High energy X-ray production in laser-solid interactions

Stuart James Morris

Doctor of Philosophy

University of York

Physics

September 2021

Abstract

The radiation produced in laser-solid interactions has been characterised at intensities relevant to petawatt-class short-pulse lasers (10^{20} to 10^{22} Wcm^{-2}). Particular attention is paid to photons of energy over 1 MeV which emerge from synchrotron radiation in the laser focal spot, and from bremsstrahlung radiation as hot electrons traverse the solid. Bremsstrahlung modelling was performed in 3D simulations using a novel hybrid-PIC code, where it was found that the emission lasted significantly longer than the laser pulse. For a driving pulse of 1 µm wavelength and 40 fs duration, the bremsstrahlung emission was found to last on the order of 10-100 ps. The efficiency of laser energy to bremsstrahlung radiation was found to be significantly higher than that reported by earlier simulations using full-PIC codes, with a peak efficiency of $(7.4 \pm 1.0)\%$ for a 10^{22} Wcm^{-2} shot on a cubic gold target of side length 100 µm. A simple analytic model is provided to estimate these bremsstrahlung efficiencies.

The hybrid-PIC code has been benchmarked against experiments on the Vulcan petawatt laser, and an empirical model has been used to emulate the complex electron refluxing behaviour on the boundaries of the simulation window. The free parameters of this model were set using both 1D and 2D full-PIC simulations. The role of self-generated magnetic fields on the X-ray efficiency was also investigated.

Despite the high bremsstrahlung efficiencies, 2D full-PIC and 3D hybrid-PIC codes were run together to demonstrate that synchrotron radiation could still dominate bremsstrahlung in some set-ups with petawatt-class lasers. In a simulation where a laser of intensity 10^{22} Wcm^{-2} and wavelength 1 µm shot a plastic target, the efficiency of laser energy to synchrotron radiation was found to be 0.84%, while the bremsstrahlung efficiency measured only 0.083%.

Contents

List of Tables

List of Figures

Acknowledgments

First and foremost, I would like to thank my supervisor Dr Christopher Ridgers - without whom this Ph.D. thesis would not have been written. It is easy for Ph.D. students to lose sight of the big picture, to not understand which results are important or worthy of publication, and I have been lucky to have a supervisor who has always provided technical support, good advice, and reassurance. I would also like to extend this gratitude to the entire York Plasma Institute and the department of physics for fostering a welcoming and supporting community, which has helped me thrive throughout my time here. Also, thanks to all the staff and students I have encountered at AWE, the University of Strathclyde, and the University of Warwick for all the external help and guidance I have received during this project.

Special thanks to my family for their unconditional support during my time in education, and my friends, old and new, who remind me there is a world beyond my physics Ph.D. The support of everyone has been especially welcome over the past few years, as this project has coincided with the Covid-19 pandemic of the early 2020's (it is my hope that future readers will find "*early* 2020's" an appropriate description). Finally I would like to extend my appreciation to Yorkshire - I can't imagine a better place to spend my Ph.D. years.

Declaration

I declare that this thesis is a presentation of original work and that I am the sole author. This thesis has not previously been accepted for any degree and is not being concurrently submitted in candidature for any degree other than Doctor of Philosophy of the University of York. This thesis is the result of my own investigations, except where otherwise stated. All other sources are acknowledged by explicit references.

Chapter 1

Introduction

1.1 X-rays

On the 8th of November, 1895, Wilhelm Röntgen made an unexpected observation. While studying the nature of electron beams passing from anode to cathode in a glass vacuum tube, he saw the glow of a fluorescent substance on a distant table. After seven weeks of investigating the mysterious "X-rays" responsible, he created the world's first X-ray image [1]. This depicted the skeletal left hand of his wife, Anna Röntgen (complete with Wedding ring), and led to Wilhelm receiving the first Nobel prize for physics.

Since their discovery, the useful properties of X-rays have led to numerous applications, with the more common uses summarised in Figure 1.1. In 1913, Bragg [2] published work detailing X-ray diffraction techniques for studying the structure of crystals, as X-ray wavelengths can be comparable to the atomic spacing in these materials. This has since evolved into the field of crystallography [3–5], with slightly higher energy X-rays used in material science for stress mapping and texture studies [6]. In 1952, London's Hammersmith hospital was fitted with a linear accelerator to create X-ray photons up to 8 MeV in energy, which utilised the ionising nature of X-rays and provided patients access to radiotherapy [7]. Eventually X-rays could be produced with energies comparable to energy levels present in nuclear physics, opening the field of photo-nuclear reactions. This provides X-rays which could actively scan for special nuclear materials (SNM) [8], or perform photo-fission reactions [9, 10] and transmute nuclear waste into medical isotopes [11]. The highest energy X-rays can be used for laboratory astrophysics experiments as they decay into electron-positron pair plasmas [12], or in quantum chromodynamics experiments for decay into pions [13]. These

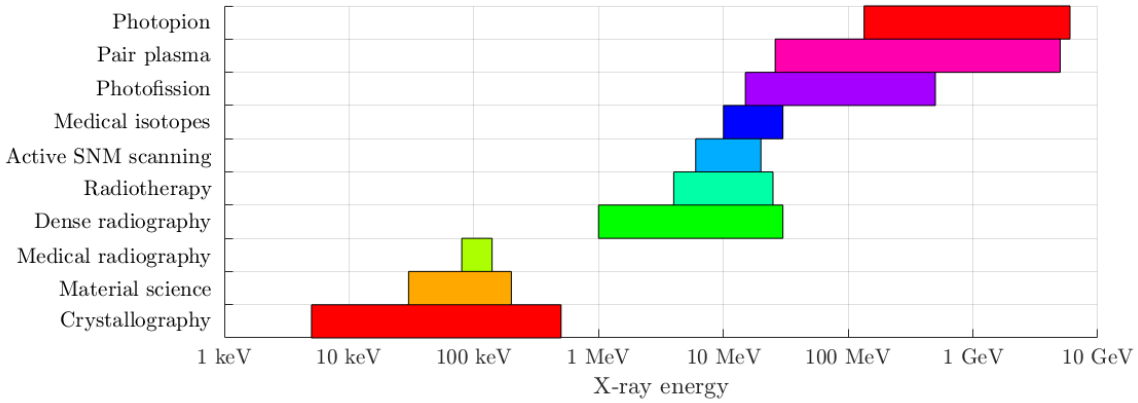

Figure 1.1: A graph detailing some of the more common applications of X-rays, plotted to show the typical X-ray energy ranges required for each one. The limits used for this plot are taken from [3–16].

higher-energy applications include photons typically associated with the label "γ-ray", but for simplicity throughout this thesis, the label of "X-ray" will be adopted for all high energy photons created through electron acceleration.

In addition to providing a source for a variety of applications, sometimes the X-rays themselves can yield interesting information. As X-rays are produced by high energy accelerating particles, they can act as a diagnostic tool to describe particle motion. This has seen use in inertial confinement fusion investigations of fast ignition schemes, to diagnose the motion of hot electrons through dense targets and to estimate the energy transferred from the laser to electrons [17]. X-rays are therefore an invaluable tool across multiple disciplines of science, and so there is some interest in the production and understanding of X-ray sources.

1.2 X-ray generation mechanisms

Most X-ray sources require two components: an energetic beam of particles and some mechanism to bend the particle trajectories. To accomplish this, various different schemes have been developed which are effective at generating a variety of different X-ray characteristics. Three of the most common types to see widespread use are synchrotron-like schemes, bremsstrahlung sources and laser-driven set-ups. Synchrotron and bremsstrahlung sources take beams of high energy electrons from accelerators, and alter electron trajectories through applying external electromagnetic fields (synchrotron) or by passing the beam through a target and using the electric fields of target nuclei (bremsstrahlung). Alternatively, the ac-

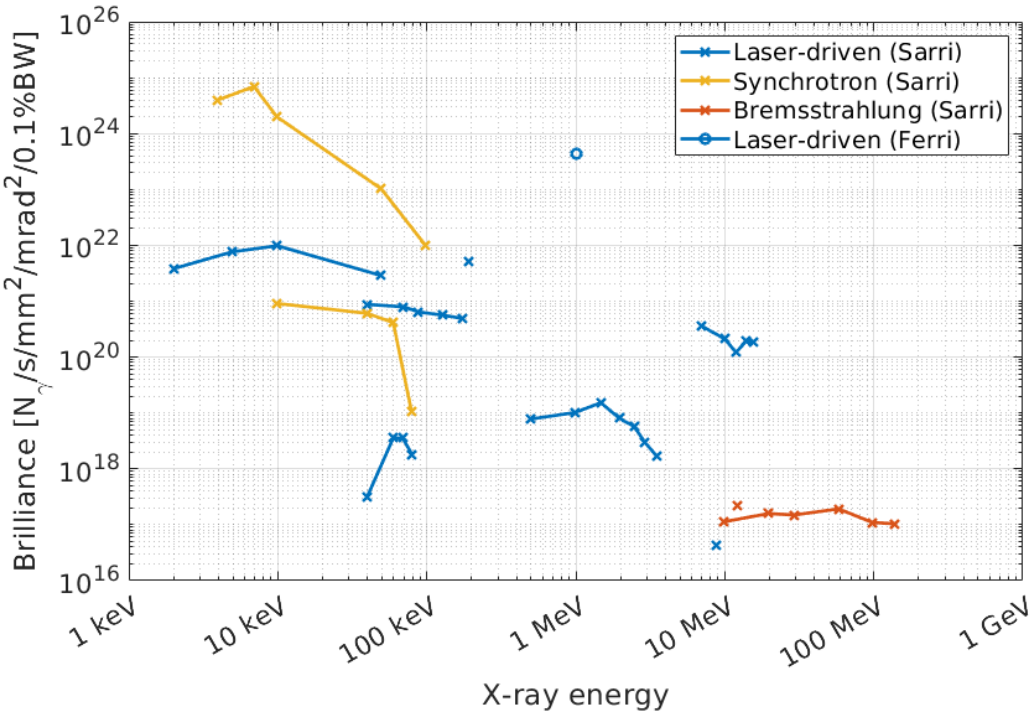

Figure 1.2: The peak brilliance achieved from a variety of X-ray sources, adapted from Figure 4 of Sarri *et al* [18], with an additional data-point from Ferri *et al* [19].

celeration and bending stages can both be achieved using lasers, which are discussed further in Section 1.3.

Many applications of X-rays involve scanning, and so a common figure of merit used for their characterisation is the brilliance, which considers four beam properties. Firstly, the rate at which photons are delivered is important, as faster scans can allow for more scans to be performed over a given period. Also, smaller beam cross-sectional areas are useful as they lead to a greater spatial resolution when scanning, and low beam divergence would provide less noisy data. Finally, we are often only interested in the behaviour of a particular X-ray energy, and so brilliance is measured as the number of photons N_γ per second passing through an area (mm^{-2}) into some solid angle (mrad^{-2}), for photons with energies of $\pm 0.1\%$ about some central photon energy.

Figure 1.2 shows the brilliance values achieved by various sources at different photon energies, coloured by the underlying mechanisms exploited by each source. Here we see that synchrotron-type sources provide the greatest brilliance for low energy X-rays, while only bremsstrahlung sources are capable of producing brilliant beams at the highest photon energies. In between these limits, in regions which are useful for dense radiography and some

photonuclear reactions, laser sources are shown to dominate the brilliance plot. It is these sources which are the focus of this thesis.

1.3 Laser-plasma interactions

Laser-plasma interactions offer some useful alternatives to conventional X-ray sources. When the plasma is low density, the laser pulse can set-up wakefields which provide accelerating fields on the order of 100 GV/m [19] compared to the 100 MV/m in linear accelerators (linacs) [20]. Thus electrons may be accelerated over a short length scale and can be made to radiate at the same time, which can provide a high brilliance source of multi-MeV X-rays.

One area where lasers will be particularly advantageous is high density radiography [21]. While synchrotrons can also be useful in this area, their large footprint can be a limiting factor for widespread use. Unlike sources accelerated by linacs, the compact accelerating area of laser-solid interactions provides a beam which is simultaneously bright and thin, providing high resolution scans of high Z targets. Hence, laser-plasma based X-ray sources have seen use in industrial radiography [22], and also in bone scans to diagnose diseases like osteoporosis [21].

With the development of next generation lasers which will come online soon, this is an interesting time to examine these systems. Facilities like ELI [23] and APOLLON [24] aim to exceed intensities of 10^{23} Wcm^{-2} within the next few years, which could produce X-rays of even higher energy. This may provide a brilliant X-ray source for triggering photo-nuclear reactions, or could even produce dense electron-positron pair plasmas for the study of laboratory astrophysics. X-rays could also play a role in diagnosing the motion of plasma particles in these next generation systems, which could provide a useful tool in future experimental campaigns.

1.4 X-rays in laser-solid interactions

When intense lasers strike solid targets, the surface is ionised and electrons in the subsequent plasma are heated to high energy. These hot electrons radiate synchrotron X-rays in the laser fields, and bremsstrahlung X-rays as they collide with nuclei in the solid density target. A more detailed breakdown of the physics involved in laser-solid interactions is provided in Chapter 3. Additional sources of X-rays are present in these systems, including high

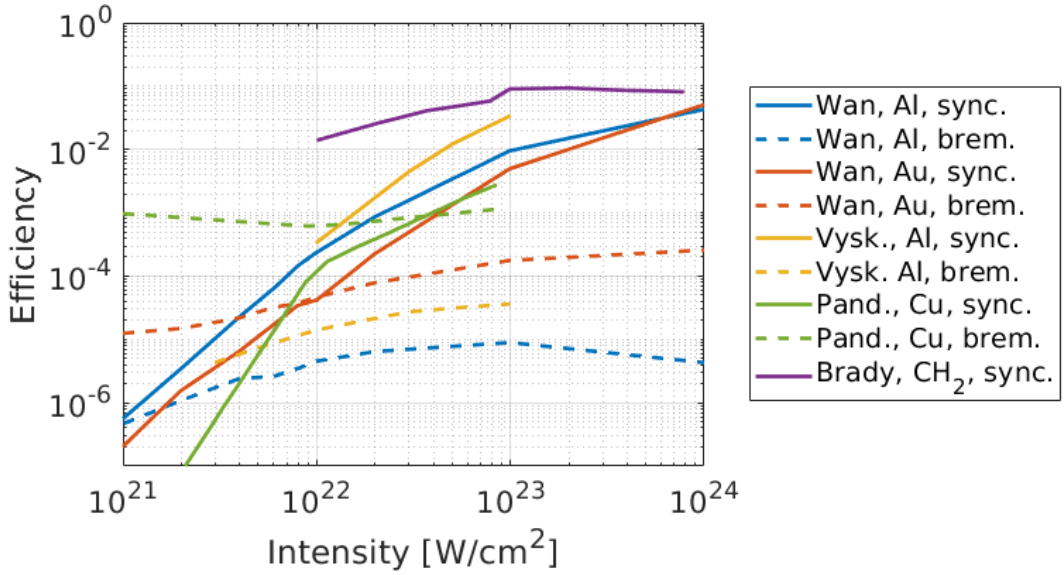

Figure 1.3: Laser to X-ray efficiencies for various laser intensities and target compositions. Solid lines denote synchrotron radiation, dashed lines are used for bremsstrahlung. Data is labelled and sourced from *Wan* [28], *Vysk.* (synchrotron [29], bremsstrahlung [30]), *Pand.* [31] and *Brady* [32].

harmonic generation (HHG), Kα emission, and coherent transition radiation (CTR).

In HHG, electrons are ionised by the laser and gain significant kinetic energy in the laser fields before being re-absorbed and emitting a high energy photon [25]. Kα emission also results from ionisation, although this refers to the photon emission due to electron de-excitation from the L shell ($n = 2$) to the K shell ($n = 1$), where n is the principle quantum number [26]. The Kα transition occurs when the K-shell is rapidly ionised before the outer-shells, either through electron or X-ray bombardment. Electrons can also emit radiation through CTR due to field changes when traversing media with different dielectric properties, such as the plasma-vacuum interface passed by escaping electrons [27]. However, as we are primarily interested in photon energies exceeding 1 MeV, then the lower keV photon energies of HHG, Kα and CTR fall outside the scope of this thesis. These processes neither contribute to the production high energy photons, nor do they make an appreciable impact on the hot electrons generating synchrotron or bremsstrahlung X-rays.

Radiation from laser-solid interactions is often described in terms of its efficiency, the ratio of the total radiated photon energy (between certain photon energy limits, typically over 1 MeV) to the total incident laser energy. A review of the bremsstrahlung efficiencies found by various groups [28–32] is given in Figure 1.3. Here it can be seen that bremsstrahlung

radiation tends to compete with and dominate synchrotron emission at intensities below 10^{22} Wcm^{-2}, making bremsstrahlung the most important X-ray source for modern petawatt-class lasers. However, the efficiencies present in Figure 1.3 were deduced through numerical simulation, and the codes used to perform this analysis were too computationally expensive to model the entire interaction. As a result, it is expected that these efficiencies underestimate the total bremsstrahlung emission. The work performed in this thesis aims to address these limitations, and to develop greater tools for modelling high energy X-ray production. Such work could be useful for both maximising the bremsstrahlung emission to explore the viability of a compact X-ray source, and for minimising bremsstrahlung as a background to synchrotron radiation.

Next generation lasers are expected to reach intensities which may exceed 10^{22} Wcm^{-2}. As seen in Figure 1.3, the synchrotron radiation scales faster with laser intensity, and should become the dominant emission mechanism in multi-petawatt lasers. This could be useful as not only a bright X-ray source, but also as a diagnostic for hot electron motion in the laser focal spot. However, the laser intensity at which synchrotron radiation dominantes bremsstrahlung is ambiguous, and dependent on the target composition. Experimental verification of synchrotron radiation may be challenging due to this bremsstrahlung background, particularly at the intensities available with petawatt-class lasers. In Chapter 8, we present work in search of synchrotron signatures at these lower intensities, along with a more rigorous characterisation of the bremsstrahlung background. This is useful for experimentally benchmarking synchrotron models, and also as a means to provide insight to experiments with next-generation lasers.

Some characteristics of the synchrotron and bremsstrahlung emissions have already been studied. For example, the angular distributions of both radiation sources have been given in Figure 1.4, and were calculated from simulation [29, 30]. In both cases, the angular distribution of the X-rays is related to that of the electrons, as ultra-relativistic electrons radiate in the direction of motion. Inside the target, hot electrons were found to reflect off target boundaries, losing longitudinal momentum as they did so. As a result, the bremsstrahlung emission starts along the initial electron direction (laser axis), but splits off to lobes as electrons scatter off the boundaries. The nature of this scatter was not well understood, but has been investigated in Section 5.7 of this thesis. Such work is important to understand the role target geometry plays in radiation production. Similarly, synchrotron radiation mechanisms

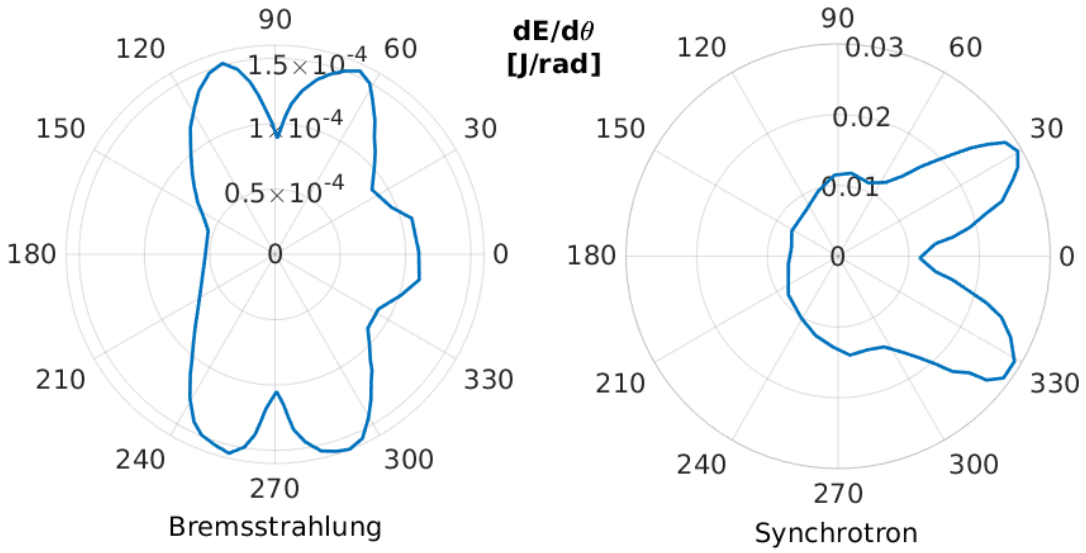

Figure 1.4: Angular distributions of X-rays created in laser-solid interactions. Results are from 2D simulations (synchrotron [29], bremsstrahlung [30]), scaled to 3D by assuming a length-scale in the omitted direction equal to the laser FWHM focal spot size. Both use a 30 fs laser with peak intensity 10^{22} Wcm^{-2} on a 2 µm target, with different compositions. The bremsstrahlung target was Al and an X-ray band of 2-10 MeV was considered, while the synchrotron target was plastic with a pre-plasma, and X-rays between 2.3 and 4.8 MeV were plotted. The laser pulse initially travelled in the $\theta = 0$ direction.

are also explored - particularly theory related to the backwards emission depicted in Figure 1.4. A detailed understanding of both radiation mechanisms is needed to fully exploit X-ray production in both current and next-generation laser facilities.

1.5 Thesis outline

In this thesis, we intend to study the X-rays generated in high intensity laser-solid simulations. In Chapter 2, we discuss the theory of X-ray emission due to electron acceleration in both classical and quantum frameworks, and elaborate on the X-ray generation mechanisms outlined in Figure 1.2. Then in Chapter 3, we turn our attention to laser-solid interactions, which is the X-ray generation system of interest for our research.

Throughout this thesis, we will attempt to describe these complex systems through numerical simulation. Chapter 4 provides detail on the Particle-In-Cell (PIC) codes which are typically employed to model these X-ray emissions, and we also introduce the bremsstrahlung module which we developed for this project. The chapter ends with a discussion of PIC-code limitations, namely the computational expense and the small length and time scales which

must be modelled. To address these limitations, we have written a hybrid-PIC code which is detailed in Chapter 5, and a set of test problems is presented in Chapter 6 for benchmarking.

Finally, we present the results from our hybrid-PIC simulations in Chapter 7, where we focus on bremsstrahlung X-rays produced within the solid target. In Chapter 8, we provide the results from a similar simulation campaign which studied the synchrotron X-rays produced in the laser-focal spot, and the two individual X-ray generation mechanisms are compared. We finish with our conclusions in Chapter 9.

Chapter 2

Radiation

This thesis details my work on characterising X-ray emissions in laser-solid interactions. Before diving into the detailed theory of how solids behave under irradiation from intense laser pulses, it is useful to put this work into context. In this introduction, a general overview of radiation theory will be given, using both classical and quantum descriptions of the processes. The chapter closes with a summary of existing and proposed X-ray generation methods, and provides some extra motivation for the generation of high energy photons.

2.1 Radiation

Over the course of this thesis, we are primarily interested in the high energy photons produced as electrons accelerate. In classical electrodynamics, the assertion that accelerating charged particles produce radiation is a natural consequence of Maxwell's equations,

$$\nabla \cdot \mathbf{E} = \frac{\rho}{\epsilon_0} \tag{2.1}$$

$$\nabla \cdot \mathbf{B} = 0 \tag{2.2}$$

$$\nabla \times \mathbf{E} = -\frac{\partial \mathbf{B}}{\partial t} \tag{2.3}$$

$$\nabla \times \mathbf{B} = \mu_0 \mathbf{J} + \frac{1}{c^2}\frac{\partial \mathbf{E}}{\partial t} \tag{2.4}$$

where (2.1) denotes Gauss' law, (2.2) forbids magnetic monopoles, and (2.3) and (2.4) show the Faraday-Lenz and Ampère-Maxwell laws respectively [33, 34]. Vector and scalar poten-

tials, $\mathbf{A}$ and ϕ may be defined such that

$$\mathbf{B} = \nabla \times \mathbf{A} \tag{2.5}$$

$$\mathbf{E} = -\nabla\phi - \frac{\partial \mathbf{A}}{\partial t} \tag{2.6}$$

as these still satisfy the constraints of (2.2) and (2.3), with some freedom over the specific choice of $\mathbf{A}$ and ϕ. Using the Lorenz gauge defined as $\nabla \cdot \mathbf{A}c^2 = -\partial\phi/\partial t$, the potential fields may be substituted into (2.1) and (2.4) to return the inhomogeneous wave equations

$$\left(\nabla^2 - \frac{1}{c^2}\frac{\partial^2}{\partial t^2}\right)\phi = -\frac{\rho}{\epsilon_0} \tag{2.7}$$

$$\left(\nabla^2 - \frac{1}{c^2}\frac{\partial^2}{\partial t^2}\right)\mathbf{A} = -\mu_0\mathbf{J} \tag{2.8}$$

which have solutions

$$\phi(\mathbf{r}, t) = \frac{1}{4\pi\epsilon_0}\int_V \frac{\rho\left(\mathbf{r'}, t - \frac{|\mathbf{r}-\mathbf{r'}|}{c}\right)}{|\mathbf{r}-\mathbf{r'}|}d^3\mathbf{r'} \tag{2.9}$$

$$\mathbf{A}(\mathbf{r}, t) = \frac{\mu_0}{4\pi}\int_V \frac{\mathbf{J}\left(\mathbf{r'}, t - \frac{|\mathbf{r}-\mathbf{r'}|}{c}\right)}{|\mathbf{r}-\mathbf{r'}|}d^3\mathbf{r'} \tag{2.10}$$

where the volume integral is evaluated over all space. Considering a point particle with charge, e, and substituting the potentials from (2.9) and (2.10) into the field equations (2.5) and (2.6) yields the Liénard-Wiechert fields

$$\mathbf{E}(\boldsymbol{r}, t) = \frac{e}{4\pi\epsilon_0}\left[\frac{(\hat{\boldsymbol{n}} - \boldsymbol{\beta})(1-\beta^2)}{\kappa^3 R^2}\right]_{\text{ret}} + \frac{e}{4\pi\epsilon_0 c}\left[\frac{\hat{\boldsymbol{n}} \times ((\hat{\boldsymbol{n}} - \boldsymbol{\beta}) \times \dot{\boldsymbol{\beta}})}{\kappa^3 R}\right]_{\text{ret}} \tag{2.11}$$

$$\mathbf{B}(\mathbf{r}, t) = [\hat{\boldsymbol{n}}]_{\text{ret}} \times \frac{\mathbf{E}(\mathbf{r}, t)}{c} \tag{2.12}$$

where terms in the square brackets are evaluated for the charged particle at the retarded time $t_r = t - R(t_r)/c$. Here, R is the distance from the charge to the observation point $\mathbf{r}$, and $\hat{\boldsymbol{n}}$ is a unit vector pointing from the charge to $\mathbf{r}$. The scalar κ represents $1 - \hat{\boldsymbol{n}} \cdot \boldsymbol{\beta}$, where $\boldsymbol{\beta}$ and $\dot{\boldsymbol{\beta}}$ are the velocity and acceleration vectors for the particle respectively, both divided by c.

As seen in (2.11), the electric fields for a charged particle may be split into two terms. The first has no dependence on the acceleration $\dot{\boldsymbol{\beta}}$ and a strength which falls off quickly

as $1/R^2$. The second term we shall call $\mathbf{E}_a$, and represents fields arising from accelerating charged particles, only falling off as $1/R$. We can demonstrate the radiative properties of E_a by first considering its non-relativistic behaviour ($\beta \to 0$). The energy flux in a given direction carried by electric and magnetic fields is given by the Poynting vector, $\mathbf{S}$

$$\mathbf{S} = \frac{1}{\mu_0}\mathbf{E} \times \mathbf{B} \tag{2.13}$$

which for $\mathbf{E}_a$ takes the form $|\mathbf{E}_a|^2\hat{\boldsymbol{n}}/\mu_0 c$. Thus, the power flowing through an infinitesimal area, dA at the observation point, $\mathbf{r}$ is SdA, where $dA = R^2 d\Omega$. The angular distribution of power is then

$$\frac{dP}{d\Omega} = \frac{1}{\mu_0 c}|R\mathbf{E}_a|^2 = \frac{e^2}{16\pi^2\epsilon_0 c}\dot{\beta}^2 \sin^2\theta \tag{2.14}$$

where θ is the angle between $\hat{\boldsymbol{n}}$ and $\dot{\boldsymbol{\beta}}$. In (2.14), we see that power doesn't diminish with increasing distance from the charge to the observer, R, and so this solution represents the transport of electromagnetic power over space (radiation). Integrating over all solid angles $d\Omega$ yields Larmor's formula for the total radiated power, P

$$P = \frac{2}{3}\frac{e^2}{4\pi\epsilon_0 c^3 m^2}\left(\frac{d\mathbf{p}}{dt} \cdot \frac{d\mathbf{p}}{dt}\right). \tag{2.15}$$

The relativistic generalisation of Larmor's formula may be obtained by constructing a form from Lorentz invariant quantities which retains the non-relativistic behaviour of (2.15). Jackson [33] describes how this may only be satisfied by

$$P = \frac{2}{3}\frac{e^2}{4\pi\epsilon_0 c^3 m^2}\left(\frac{dp_\mu}{d\tau}\frac{dp^\mu}{d\tau}\right) \tag{2.16}$$

where p_μ denotes the 4-momentum of the charge, and $d\tau$ an interval of proper time. Solving this yields the classical result for the power radiated by an accelerating, relativistic particle,

$$P = \frac{2}{3}\frac{e^2}{4\pi\epsilon_0 c}\gamma^6(\dot{\beta}^2 - (\boldsymbol{\beta} \times \dot{\boldsymbol{\beta}})^2). \tag{2.17}$$

While (2.17) describes the radiation power produced by accelerating charges, it doesn't address the cause of acceleration. Relativistic electrons passing through matter are accelerated by the electric fields of atomic nuclei, and the resultant emissions are termed *bremsstrahlung*

radiation. Acceleration also occurs for electrons passing through external electromagnetic fields, which results in *synchrotron* radiation (this term refers to a particular field configuration, but will be used to describe the general case in this thesis - see Section 2.4). While the emission of photons is an inherently quantum process, considering the radiation from these sources using classical arguments provides simple analytic scaling laws for total emitted power, which will be discussed further in later subsections. It is also possible to describe the radiation spectrum using classical arguments, which will be useful in describing classical bremsstrahlung.

2.1.1 Classical radiation spectra

Jackson obtains a radiation spectrum by considering the flash of radiation seen by an observer as an accelerating charge passes by. The rise and fall of radiation power may be broken down into a Fourier spectrum of waves with different frequencies, which corresponds to an energy spectrum for radiation. If the angular distribution of power is rewritten as

$$\frac{dP(t)}{d\Omega} = |\mathbf{F}(t)|^2 \tag{2.18}$$

then the angular distribution of total energy is

$$\frac{dW}{d\Omega} = \int_{-\infty}^{\infty} |\mathbf{F}(t)|^2 dt = \int_{-\infty}^{\infty} |\mathbf{F}(\omega)|^2 d\omega \tag{2.19}$$

where we define the Fourier transform of $\mathbf{F}(t)$ as

$$\mathbf{F}(\omega) = \frac{1}{\sqrt{2\pi}} \int_{-\infty}^{\infty} e^{i\omega t} \mathbf{F}(t) dt. \tag{2.20}$$

By substituting the relativistic form of $\mathbf{E}_a$ into the Poynting vector (2.13), a relativistic form of $dP(t)/d\Omega$ can be obtained, which results in

$$\mathbf{F}(\omega) = \frac{e}{\sqrt{32\pi^3 \epsilon_0 c}} \int_{-\infty}^{\infty} \frac{\hat{\boldsymbol{n}} \times ((\hat{\boldsymbol{n}} - \boldsymbol{\beta}) \times \dot{\boldsymbol{\beta}})}{(1 - \boldsymbol{\beta} \cdot \hat{\boldsymbol{n}})^2} e^{i\omega(t - \hat{\boldsymbol{n}} \cdot \mathbf{r}(\mathbf{t})/c)} dt. \tag{2.21}$$

As there is no special significance to negative ω, we instead define a double differential on radiated energy $d^2W/d\Omega d\omega$ such that

$$\frac{dW}{d\Omega} = \int_0^\infty \frac{d^2W}{d\Omega d\omega} d\omega \tag{2.22}$$

and so $d^2W/d\Omega d\omega = 2|\mathbf{F}(\omega)|^2$. This double differential energy distribution may be simplified further by considering the non-relativistic case $\beta \to 0$. Assuming a characteristic interaction time of $\tau \approx x/v$ (where v and x are characteristic particle speeds and length scales during the interaction), then we may integrate the non-relativistic form of $d^2W/d\Omega d\omega$ to obtain an energy spectrum, $dW/d\omega$ in high and low frequency limits

$$\frac{dW}{d\omega} \approx \begin{cases} \frac{e^2}{6\pi^2\epsilon_0 c}|\Delta\boldsymbol{\beta}|^2 & \omega\tau < 1 \\ 0 & \omega\tau > 1 \end{cases} \tag{2.23}$$

which implies a cut-off frequency of $\omega = v/x$. Here, $|\Delta\boldsymbol{\beta}|$ describes the change in $\boldsymbol{\beta}$ over the characteristic interaction time.

Similarly, we may obtain a fully-relativistic angular distribution of radiation power in the low frequency limit,

$$\frac{dP(t')}{d\Omega} = \frac{e^2}{16\pi^2\epsilon_0 c} \frac{\left|\hat{\boldsymbol{n}} \times ((\hat{\boldsymbol{n}} - \boldsymbol{\beta}) \times \dot{\boldsymbol{\beta}})\right|^2}{(1 - \boldsymbol{\beta}\cdot\hat{\boldsymbol{n}})^5} \tag{2.24}$$

where terms have been evaluated at the photon emission time t'. This angular distribution becomes strongly peaked in the $\boldsymbol{\beta}$ direction for particles approaching the ultra-relativistic limit, with the root-mean-square angle between radiation direction and $\boldsymbol{\beta}$ falling as $\theta_{rms} = 1/\gamma$.

2.2 Bremsstrahlung radiation

Bremsstrahlung describes the radiation caused by charged particles accelerating in the electric fields of nuclei. In Section 2.1 we demonstrate that accelerating charged particles produce radiation, and discuss the energy spectrum for non-relativistic particles using classical arguments. Jackson also provides a method for using these equations to obtain a classical description of bremsstrahlung radiation [33].

We start by considering the case of a fast but non-relativistic electron approaching a bare nucleus. In the frame moving at the initial velocity of the electron, $\mathbf{v}$, we see a nucleus approaching a non-relativistic electron with velocity $-\mathbf{v}$. In this frame, the electric field on the moving nucleus is simply given by Coulomb's law,

$$\mathbf{E}' = \frac{-e}{4\pi\epsilon_0(b^2 + (vt')^2)}\hat{\boldsymbol{n}}' \tag{2.25}$$

where the impact parameter, b describes the distance between the electron and nucleus in the direction perpendicular to $\mathbf{v}$, and $\hat{\boldsymbol{n}}'$ is a unit vector pointing from electron to nucleus. We have arbitrarily set $t' = 0$ in this frame to correspond to the time of shortest electron-nucleus distance, and the trajectories of both particles are assumed to be unaffected during the interaction time. This field can be Lorentz transformed into the lab-frame [33], and the momentum transfer can be calculated by integrating the resultant force on the nucleus over all times. Hence, the parameter $|\Delta\boldsymbol{\beta}|$ takes the form

$$|\Delta\boldsymbol{\beta}| = \frac{Ze^2}{2\pi\epsilon_0 m_e v b c} \tag{2.26}$$

giving a bremsstrahlung spectrum of

$$\frac{dW}{d\omega} \approx \begin{cases} \frac{Z^2e^2}{24\pi^4\epsilon_0^3 c}\left(\frac{e^2}{m_e c^2}\right)^2\left(\frac{c}{v}\right)^2\frac{1}{b^2} & \omega < \frac{v}{b} \\ 0 & \omega > \frac{v}{b} \end{cases} \tag{2.27}$$

where we have replaced the characteristic interaction distance with the impact parameter. This form is not very useful in large systems, as it requires knowledge of b for every electron-nucleus collision. Instead, we define a *radiation cross section*,

$$\frac{d\chi}{d\omega} = 2\pi\int_{b_{min}}^{b_{max}} \frac{dW}{d\omega} b db \tag{2.28}$$

where b_{min} and b_{max} describe the range of impact parameters which produce non-negligible radiation. Physically, the integration of $d\chi/d\omega$ between ω' and $(\omega' + d\omega)$ yields the cross section, multiplied by the radiated energy per electron-nucleus collision, for radiation with ω between these limits.

We consider relativistic bremsstrahlung by returning to the frame co-moving with the electron, where the electron remains non-relativistic throughout this interaction. Here,

$dW'/d\omega'$ is described by (2.27), and $d\chi/d\omega$ may be approximated for a suitable choice of the b limits. From (2.27), it is clear there is no radiation above $b_{max} \approx \gamma v/\omega'$, where a γ factor is introduced due to the Lorentz transformation. The uncertainty principle gives us $b_{min} \approx \hbar/m_e v$. Solving (2.28) with these limits and transforming back to the lab-frame yields the radiation cross section

$$\frac{d\chi}{d\omega} \approx \frac{Z^2 e^2}{12\pi^3 \epsilon_0^3 c}\left(\frac{e^2}{m_e c^2}\right)^2 \ln\left(\frac{\kappa\gamma^2 m_e v^2}{\hbar\omega}\right) \tag{2.29}$$

where κ denotes the uncertainty in b limit approximations, and is of order unity.

2.2.1 Atomic screening

Equation (2.29) describes the radiation produced by an incident electron accelerating in the Coulomb field of a bare nucleus, but the electric field on this electron will actually be a combination of fields from the nucleus and orbital electrons if our target is composed of neutral atoms. The orbital electrons reduce the Coulomb field strength experienced by the incident electron, resulting in a screened potential of the approximate form

$$V(r) = \frac{Ze}{4\pi\epsilon_0 r} e^{-r/a} \tag{2.30}$$

according to Thomas-Fermi theory [35], where the characteristic atomic length scale $a = 1.4 a_B Z^{-1/3}$, and a_B is the Bohr radius. The difference between potentials from bare/screened nuclei is shown in Figure 2.1 for the case of aluminium (Al). Jackson obtains a screened differential bremsstrahlung cross section by assuming the Coulomb field around the nucleus becomes negligible at $r = a$, which sets a maximum impact parameter of $b_{max} = \min(a, \gamma^2 v/\omega)$ [33]. Hence, this screening correction is only applied to the differential cross section for frequencies below

$$\omega_s = \frac{Z^{1/3}\gamma^2 m_e v c}{1.4\hbar}\left(\frac{e^2}{4\pi\epsilon_0 \hbar c}\right) \tag{2.31}$$

where we have

$$\frac{d\chi}{d\omega} = \frac{Z^2 e^2}{12\pi^3 \epsilon_0^3 c}\left(\frac{e^2}{m_e c^2}\right)^2 \ln\left(\lambda \frac{1.4\hbar v(4\pi\epsilon_0)}{Z^{1/3} e^2}\right). \tag{2.32}$$

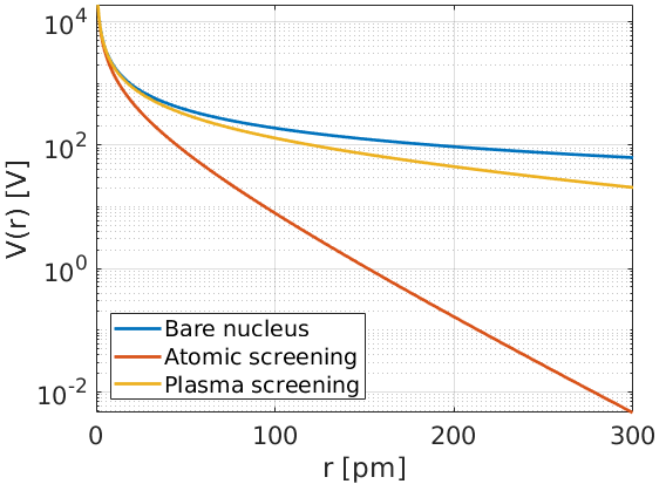

Figure 2.1: The electrical potential, $V(r)$ of an Al nucleus as a function of distance, r for three different screening models. In the plasma case, an Al plasma is used with an electron temperature of 1 keV, and ion density $n_i = 6.026 \times 10^{28}$ m^{-3} (solid density).

Equation (2.31) shows that the critical frequency, ω_s rises with the electron γ-factor. Once $\hbar\omega_s$ exceeds the electron kinetic energy, the screening becomes "complete", and radiation is emitted according to (2.32) at every frequency.

2.2.2 Plasma screening

Expressions for bremsstrahlung radiation in ionised targets can be obtained using charge-screening arguments similar to those used in deriving the differential bremsstrahlung cross section with orbital electron screening (2.32). A heavily ionised target may be modelled as a plasma - a collection of negatively charged free electrons and positively charged ions. These free electrons will be distributed through space differently to their bound counterparts, and Thomas-Fermi screening (2.30) will no longer be a valid potential model. Instead, the screening of nuclear charge potential can be modelled by Debye shielding (see Section 3.1.1),

$$V(r) = \frac{Ze}{4\pi\epsilon_0 r} e^{-r/\lambda_D} \tag{2.33}$$

where the Debye length λ_D is given by

$$\lambda_D = \sqrt{\frac{\epsilon_0 k_B T_e}{n_e e^2}} \tag{2.34}$$

for a given electron temperature and number density T_e and n_e respectively [36]. This Debye shielding model is derived by solving Gauss' law (2.1) for a Boltzmann distribution of charges [36]. The potential (2.33) is also plotted in Figure 2.1 for an Al target heated to 1 keV, where the mean ionisation state was found to be $Z^* \approx 12.7$ using the `FLYCHK` tables [37].

Equation (2.33) is of the same form as the atomic screened potential (2.30), with the length parameter a replaced with λ_D. The radiation cross section for ionised targets may therefore be approximated as

$$\frac{d\chi}{d\omega} = \frac{Z^2 e^2}{12\pi^3 \epsilon_0^3 c}\left(\frac{e^2}{m_e c^2}\right)^2 \ln\left(\lambda \frac{m_e v}{\hbar}\sqrt{\frac{\epsilon_0 k_B T_e}{n_e e^2}}\right) \tag{2.35}$$

in the complete screening limit.

2.2.3 Quantum cross-section

The previous subsections deal with a classical description of bremsstrahlung radiation, and while this provides a good approximation for radiation power, it fails to fully describe the quantum process of photon emission. Multiple groups have derived quantum expressions for bremsstrahlung radiation in various approximations and limits, which are combined into the differential cross section tables, $d\sigma/d\epsilon_\gamma$ given by Seltzer and Berger, where ϵ_γ denotes the emitted photon energy [38, 39]. These include the differential cross sections for electrons with kinetic energies, ϵ_k between 1 keV and 10 GeV, passing through targets with atomic numbers numbers from 1 to 100. These represent the total cross sections for atomic targets, including bremsstrahlung due to both the interaction with the nucleus ($e^- n$), and the Z atomic electrons ($e^- e^-$) [38]. The total cross-sections integrated over all ϵ_γ are shown in Figure 2.2.

For ϵ_k values between 1 keV and 2 MeV, the Seltzer-Berger $e^- n$ cross sections use analytic results from Pratt *et al* [40], where the emission is treated as a single-electron transition in a screened atomic potential. The cross sections were obtained by solving the Dirac equation for electrons in targets with $2 \leq Z \leq 92$.

For electrons with kinetic energy over 50 MeV, the Seltzer-Berger $e^- n$ cross sections combine multiple bremsstrahlung models, and take the general form

$$\frac{d\sigma_n}{d\epsilon_\gamma} = \frac{Z^2 e^2}{16\pi^3 \epsilon_0^3 \hbar c}\left(\frac{e^2}{m_e c^2}\right)^2 \frac{1}{\epsilon_\gamma}(\chi_{Born}^{unscr} + \delta_{screen} + \delta_{Coul}) \tag{2.36}$$

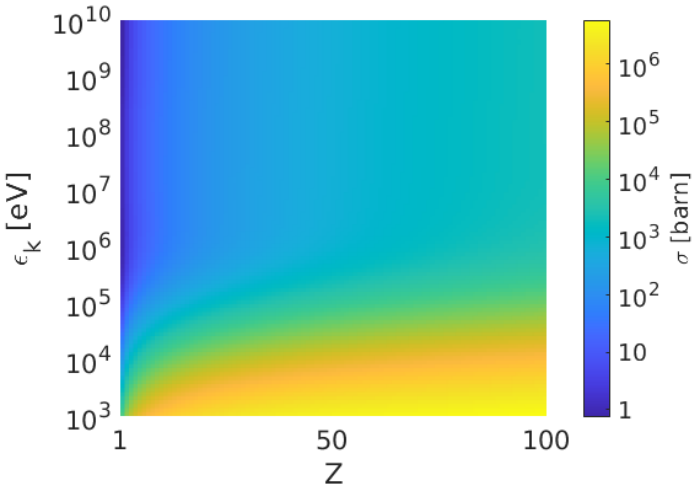

Figure 2.2: The total integrated bremsstrahlung cross section per atom, σ, using the Seltzer-Berger model [38]. This is expressed as a function of target atomic number, Z, and incident electron kinetic energy, ϵ_k. 1 barn $\equiv 10^{-28}$ m^2.

where χ_{Born}^{unscr} is chosen such that (2.36) returns the unscreened differential cross section, calculated by solving the Dirac equation with the Born approximation (if δ_{screen} and δ_{Coul} are set to zero) [41]. Here the electron wavefunction interacts with the potential of a bare nucleus, where this potential is treated as a small perturbation to the wavefunction (Born approximation). The additive correction factors δ_{screen} and δ_{Coul} introduce screening and Coulomb effects respectively. The term δ_{screen} maps the unscreened Born differential cross secton onto a corresponding screened Born result (for $\delta_{Coul} = 0$) [42]. The Born approximation has been shown to over-predict the cross section for electrons in heavy elements by up to 10% in the case of lead [43]. To correct for this, the δ_{Coul} term is chosen to map $d\sigma_n/d\epsilon_\gamma$ onto unscreened equations derived without the Born approximation (for $\delta_{screen} = 0$) [38,43]. The $d\sigma_n/d\epsilon_k$ values for ϵ_k in the range 2-50 MeV are interpolated between the two regimes, providing a smooth transition between the different theories.

The e^-e^- cross sections are calculated using a similar treatment, with the general form

$$\frac{d\sigma_e}{d\epsilon_\gamma} = \frac{Ze^2}{16\pi^3\epsilon_0^3\hbar c}\left(\frac{e^2}{m_e c^2}\right)^2 \frac{1}{\epsilon_\gamma}(f_{ee}\chi_{Haug} + \delta_{screen}^e) \tag{2.37}$$

where χ_{Haug} denotes the bremsstrahlung radiation from an unscreened target electron in the Born approximation, δ_{screen}^e is a correction factor for screening, and f_{ee} is a multiplicative Coulomb correction. Much like the e^-n case, the quantum cross-sections come from solving the Dirac equation [44].

These differential cross sections can be combined into a cross section per atom,

$$\frac{d\sigma}{d\epsilon_k} = \frac{d\sigma_n}{d\epsilon_k} + Z\frac{d\sigma_e}{d\epsilon_k} \tag{2.38}$$

which has been benchmarked against experiment to obtain uncertainty estimates [39]. For $\epsilon_k < 2$ MeV, the Seltzer-Berger cross sections agreed with experimental data within an uncertainty of around 10%. This falls to 3-5% in experiments with $\epsilon_k > 50$ MeV, and the interpolation region was found to be accurate between 5% and 10%.

2.3 Radiation reaction

Radiation reaction is a classical, higher-order correction to the Lorentz force law. It provides a resistive force corresponding to the recoil of charged particles when they emit radiation, and a derivation has been provided by Landau and Lifshitz [45]. This begins by considering the Lagrangian of a particle with charge, q and mass, m moving at speed, v in an electromagnetic field,

$$\mathcal{L} = -mc^2\sqrt{1-\frac{v^2}{c^2}} + q\mathbf{A}\cdot\mathbf{v} - q\phi \tag{2.39}$$

where the field potentials are defined in (2.5) and (2.6). Let us also rewrite the potentials (2.9) and (2.10) as

$$\phi = \frac{1}{4\pi\epsilon_0}\int_V \frac{\rho_{ret}}{R}dV \tag{2.40}$$

$$\mathbf{A} = \frac{\mu_0}{4\pi}\int_V \frac{\rho_{ret}\mathbf{v}}{R}dV \tag{2.41}$$

where the current density has been expressed as the product of the charge density and its velocity.

In the non-relativistic limit, the ratio v/c is small, and so the scalar and vector potentials (2.40) and (2.41) may be expanded to

$$\phi = \frac{1}{4\pi\epsilon_0}\left(\int\frac{\rho}{R}dV - \frac{1}{c}\frac{\partial}{\partial t}\int\rho dV + \frac{1}{2c^2}\frac{\partial^2}{\partial t^2}\int R\rho dV - \frac{1}{6c^3}\frac{\partial^3}{\partial t^3}\int R^2\rho dV\right) \tag{2.42}$$

$$\mathbf{A} = \frac{\mu_0}{4\pi}\left(\int\frac{\rho\mathbf{v}}{R}dV - \frac{1}{c}\frac{\partial}{\partial t}\int\rho\mathbf{v}dV\right). \tag{2.43}$$

These forms have been chosen to ensure all terms in $\mathcal{L}$ are evaluated to third order in $1/c$. The vector potential, $\mathbf{A}$ has two fewer terms in its expansion because the pre-factor $\mu_0/4\pi$ already carries an extra $1/c^2$ when compared to $1/4\pi\epsilon_0$ for the scalar potential. The $1/c$ term of (2.42) describes the rate of change of a conserved quantity (total charge), and so this term may be removed from the expansion.

The third order term of equation (2.42) may be removed by considering an appropriate gauge, as gauge invariance permits us to introduce any scalar function, λ provided the potentials are modified by

$$\phi \to \phi - \frac{\partial \lambda}{\partial t} \tag{2.44}$$

$$\mathbf{A} \to \mathbf{A} + \nabla\lambda \tag{2.45}$$

because these new potentials still satisfy their original definitions, (2.5) and (2.6). Hence, for

$$\lambda = -\frac{1}{24\pi\epsilon_0 c^3}\frac{\partial^2}{\partial t^2}\int R^2 \rho dV \tag{2.46}$$

we obtain

$$\phi = \frac{1}{4\pi\epsilon_0}\left(\int \frac{\rho}{R}dV + \frac{1}{2c^2}\frac{\partial^2}{\partial t^2}\int R\rho dV\right) \tag{2.47}$$

$$\mathbf{A} = \frac{\mu_0}{4\pi}\left(\int \frac{\rho\mathbf{v}}{R}dV - \frac{2}{3c}\int \rho\dot{\mathbf{v}}dV\right) \tag{2.48}$$

where we have used $\mathbf{R} = \mathbf{R}_0 - \mathbf{r}(t)$ for observation point $\mathbf{R}_0$ and charge position $\mathbf{r}(t)$. We have also used $\dot{\mathbf{R}} = -\mathbf{v}$ and $\nabla R^2 = 2\mathbf{R}$, as ∇ describes differentiation with respect to observation point coordinates.

Using the scalar potential definition (2.6), the force on an electron associated with the highest order term of our expansion is

$$F_{LA} = \frac{e^2}{6\pi\epsilon_0 c^3}\ddot{\mathbf{v}} \tag{2.49}$$

which is termed the Lorentz-Abraham force. This force is extended to the relativistic case by invoking two arguments: the equation must reduce to (2.49) in the limit $c \to \infty$, and $f^\mu u_\mu = 0$ for any 4-velocity $u^\mu = \gamma(c, \mathbf{v})$ and 4-force $f^\mu = d(E/c, \mathbf{p})/d\tau$, where τ is the

proper time. The Lorentz-Abraham-Dirac 4-force satisfies both conditions

$$F^{\mu}_{LAD} = \frac{2e^2}{12\pi\epsilon_0 c^3}\left(\frac{d^2u^{\mu}}{d\tau^2} + \frac{1}{c^2}\frac{du^{\nu}}{d\tau}\frac{du_{\nu}}{d\tau}u^{\mu}\right). \tag{2.50}$$

2.3.1 Landau-Lifshitz equation

The Lorentz-Abraham (2.49) and Lorentz-Abraham-Dirac forces (2.50) describe the radiation reaction process, but these equations can exhibit non-physical solutions. One particularly troubling solution suggests that particles at rest may undergo exponential acceleration in the absence of an electromagnetic field, in clear violation of the conservation of energy. The issues come from the classical treatment which has potentials falling off as $1/R$ for point particles, as this implies an infinite energy and mass which contradicts the finite electron mass used in Section 2.3 [45].

To address these inaccuracies, Landau and Lifshitz proposed an approximation to (2.50) without run-away solutions. When assuming the radiation reaction is significantly smaller than the Lorentz force in the electron rest frame, the acceleration terms in (2.50) may be replaced by the Lorentz force acceleration. The spatial components of this new equation yield the Landau-Lifshitz force

$$F_{LL} = -\frac{e^2 m_e^2 c^2}{6\pi\epsilon_0\hbar^2}\eta^2\hat{\boldsymbol{n}} \tag{2.51}$$

where $\hat{\boldsymbol{n}}$ is the direction of electron motion, the Lorentz invariant η^2 takes the form

$$\eta^2 = \frac{1}{E_s^2}\left(\left|\gamma\mathbf{E} + \frac{1}{m_e c}(\mathbf{p}\times c\mathbf{B})\right|^2 - \frac{1}{(m_e c)^2}(\mathbf{E}\cdot\mathbf{p})^2\right) \tag{2.52}$$

and the Schwinger field $E_s = m_e^2 c^3/e\hbar$. Physically, η describes the ratio of the electric field experienced by an electron in its rest frame to the Schwinger field. Equation (2.51) is strictly classical, and the $\hbar$ term is cancelled by a corresponding $\hbar$ in the Schwinger field. These $\hbar$ terms have been included to demonstrate a dependence on η^2, which will be used in later sections.

2.4 Synchrotron radiation

Radiation due to relativistic electron motion in an external electromagnetic field has been addressed for many special cases. The resulting models are given different names, including magneto-bremsstrahlung, curvature radiation, non-linear Thomson scatter and non-linear Compton scatter. Synchrotron radiation is also a special case, referring to the radiation of electrons travelling through a synchrotron (uniform magnetic field) - but in this thesis we will use this as an umbrella term for all of these processes, as done by Kirk *et al* [46]. A justification for this treatment is provided in Section 2.4.2.

Much like in the case of bremsstrahlung, synchrotron radiation can be described classically as a continuous energy loss, or quantum mechanically as a discrete emission process. The classical treatment is useful for analytic scaling laws, while the quantum description provides a more accurate evolution of the electron distribution function with straggling effects [47].

2.4.1 Classical synchrotron emission

The synchrotron radiation produced by electrons as they execute circular orbits in constant magnetic fields can be described classically using the classical radiation double-differential cross section (2.21) [33]. It can be shown through integration by parts that (2.21) is equivalent to the radiated energy double differential

$$\frac{d^2W}{d\Omega d\omega} = \frac{e^2\omega^2}{16\pi^3\epsilon_0 c}\left|\int_{-\infty}^{\infty} \hat{\boldsymbol{n}} \times (\hat{\boldsymbol{n}} \times \boldsymbol{\beta}) e^{i\omega(t-\hat{\boldsymbol{n}}\cdot\boldsymbol{r}/c)} dt\right|^2 . \tag{2.53}$$

As the electron traces circular motion with some radius ρ, let us define the electron position $\boldsymbol{r}$ such that

$$\boldsymbol{r} = \begin{bmatrix} \rho \sin\left(\frac{\beta ct}{\rho}\right) \\ \rho\left(1 - \cos\left(\frac{\beta ct}{\rho}\right)\right) \\ 0 \end{bmatrix} \tag{2.54}$$

which ensures the electron is restricted to the $x-y$ plane, passing the origin at time $t = 0$. Let the centre of the circle be positioned such that the observation point $\hat{\boldsymbol{n}}$ lies in the x-z

plane, with position

$$\hat{\boldsymbol{n}} = \begin{bmatrix} \cos\theta \\ 0 \\ \sin\theta \end{bmatrix} \tag{2.55}$$

for an observation point at some angle θ to the plane of the electron orbit. Radiation from relativistic electrons points into a cone of $\theta_{rms} = 1/\gamma$, with cone axis parallel to the electron velocity. Hence, we may use the small angle approximation for θ in (2.55), as radiation at large angles will be negligible for relativistic particles. Let us also define two additional vectors $\boldsymbol{\epsilon}_{\parallel}$ and $\boldsymbol{\epsilon}_{\perp}$ which, when combined with $\hat{\boldsymbol{n}}$, form a set of mutually perpendicular unit vectors (with $\boldsymbol{\epsilon}_{\parallel}$ pointing along the y-axis). The vector terms in (2.53) then reduce to

$$\hat{\boldsymbol{n}} \times (\hat{\boldsymbol{n}} \times \boldsymbol{\beta}) = \beta \left(-\boldsymbol{\epsilon}_{\parallel} \sin\left(\frac{\beta ct}{\rho}\right) + \boldsymbol{\epsilon}_{\perp} \cos\left(\frac{\beta ct}{\rho}\right) \sin(\theta) \right) \tag{2.56}$$

$$\omega \left(t - \frac{\hat{\boldsymbol{n}} \cdot \boldsymbol{r}}{c} \right) = \omega \left(t - \frac{\rho}{c} \sin\left(\frac{\beta ct}{\rho}\right) \cos(\theta) \right) \tag{2.57}$$

which yield

$$\frac{d^2W}{d\Omega d\omega} = \frac{e^2}{12\pi^3 \epsilon_0 c} \left(\frac{\omega\rho}{c}\right)^2 \left(\frac{1}{\gamma^2} + \theta^2\right)^2 \left(K_{2/3}^2(\xi) + \frac{\theta^2}{(1/\gamma^2) + \theta^2} K_{1/3}^2(\xi) \right) \tag{2.58}$$

in the small angle approximation, where ξ takes the form

$$\xi = \frac{\omega\rho}{3c} \left(\frac{1}{\gamma^2} + \theta^2\right)^{3/2} \tag{2.59}$$

and $K_i(\xi)$ are the i-th order modified Bessel functions of the second kind. These Bessel functions are negligible for $\xi \gg 1$, and so a critical frequency, ω_c may be defined for $\xi = 1/2$, $\theta = 0$ such that

$$\omega_c = \frac{3}{2} \frac{c}{\rho} \gamma^3. \tag{2.60}$$

Finally, the frequency distribution of radiated energy may be obtained by integrating (2.58) over all solid angles, which gives

$$\frac{dW}{d\omega} = \sqrt{3} \frac{e^2}{4\pi\epsilon_0 c} \gamma f_{sync} \left(\frac{\omega}{\omega_c}\right). \tag{2.61}$$

Here, the classical synchrotron emissivity, f_{sync} [33, 46] is given by

$$f_{sync}(y) = y \int_y^\infty K_{5/3}(x)dx \tag{2.62}$$

which is a useful function for comparisons with the quantum description of synchrotron radiation.

2.4.2 Quantum synchrotron emission

While bremsstrahlung radiation is described in terms of an emission cross section, the expressions for synchrotron radiation describe emission rates. These rates can be calculated if the basis states of the system are known. When dealing with charged particles in external electromagnetic fields, we may use the Furry states to describe the system [48, 49].

In general the photon emission rates for a relativistic electron in an external field are complicated, but there are approximations which simplify this treatment [46, 47]. Firstly, the external fields are assumed to remain unchanged over the course of the emission, which holds if the characteristic length scale of the emission is smaller than the length scale of field variation. For electrons in a monochromatic laser field, this implies the normalised vector potential a_0 satisfies

$$a_0 = \frac{eE_0\lambda_L}{2\pi m_e c^2} \gg 1 \tag{2.63}$$

where E_0 and λ_L are the peak electric field and wavelength of the laser respectively [46, 47].

Within the quasi-static (large a_0) approximation, the photon emission rates are governed by three dimensionless Lorentz invariant quantities: η from (2.52), and

$$F = \frac{|E^2 - c^2B^2|}{E_s^2} \tag{2.64}$$

$$G = \frac{|\mathbf{E} \cdot c\mathbf{B}|}{E_s^2}. \tag{2.65}$$

The photon emission rate is further simplified in the weak-field approximation, which eliminates the dependence on F and G provided $F \ll 1$, $G \ll 1$, and $\eta^2 \gg \max(F, G)$ [46, 47]. When both the quasi-static and weak-field approximations are applied, different field structures will give rise to the same photon emission behaviour provided they share the same η. While synchrotron radiation traditionally refers to emission from electrons in a constant

magnetic field, when its equations are expressed in terms of η they will apply to all electromagnetic configurations within the approximation limits [46]. This is the motivation for using "synchrotron radiation" as an umbrella term for the radiation mechanisms at the start of Section 2.4.

The differential photon emission rate for synchrotron radiation is given by

$$\frac{d^2N_\gamma}{d\chi dt} = \frac{\sqrt{3}m_e c^2}{h}\alpha\frac{cB}{E_s}\frac{F(\eta,\chi)}{\chi} \tag{2.66}$$

where the emitted photon energy is parametrised by χ, $F(\eta,\chi)$ represents the quantum synchrotron emissivity [50], and α is the fine structure constant. The χ parameter may be written as

$$\chi = \frac{\hbar}{2E_s m_e c}\left|(\mathbf{k}\cdot\mathbf{E})^2 - \left(\left|\frac{\omega\mathbf{E}}{c} + \mathbf{k}\times c\mathbf{B}\right|^2\right)\right|^{1/2} \tag{2.67}$$

for a photon of angular frequency ω and wavevector $\mathbf{k}$, and can be considered the photon equivalent of the electron η. Hence, $d^2N_\gamma/d\chi dt$ describes both the rate of radiated photon production, and the energy spectrum of these photons in a particular (E,B) field configuration. The parameter $F(\eta,\chi)$ takes the form

$$F(\eta,\chi) = \frac{4\chi^2}{\eta^2}yK_{2/3}(y) + \left(1-\frac{2\chi}{\eta}\right)y\int_y^\infty dtK_{5/3}(t) \tag{2.68}$$

where y is $4\chi/(3\eta^2 - 6\eta\chi)$. The total rate of photon production can be determined through integrating (2.66) over all χ, which yields

$$\frac{dN_\gamma}{dt} = \frac{\sqrt{3}m_e c^2}{h}\alpha\frac{\eta}{\gamma}\int_0^{\eta/2} d\chi\frac{F(\eta,\chi)}{\chi} \tag{2.69}$$

where the upper integral limit for χ occurs when the emitted photon energy $\hbar kc$ is equal to the electron kinetic energy (approximately $\gamma m_e c^2$ for ultra-relativistic electrons). Substituting $\gamma m_c c^2$ into the χ definition (2.67) yields an upper limit equivalent to $\eta/2$ [47].

2.4.3 Gaunt factor

The quantum treatment of synchrotron radiation reveals an inconsistency when compared to a treatment using classical methods. In the classical picture, $h \to 0$ and there is no

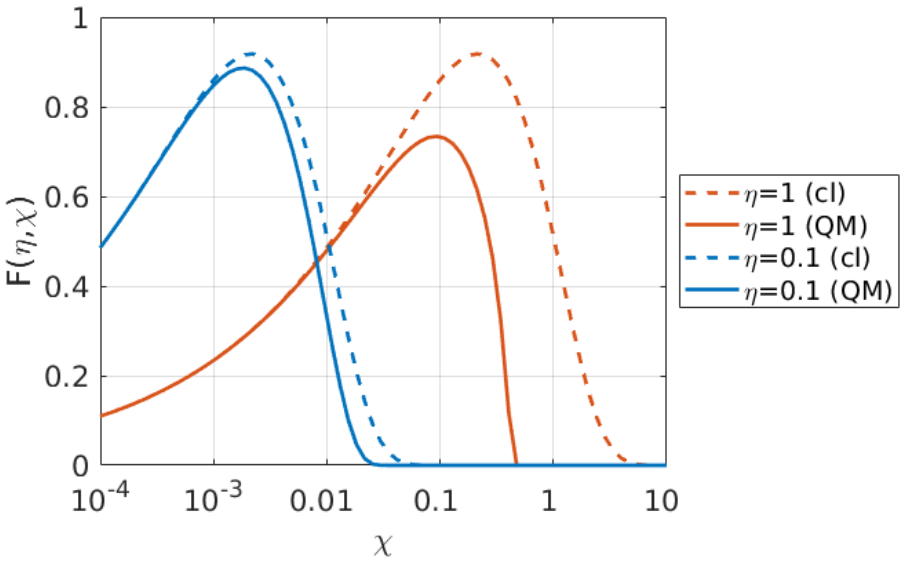

Figure 2.3: The synchrotron emissivity function $F(\eta, \chi)$ evaluated at different η. The solid curves represent the quantum $F(\eta, \chi)$, and the dashed curves denote the classical equivalent $f_{sync}(4\chi/3\eta^2)$. Figure adapted from Kirk *et al* [46].

concept of photon energy. As a result, the classical emissivity (2.62) over-estimates the emission by high energy photons when compared to the quantum case, and even allows for the non-physical emission of photons with energy greater than the incident electron. These differences are illustrated in Figure 2.3 for various η and χ values. The classical expression for radiated power is therefore an over-estimate, which also applies to the Landau-Lifshitz forumla (2.51). To correct this, a semi-classical Gaunt factor may be introduced [46, 51].

The Gaunt factor, $g(\eta)$ is defined as the ratio between the quantum and classical emissivities for synchrotron radiation, integrated over all photon energies. It can be seen that as $h \to 0$, the quantum emissivity (2.68) reduces to its classical form (2.62) for $y = 4\chi/3\eta^2$. Hence

$$g(\eta) = \frac{\int_0^{\eta/2} F(\eta, \chi) d\chi}{\int_0^{\infty} f_{sync}\left(\frac{4\chi}{3\eta^2}\right) d\chi} = \frac{3\sqrt{3}}{2\pi\eta^2} \int_0^{\eta/2} F(\eta, \chi) d\chi \tag{2.70}$$

which may be approximated [51], to the form

$$g(\eta) \approx (1 + 4.8(1+\eta)\ln(1+1.7\eta) + 2.44\eta^2)^{-2/3}. \tag{2.71}$$

Using this Gaunt factor, a semi-classical form of the Landau-Lifshitz force (2.51) may be

approximated as $F_{LL}g(\eta)$.

2.5 X-ray sources

There are many techniques capable of generating high energy X-rays, with each tailored for particular energy ranges and brightnesses [18]. Despite the wide array of configurations, the basic idea is shared across most methods (with the exception of sources based on electron-positron annihilation): a high energy beam of electrons is created, which is then directed to some converter region where acceleration is applied and radiation is generated.

X-rays over 1 MeV are of particular interest, as these can trigger nuclear processes because they are of similar energy to transitions between nuclear states. For example, 1.32 MeV photons could excite a tin vibrational state, and 8 MeV photons can trigger the proton emission of lead [18]. Giant dipole resonances of heavy nuclei may be excited by photons in the range 10-30 MeV, which can trigger the photo-fission of nuclear waste, or generate medical isotopes [10, 11]. X-rays around energies 9-10 MeV may also be used in special nuclear material (SNM) detection for defence and security applications, as these cause SNM to eject neutrons which may be detected [8]. This section provides only a brief overview of the methods used to generate high energy X-rays, with references provided for further reading.

2.5.1 Synchrotrons and free-electron lasers

Synchrotrons and free-electron lasers (FEL) can provide brilliant sources of low-energy X-rays using synchrotron radiation. A high energy electron beam is directed through an undulator, which consists of many tightly-packed magnets stacked in a row. Undulator magnets are arranged such that the magnetic fields of adjacent magnets point in opposite directions. Synchrotron radiation is produced as the electrons wiggle through this magnetic field configuration, which is shown schematically in Figure 2.4. The Diamond light source [52], along with PETRA-III at DESY [6] are examples of synchrotron sources. In an FEL set-up, the electron beam collapses into *microbunches* which radiate in phase with each other, leading to constructive superposition of the radiation generated and high gain [53, 54]. Examples of FEL sources include FLASH at DESY [55], and LCLS at SLAC [56].

Synchrotron sources are capable of producing brilliant beams of radiation up to photon

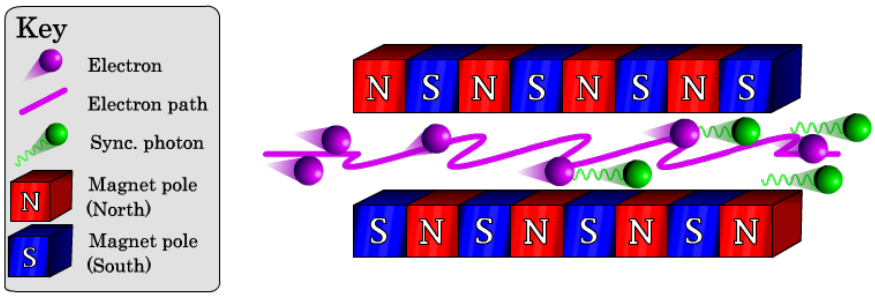

Figure 2.4: A schematic diagram of electrons emitting synchrotron-like radiation in an undulator.

energies of many keV, with PETRA-III operating within the range 30-200 keV [6]. Photons of these energies can penetrate deeply into materials while minimising radiation damage, and so find many applications in material science, including stress mapping, texture studies, and probing dynamic mechanical behaviours in manufacturing processes [6, 57]. The LCLS FEL typically produces photons of lower energy, in the range 0.8-8 keV [56], with an emphasis on tracking ultra-fast dynamical processes [58].

2.5.2 Betatron

Betatron radiation refers to the X-rays produced when laser pulses pass through gas targets and establish wakefields [59, 60], and is shown diagrammatically in Figure 2.5. The laser pulse ionises the gas as it passes through, and the ponderomotive force of the laser fields push electrons away from the laser axis, which creates a positively charged ion channel behind the pulse. The plasma electrons ejected from the beam path then undergo transverse oscillations across the ion channel, which is equivalent to electron wiggling in undulator fields. Hence, a synchrotron-like spectrum of X-rays is produced.

The betatron process creates a broadband radiation source up to a critical photon energy, $E_c \propto \gamma^2 n_e r_0$, where n_e is the background plasma-electron number density, and γ and r_0 are the Lorentz factor and oscillatory amplitude of the electrons respectively [59]. This cut-off occurs for photon energies at a few tens of keV for the n_e of traditional betatron sources, as a further increase of n_e reduces laser propagation speed and affects electron acceleration. Ferri *et al* address this problem with a two stage betatron source capable of reaching MeV photon

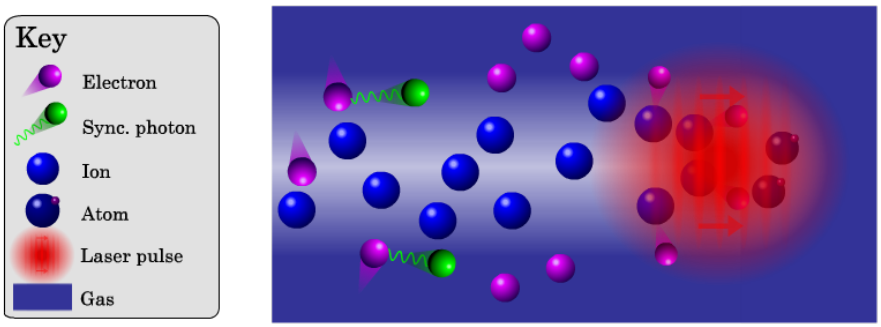

Figure 2.5: A schematic diagram showing the laser-driven formation of an ion channel in a gas target, which electrons oscillate through to create synchrotron-like betatron radiation.

energies [19]. Electrons are pre-accelerated via wakefield acceleration through low density plasma, and are then injected into a high density region where they drive wakefields which can produce high energy photons. This set-up is expected to produce a brilliance of 4×10^{23} photons/s/mm^2/mrad^2/0.1%BW, and convert 1% of the laser energy into X-rays [19].

2.5.3 Bremsstrahlung

Bremsstrahlung radiation is created as high energy electrons traverse through the fields of atomic or ionic nuclei. The cross section per nucleus is proportional to Z^2 (2.36), so the photon characteristics will have a strong dependence on the chosen material. In practice, electrons pass through an accelerator and are directed into foil converter targets [61, 62], as shown in Figure 2.6. The target thickness is chosen to maximise photon emissions from the electrons, but also to minimise photon attenuation inside the target.

The photon energy distribution of bremsstrahlung radiation is dependent on the energy of the incident electrons, and so bremsstrahlung radiation can be used in many different energy regimes. In medicine, linear accelerators a few metres in size are used to create electron beams with energies of a few MeV. These are directed onto high Z converter targets, and the resultant bremsstrahlung X-rays can be used for imaging or radiotherapy [7].

The PrimEx [61] and GlueX [62] collaborations at the Jefferson Lab obtained photon energies from 5-9 GeV, using electron beams accelerated to 5.76 GeV and 12 GeV respectively [62, 63]. The absolute number of bremsstrahlung photons moving towards the target can be deduced from photon-tagging. In PrimeEx, electrons emerging from the rear side of

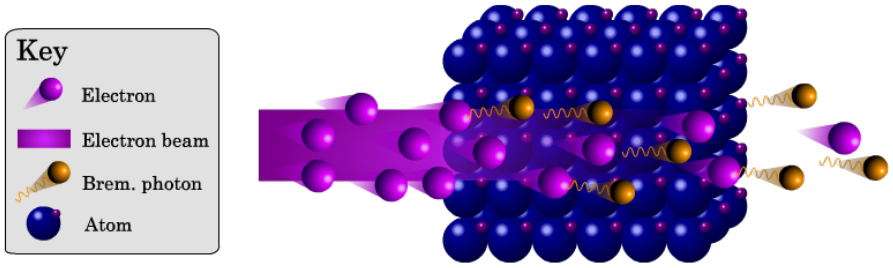

Figure 2.6: A schematic diagram of an electron beam colliding with a solid target, producing bremsstrahlung X-rays.

the Au converter are bent into detectors where their energy is counted, which allows the corresponding bremsstrahlung photon energy to be calculated. These detailed photon counts are used to calculate photo-production cross sections for nuclear and particle physics [61,64].

2.5.4 Positron annihilation

High energy photons can also be created in annihilation events, $e^- + e^+ \rightarrow 2\gamma$, and a set-up which has been used to create annihilation photon beams in the past is illustrated in Figure 2.7 [65]. In these experiments, an electron beam passes through an accelerator and strikes a thick, high Z converter target, producing copious bremsstrahlung radiation. These high-energy photons undergo Bethe-Heitler pair production within the target, and beams of e^-, e^+ and γ-rays exit the target rear. The e^+ beam is selected for through electric or magnetic field set-ups, and is directed at a secondary annihilation target with low Z to suppress bremsstrahlung radiation. This creates a photon beam which is closer to mono-energetic than a typical bremsstrahlung spectrum.

Precise estimates of these yields may be determined through photon-tagging, as two γ-rays are produced in each annihilation event. When directed at a reaction chamber, the number of beam photons which undergo a reaction can be estimated through comparison of the photon beam exiting chamber, and the secondary annihilation photons which never entered the chamber. This is useful information for experiments measuring photo-nuclear cross-sections [65, 66].

The Saclay linear accelerator set-up is capable of producing 300 MeV photons ($\pm$25 MeV)

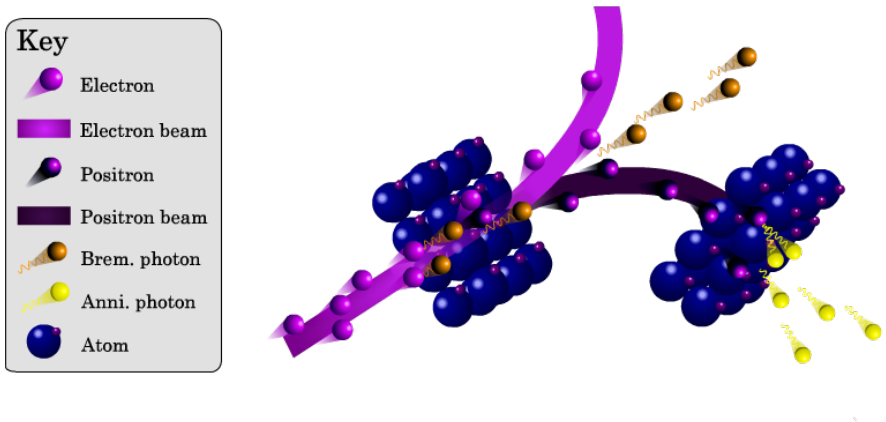

Figure 2.7: A schematic diagram depicting an incident electron beam striking a converter target and generating positrons, which are magnetically steered into a second target to produce annihilation photons.

at a flux of 10^4 photons per second as reported by Argan *et al* [67]. Using characterisations in their paper, we estimate a brilliance of $\sim 4 \times 10^{-6}$ photons/s/mm^2/mrad^2/0.1%BW. This is very low when compared to other sources, and can be attributed to the use of more than one converter stage in this set-up.

2.5.5 Compton scatter

Compton scatter refers to the X-rays generated when high energy electrons interact with photons. This is often distinguished from Thomson scatter in the literature, which describes the same process but for systems where the quantum effects like photon recoil are negligible [18, 68].

One of the more recent laser Compton backscatter sources has been proposed by IHEP, and is shown schematically in Figure 2.8. The facility currently under construction will direct a 0.2-2.5 GeV electron beam from a linear accelerator into a head-on collision with multi-picosecond laser-pulses (of energy 0.5-1.0 J) [69]. This set-up is expected to achieve photon energies between 1 and 111 MeV, and will aim to study photo-nuclear physics, transmutation of long-lived isotopes, and QED effects like Breit-Wheeler pair production in photon-photon collisions [69].

A slightly different Compton scatter scheme is performed by the HIγS (the high intensity gamma source) synchrotron, which generates X-rays through Compton backscatter in an FEL optical cavity [70, 71]. Here, a primary electron bunch generates X-rays via the FEL process,

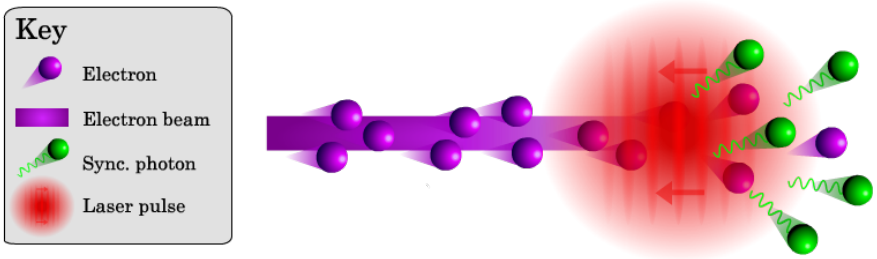

Figure 2.8: A schematic diagram showing X-rays generated by colliding an electron beam with a counter-propagating laser pulse.

and a second electron bunch collides head on with the FEL photons [72]. This allows the creation of significantly higher photon energies than those generated by a standard FEL set-up, reaching between 1 and 100 MeV [71].

Chapter 3

Laser-solid interactions

In Chapter 2, we briefly discussed the different physical mechanisms responsible for generating high energy X-rays, along with some set-ups which can achieve this radiation. We now turn our attention to the system of interest in this thesis: high-intensity short-pulse laser-solid interactions. The detailed physics involved when a high-intensity laser pulse strikes a solid target is shown in Figure 3.1.

In these interactions, there is sufficient energy to ionise atoms on the solid target and form a plasma on the target-surface. The ions and electrons of the plasma are accelerated by the external fields of the laser pulse, and emit synchrotron radiation. Both ions and electrons are accelerated by the laser, although the lighter electrons achieve greater speeds than the heavier ions, and are injected into the solid.

This injected current produces bremsstrahlung radiation as the high energy (hot) elec-

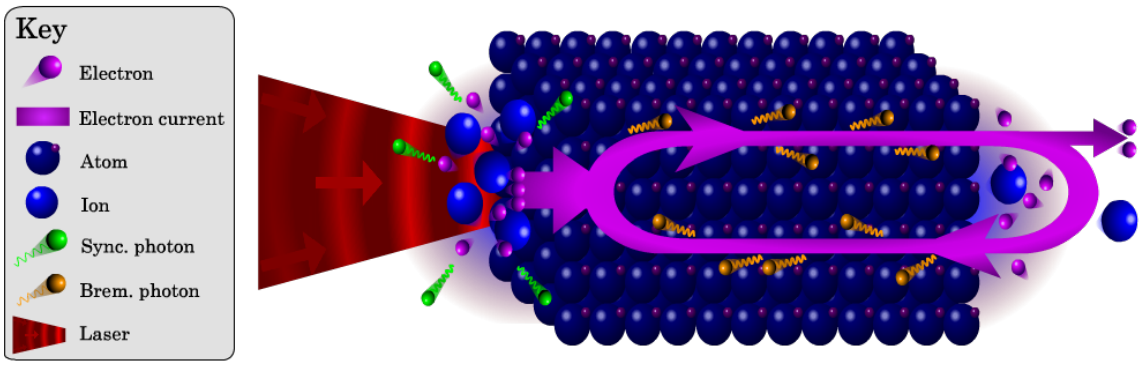

Figure 3.1: A schematic diagram of a laser-solid interaction.

trons interact with the electric fields of atomic nuclei [73–75]. Electrons may also lose energy in non-radiative collisions, where energy is spent exciting atomic electrons and raising the temperature of the solid (ionisation energy loss). The propagation of hot electrons though a resistive material also generates return currents and fields which oppose the electron motion, and energy is lost to the target in the form of Ohmic heating. Additionally, hot electrons may scatter within the target through elastic collisions with the atoms which comprise the solid target, or may bend through magnetic fields established by the moving charges.

Once electrons have traversed the target, they can pass through the rear surface and the highest energy electrons may escape. However, the build-up of negative charge beyond the target as hot electrons keep passing through will eventually create a sheath field, which can be strong enough to reflect hot electrons arriving later back into the target [75, 76]. These sheath fields are also capable of accelerating ions from the target out into the vacuum, providing a source of energetic ions.

The remaining sections in this chapter cover the particular processes outlined above, describing the physics of the pre-plasma, important laser parameters, and electron transport within the solid. An investigation into the behaviour of hot electrons traversing sheath fields is present in Chapter 5.

3.1 Plasma physics

The beams produced by petawatt class lasers have sufficient energy to ionise the front surface of a solid target into a plasma. Hence, a thesis on laser-solid interactions necessitates a discussion of plasma physics. A plasma is an ensemble of negatively charged electrons and positively charged ions, where particles are distributed through space like a gas, but also experience long-range electro-magnetic forces.

There are several concepts in plasma physics which are useful in describing laser-plasma interactions. The Debye length sets a typical length-scale for important processes in a plasma, and the time-scale of plasma dynamics may be expressed in terms of the plasma frequency. Whether or not a laser pulse can propagate through a plasma depends on the critical density, which has a relativistic correction for high intensity lasers. This section will delve into these concepts to provide greater insight into plasma behaviour, and also to pre-define terms which will be useful in subsequent sections.

3.1.1 Debye length

The electric field from a charged particle extends out to long ranges, and so one may assume that the dynamics of a particular plasma particle will be governed by all other particles in the plasma. In practice, the electric field around a plasma particle drops off faster than it would in a vacuum due to Debye shielding [36].

Charged particles in a plasma will repel like-charges and surround themselves with opposite charges, such that any particular region in the plasma appears neutral on average. The time-independent fields around the plasma satisfy Poisson's equation

$$\nabla^2\phi = -\frac{\rho}{\epsilon_0} \tag{3.1}$$

where we have substituted the time-independent form of the scalar potential definition (2.6) into Gauss' law (2.1). For a charge, Q at position, $\boldsymbol{r}$ surrounded by a plasma of protons and electrons, the charge density, ρ may be expressed as

$$\rho(\boldsymbol{r}) = (n_p(\boldsymbol{r}) - n_e(\boldsymbol{r}))e + Q\delta(\boldsymbol{r}) \tag{3.2}$$

where n_p and n_e denote the proton and electron number densities respectively. These may be evaluated using the Boltzmann distribution, giving

$$n_p = \langle n \rangle e^{e\phi/k_BT} \tag{3.3}$$

$$n_e = \langle n \rangle e^{-e\phi/k_BT} \tag{3.4}$$

where we have assumed both species are at the same temperature, T, and have the same number densities, $\langle n \rangle$ when averaged over a large enough volume. The proton number density (3.3) is often ignored, as electrons will have a greater speed than protons (or heavier ions) at a given temperature, so over short time-scales it is the electrons which move to neutralise local charge [77]. For small potentials $|e\phi| \ll k_BT$, we may use the expansion $e^x \approx 1 + x$ on the exponential in (3.4), and substituting resultant charge density into (3.1) yields

$$\nabla^2\phi = \frac{e^2\langle n \rangle}{\epsilon_0 k_B T}\phi - \frac{Q}{\epsilon_0}\delta(\boldsymbol{r}) \tag{3.5}$$

where we have neglected the proton contribution to the charge density ρ.

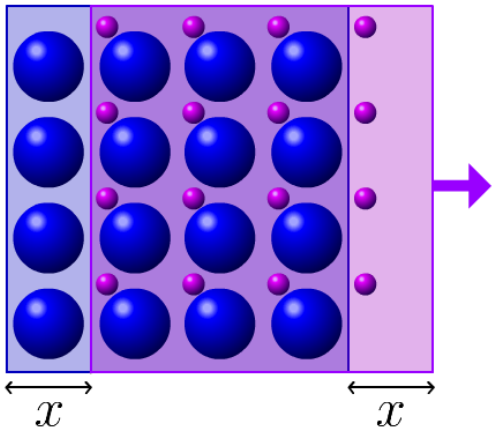

Figure 3.2: A schematic diagram depicting a displacement of ion and electron populations in a plasma by distance x.

Assuming a spatially uniform proton charge density yields a potential of the form (2.33) with the electron Debye length quoted in (2.34). In general, for a plasma consisting of multiple ion species, α, each with their own temperature T_α, number density, n_α and ionisation state Z_α, the Debye length may be written

$$\frac{1}{\lambda_D^2} = \frac{e^2}{\epsilon_0 k_B}\left(\frac{n_e}{T_e} + \sum_\alpha \frac{n_\alpha Z_\alpha^2}{T_\alpha}\right) \tag{3.6}$$

for a sum over all ion species α, where all terms have been retained in the charge density, ρ [77].

3.1.2 Plasma frequency

The charged particles in a plasma will arrange themselves so as to make the charge density appear neutral when averaged over large volumes (quasi-neutral). If the negative charges were displaced from the positive charges, then electric fields would be established to restore quasi-neutrality. In a simple system, the restoring forces set-up simple harmonic motion, with the plasma frequency, ω_p describing the frequency of the oscillations [36].

To quantify this, consider a quasi-neutral plasma composed of positive ions and negative electrons, surrounded by vacuum. If all electrons are all displaced in the same direction by some length x, the electrons at one end of the plasma will move into the vacuum as shown in Figure 3.2. This builds up a negative charge per unit area of $en_e x$ on the electron side, where n_e is the electron number density. On the other side of the plasma, electrons will

move away exposing a positively charged region with a charge density of equal magnitude.

The electric field between these positive and negative regions is calculated from Gauss' law to be

$$E = \frac{en_e x}{\epsilon_0} \tag{3.7}$$

which results in the electron acceleration

$$\frac{d^2x}{dt^2} = -\frac{e^2 n_e}{\epsilon_0 m_e} x \tag{3.8}$$

where we recognise simple harmonic motion with frequency

$$\omega_p = \sqrt{\frac{e^2 n_e}{\epsilon_0 m_e}}. \tag{3.9}$$

We have assumed immobile ions in this derivation, as ion acceleration in the same electric field will be a factor m_i/m_e smaller for ions of mass m_i (about 1836 times smaller for the case of a hydrogen plasma).

3.1.3 Critical density

In a laser-solid interaction, the laser pulse moves towards the target and strikes the pre-plasma, which typically has a lower particle density than the solid. While the laser pulse can pass through a low density plasma, eventually a critical density is reached where propagation ceases, and the laser is reflected. This critical density may be determined by considering the phase velocity of the light wave in the plasma medium [78].

To start, we consider the non-relativistic evolution of the plasma phase-space density $f(\boldsymbol{r}, \boldsymbol{v}, t)$, where $f(\boldsymbol{r}, \boldsymbol{v}, t) d^3\boldsymbol{r} d^3\boldsymbol{v}$ denotes the number of particles within the phase-space volume $d^3\boldsymbol{r} d^3\boldsymbol{v}$ at position $\boldsymbol{r}$, velocity $\boldsymbol{v}$ and time t. The Boltzmann transport equation describes the total time derivative of f, and may be expressed as

$$\frac{\partial f}{\partial t} + (\boldsymbol{v} \cdot \nabla_x) f + \frac{1}{m} (\boldsymbol{F} \cdot \nabla_v) f = \left(\frac{\partial f}{\partial t} \right)_{\text{coll}} \tag{3.10}$$

where ∇_x and ∇_v denote the gradient vectors in position and velocity space respectively. Here $\boldsymbol{F}$ is the force acting on a plasma particle of mass m, and the RHS term describes

the change in f due to collisions. The time evolution of a velocity-dependent observable quantity, $Q(\boldsymbol{v})$ is found by applying $\int_v d^3\boldsymbol{v}Q(\boldsymbol{v})$ to both sides of (3.10), which yields

$$\frac{\partial}{\partial t}(n\langle Q\rangle_v) + \nabla_x \cdot (n\langle \boldsymbol{v}Q\rangle_v) - \frac{n}{m}\langle \nabla_v \cdot (\boldsymbol{F}Q)\rangle_v = \int_v d^3\boldsymbol{v}Q\left(\frac{\partial f}{\partial t}\right)_{\text{coll}} \tag{3.11}$$

where $\langle ...\rangle_v$ denotes an average over velocity space.

Setting $Q = 1$ yields the continuity equation

$$\frac{\partial n}{\partial t} = -\nabla_x \cdot (n\langle \boldsymbol{v}\rangle_v) \tag{3.12}$$

and using $Q = m\boldsymbol{v}$ gives an expression for the momentum evolution

$$m\left(n\frac{\partial \langle \boldsymbol{v}\rangle_v}{\partial t} + (\langle \boldsymbol{v}\rangle_v \cdot \nabla_x)(n\langle \boldsymbol{v}\rangle_v)\right) = nq(\boldsymbol{E} + \langle \boldsymbol{v}\rangle_v \times \boldsymbol{B}) - \nabla_x \cdot \Psi + \boldsymbol{P} \tag{3.13}$$

for particles of charge q. In evaluating (3.13), we have split $\boldsymbol{v}$ into the sum $\langle \boldsymbol{v}\rangle_v + \tilde{\boldsymbol{v}}$, where $\tilde{\boldsymbol{v}}$ describes velocity fluctuations about the mean and has $\langle \tilde{\boldsymbol{v}}\rangle_v = 0$. The Ψ term describes the stress tensor, defined such that

$$\nabla_x \cdot \Psi = \frac{\partial}{\partial x}(nm\langle \tilde{v_x}\tilde{\boldsymbol{v}}\rangle_v) + \frac{\partial}{\partial y}(nm\langle \tilde{v_y}\tilde{\boldsymbol{v}}\rangle_v) + \frac{\partial}{\partial z}(nm\langle \tilde{v_z}\tilde{\boldsymbol{v}}\rangle_v) \tag{3.14}$$

and may be neglected in uniform plasmas with no pressure gradients. Also in (3.13), the Lorentz force is used for $\boldsymbol{F}$, and the average momentum change through collisions is written as $\boldsymbol{P}$, where

$$\boldsymbol{P} = \int_v d^3\boldsymbol{v}\left(\frac{\partial f}{\partial t}\right)_{\text{coll}} m\boldsymbol{v}. \tag{3.15}$$

As a first approximation, neglecting $\boldsymbol{B}$, Ψ, $\boldsymbol{P}$ and non-linear terms, a set of equations for electron and ion evolution in an electric field may be written as

$$n_e\frac{\partial \boldsymbol{v}_e}{\partial t} = -\frac{en_e}{m_e}\boldsymbol{E} \tag{3.16}$$

$$n_i\frac{\partial \boldsymbol{v}_i}{\partial t} = \frac{Zen_i}{m_i}\boldsymbol{E} \tag{3.17}$$

where subscripts e and i have been used for electron and ion quantities respectively, and the $\langle ...\rangle_v$ brackets have been dropped for brevity. Performing $Z(3.16)-(3.17)$ yields an expression

for the current response to an electric field

$$\frac{\partial \boldsymbol{J}}{\partial t} = \left(\frac{n_i Z^2 e^2}{m_i} + \frac{n_e e^2}{m_e} \right) \boldsymbol{E} \tag{3.18}$$

where total current density $\boldsymbol{J} = Z e n_i \boldsymbol{v}_i - n_e e \boldsymbol{v}_e$.

The propagation of a laser pulse is described by Maxwell's equations (2.1)-(2.4), and comparing $\nabla \times$(2.3) to ∂(2.4)$/\partial t$ produces

$$\nabla^2 \boldsymbol{E} = \mu_0 \frac{\partial \boldsymbol{J}}{\partial t} + \frac{1}{c^2} \frac{\partial^2 \boldsymbol{E}}{\partial t^2} \tag{3.19}$$

where the term $\nabla \cdot \boldsymbol{E}$ has been removed as this is given by Gauss' law (2.1), and $\rho = 0$ for a quasi-neutral plasma. If the laser pulse is modelled as a plane wave with $\boldsymbol{E} = E_0 e^{i(kx - \omega t)} \hat{\boldsymbol{z}}$, then using the current evolution (3.18) in equation (3.19) yields

$$-k^2 E_z = \frac{\mu_0 n_e e^2}{m_e} E_z - \frac{\omega^2}{c^2} E_z \tag{3.20}$$

which may be re-arranged to obtain an expression for the laser phase velocity, v_p

$$v_p = \frac{c}{\sqrt{1 - \omega_p^2 / \omega^2}} \tag{3.21}$$

where $v_p = \omega / k$, and the plasma frequency ω_p is given by (3.9). When $\omega_p > \omega$, the phase velocity goes imaginary, and the laser pulse can no longer propagate through the plasma. This implies a critical electron number density, n_e^{crit} of the form

$$n_e^{\text{crit}} = \frac{4\pi^2 c^2 m_e \epsilon_0}{\lambda^2 e^2} \tag{3.22}$$

for a laser pulse of wavelength λ [78]. For the 1 µm wavelength lasers typically considered in this thesis, $n_e^{\text{crit}} = 1.1 \times 10^{27}$ m^{-3}. This places the critical density between the electron density of nitrogen gas at standard temperature and pressure, 3.8×10^{26} m^{-3}, and that of solid density aluminium, 7.8×10^{29} m^{-3}. For X-rays of energies 10 keV and 1 MeV, the critical densities are 7.3×10^{34} m^{-3} and 7.3×10^{38} m^{-3} respectively, and so X-rays are capable of propagation through far denser targets than laser photons.

3.1.4 Relativistic transparency

At high laser intensities, plasma electrons can achieve relativistic speeds which allows the laser pulse to propagate through greater densities than approximated by the non-relativistic critical density (3.22) [79,80]. Assuming all fields and electron momenta are functions of the phase $\tau = t - (z/v_p)$ for a plane wave travelling in the z direction with phase velocity v_p, Maxwell's equations (2.1)-(2.4) may be re-written as

$$-\hat{\boldsymbol{z}} \cdot \frac{d\boldsymbol{E}}{d\tau} = \frac{ev_p}{\epsilon_0}(n_0 - n_e) \tag{3.23}$$

$$\hat{\boldsymbol{z}} \cdot \frac{d\boldsymbol{B}}{d\tau} = 0 \tag{3.24}$$

$$-\hat{\boldsymbol{z}} \times \frac{d\boldsymbol{E}}{d\tau} = -v_p \frac{d\boldsymbol{B}}{d\tau} \tag{3.25}$$

$$-\hat{\boldsymbol{z}} \frac{1}{v_p} \times \frac{d\boldsymbol{B}}{d\tau} = -\mu_0 e n_e \boldsymbol{v} + \frac{1}{c^2} \frac{d\boldsymbol{E}}{d\tau} \tag{3.26}$$

with Lorentz force

$$\left(\frac{\hat{\boldsymbol{z}} \cdot \boldsymbol{v}}{v_p} - 1 \right) \frac{d\boldsymbol{p}}{d\tau} = e(\boldsymbol{E} + \boldsymbol{v} \times \boldsymbol{B}) \tag{3.27}$$

where n_0 is the number density of electrons at equilibrium. In writing these equations, we have assumed the electrons are initially immobile (thermal velocities are typically non-relativistic), and that the laser pulse is not strong enough to accelerate background ions to relativistic speeds [79].

From applying $\hat{\boldsymbol{z}}\cdot$(3.26), we find

$$n_e = \frac{n_0 v_p}{v_p - v_z} \tag{3.28}$$

and $\hat{\boldsymbol{z}}\times$(3.27) yields

$$\boldsymbol{B} = -\frac{1}{ev_p} \hat{\boldsymbol{z}} \times \frac{d\boldsymbol{p}}{d\tau}. \tag{3.29}$$

By comparing d(3.29)$/d\tau$ to $\hat{\boldsymbol{z}}\times$(3.26), momentum evolution equations can be found for the

transverse directions

$$\frac{d^2 p_x}{d\tau^2} = -\frac{e^2 n_e}{m_e \epsilon_0 \gamma} \frac{v_p^2}{v_p^2 - c^2} p_x \tag{3.30}$$

$$\frac{d^2 p_y}{d\tau^2} = -\frac{e^2 n_e}{m_e \epsilon_0 \gamma} \frac{v_p^2}{v_p^2 - c^2} p_y \tag{3.31}$$

where γ is the electron Lorentz factor, and we may also obtain

$$\frac{d^2}{d\tau^2}(\gamma m_e c^2 - v_p p_z) = \frac{e^2 n_0}{\epsilon_0} \frac{v_z v_p^2}{v_p - v_z} \tag{3.32}$$

from $d(\hat{\boldsymbol{z}}\cdot(3.27))/d\tau$. For pure transverse waves with $v_z = 0$, (3.32) shows $d\gamma/d\tau$ is constant, which implies γ is constant if we seek bounded solutions. This means (3.30) and (3.31) show simple harmonic motion in the transverse directions, with angular frequency

$$\omega = \frac{\omega_p}{\sqrt{\gamma}} \frac{v_p}{\sqrt{v_p^2 - c^2}} \tag{3.33}$$

and corresponding phase velocity

$$v_p = \frac{c}{\sqrt{1 - \omega_p^2/(\gamma\omega^2)}}. \tag{3.34}$$

As with the non-relativistic case (3.21), this wave may only propagate if the phase velocity is real, which requires $\omega\sqrt{\gamma} > \omega_p$. Hence, the relativistically corrected critical electron density may be written as

$$n_e^{\gamma,\mathrm{crit}} = \frac{4\pi^2 c^2 m_e \epsilon_0}{e^2 \lambda^2} \gamma = n_e^{\mathrm{crit}} \gamma \tag{3.35}$$

and so when electrons reach relativistic speeds, a laser pulse of a given wavelength can propagate through denser plasma than when electrons are cold.

3.2 High power lasers

The lasers of interest in this thesis are capable of producing high-energy, short-duration pulses, with peak powers approaching and exceeding 1 PW. A good review of worldwide petawatt-class laser facilities is given by Danson *et al* [81], and some examples include the

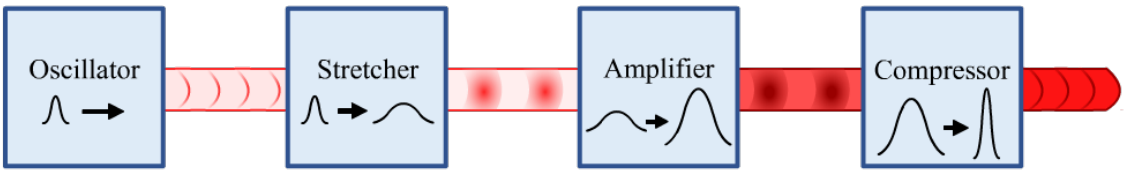

Figure 3.3: A schematic diagram describing the production of a high energy laser pulse, created using the chirped pulse amplification technique.

Vulcan PW laser [82], or 10 PW lasers like Apollon [24] and the extreme light infrastructure (ELI) [23].

The high powers achieved by modern lasers can be attributed to the chirped pulse amplification (CPA) technique [83], which typically involves the use of four components sketched out in Figure 3.3 [80]. An oscillator produces low energy, short-duration pulses with a large bandwidth, which are then temporally stretched out to reduce the energy density of the pulse. This is done to minimise damage to optical components, and can be achieved using diffraction gratings which give varying transmission times for waves of different wavelengths. The long pulse is then safely amplified, and compressed back to a short pulse using the optical inverse of the initial stretcher. Optical parametric chirped pulse amplification (OPCPA) [84] may enhance the laser power further, in which pre-amplified low-wavelength pulses are used to amplify low-energy high-wavelength pulses in materials with non-linear optical properties like KDP.

The pulses produced by petawatt-class lasers typically have durations with full width half maxima ranging from picoseconds to tens of femtoseconds, at wavelengths around 1 µm, with focal spot sizes of a few microns. A pulse from a 1 PW laser could reach intensities up to 10^{22} Wcm^{-2}, with next generation 10 PW lasers potentially exceeding 10^{23} Wcm^{-2}. The high-intensity main pulses from these lasers are often preceded by a nanosecond-duration lower-intensity pre-pulse, which is capable of ionising the solid target before the main pulse arrives, forming a pre-plasma [85]. The main pulse will then interact with the pre-plasma instead of the solid, although the size of this plasma layer can be reduced by minimising the pre-pulse using plasma mirror [86] or frequency doubling [87] techniques.

3.3 Laser absorption

Before considering the acceleration of plasma electrons under the influence of a laser field, let us first address the mechanism which allows a laser to convert solid atoms into plasma [80]. The wavelengths of petawatt-class lasers are typically around $\lambda = 1$ µm, and each laser photon carries an energy $E_\gamma = hc/\lambda$, or about 1 eV. The energy required to ionise a hydrogen atom is 13.6 eV, and so no individual laser photon is capable of ionisation. Instead, consider the electric field, E_a, which binds an electron to its proton in a hydrogen atom

$$E_a = \frac{e}{4\pi\epsilon_0 a_B^2} \approx 5.14 \times 10^{11} \text{ Vm}^{-1} \tag{3.36}$$

where the electron-proton spacing is taken to be the Bohr radius, a_B. The peak electric field of a laser pulse, E_0 is given by

$$E_0 = \sqrt{\frac{2I}{\epsilon_0 c}} \tag{3.37}$$

where I is the cycle-averaged laser intensity, and so laser fields become comparable to atomic fields at intensities around 4×10^{16} Wcm^{-2}. For petawatt class lasers exceeding intensities of 10^{20} Wcm^{-2}, E_0 dominates and the atomic fields are no longer capable of holding the atom together. This produces a pre-plasma, and solid atoms will continue to undergo field ionisation until the pre-plasma achieves critical density, as this prevents further laser propagation and shields the remaining solid atoms from ionisation.

The amount of laser energy absorbed by plasma electrons is complicated, depending on various laser and plasma parameters. Various models exist to describe the coupling of laser energy to hot electrons [80], including resonance absorption [88], vacuum heating [89], the anomalous skin effect [90], sheath inverse bremsstrahlung [91], and relativistic $\boldsymbol{J} \times \boldsymbol{B}$ heating (Wilks scaling) [92]. However, not all of these absorption mechanisms are important for petawatt class laser pulses. The following subsections discuss acceleration methods for plasma electrons in these laser fields.

3.3.1 Single electron motion in intense laser fields

To understand how electrons absorb laser energy, it is useful to discuss how a single electron responds to the fields of a laser, as covered by Gibbon [80]. For a general elliptically polarised

plane wave travelling in the x direction, the vector potential $\boldsymbol{A}$ takes the form

$$\boldsymbol{A} = \begin{pmatrix} 0 \\ A_0 \delta \cos(\phi) \\ A_0 \sqrt{1-\delta^2} \sin(\phi) \end{pmatrix} \tag{3.38}$$

where A_0 is the peak vector potential, the laser phase $\phi = \omega t - kx$, and δ is a constant between ± 1 which sets the polarisation. The rate of change of electron momentum may be expressed in terms of $\boldsymbol{A}$ by using the Lorentz force $\boldsymbol{F} = -e(\boldsymbol{E} + \boldsymbol{v} \times \boldsymbol{B})$ with the potential definitions (2.5) and (2.6), along with the electron power

$$\frac{d}{dt}(\gamma m_e c^2) = -e(\boldsymbol{v} \cdot \boldsymbol{E}). \tag{3.39}$$

This yields

$$\frac{dp_x}{dt} = m_e c \frac{d\gamma}{dt} \tag{3.40}$$

$$\frac{d\boldsymbol{p}_\perp}{dt} = e \frac{d\boldsymbol{A}_\perp}{dt} \tag{3.41}$$

with corresponding momenta

$$p_x = \frac{1}{4} a_0^2 m_e c \left(1 + \left(2\delta^2 - 1\right) \cos(2\phi)\right) \tag{3.42}$$

$$p_y = a_0 m_e c \delta \cos(\phi) + p_{y0} \tag{3.43}$$

$$p_z = a_0 m_e c \sqrt{1-\delta^2} \sin(\phi) + p_{z0} \tag{3.44}$$

where the dimensionless vector potential (pump strength (2.63)) $a_0 = eA_0/m_e c$, and p_{y0} and p_{z0} are constants of integration which represent the canonical momentum. Using the $\boldsymbol{A}$ definition (2.5), $A_0 = E_0/\omega$ for a plane wave of peak electric field E_0, and so a_0 is often written

$$a_0 = \sqrt{\frac{e^2}{2\pi^2 m_e^2 c^5 \epsilon_0} I\lambda^2} \approx 8.5 \times 10^{-6} \sqrt{I\lambda^2} \tag{3.45}$$

where I and λ are the intensity (Wm^{-2}) and wavelength of the laser pulse respectively.

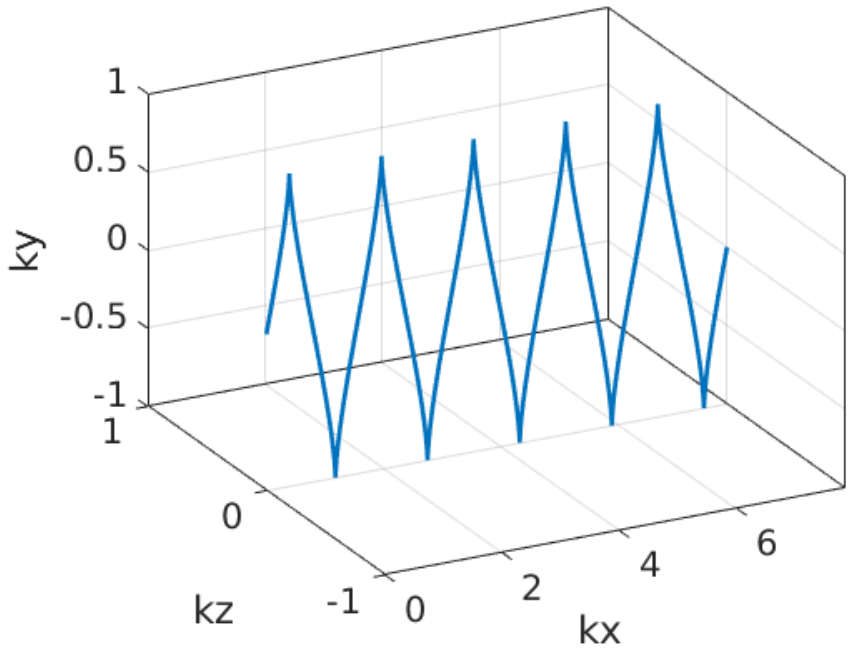

Figure 3.4: The trajectory of a single electron in a laser field, parametrised by $a_0 = \delta = 1$.

The momenta (3.42)-(3.44) may be integrated to obtain the trajectories

$$x = \frac{a_0^2}{4k}\left(\phi + \frac{1}{2}\left(2\delta^2 - 1\right)\sin(2\phi)\right) \tag{3.46}$$

$$y = \frac{a_0}{k}\delta\sin(\phi) \tag{3.47}$$

$$z = -\frac{a_0}{k}\sqrt{1-\delta^2}\cos(\phi) \tag{3.48}$$

where we have assumed that the electron initially has $p_x = 0$ and no canonical momentum. A typical trajectory has been plotted in Figure 3.4.

Equations (3.43) and (3.44) describe electron oscillation in the transverse direction, with (3.42) showing a longitudinal momentum consisting of both a drift term and an oscillatory term at twice the wave frequency. At high a_0, the motion is relativistic ($v \approx c$), and $p_x \gg p_\perp$. As momentum is transferred to the electron from many (n) laser photons travelling in the x direction, then $p_x = n\hbar k$ from momentum conservation. This implies $p_x = (\gamma - 1)m_e c$ for an electron which gains energy $(\gamma - 1)m_e c^2$, and comparing (3.42) to (3.43) and (3.44) gives

$$\tan(\theta) = \frac{p_\perp}{p_x} = \sqrt{\frac{2}{\gamma - 1}} \tag{3.49}$$

where θ denotes the peak ejection angle of an electron leaving the pulse [80, 93]. To achieve this escape angle, the electron must be ionised by the laser an instant when $\boldsymbol{A}$ is non-zero to allow for a non-zero canonical momentum, and the laser intensity must decrease with transverse distance from the pulse centre. The latter condition ensures the laser field strength decreases as the electron moves in the transverse direction, which prevents the electron fully returning to its original transverse displacement as in Figure 3.4. The process responsible for the growth of transverse electron momentum is referred to as the "ponderomotive force", which can carry the electron out of the laser pulse.

3.3.2 Wilks scaling

Multiple models exist for describing the absorption of laser light into high energy (hot) electrons [80], although the most common model used for intensities over 10^{18} Wcm^{-2} is that covered by Wilks *et al* [92]. In a series of 2D PIC simulations, Wilks *et al* discovered similarities between absorption in laser-solid simulations, and the single electron acceleration model which was covered in Section 3.3.1. For laser intensities in the range of 10^{18}-10^{19} Wcm^{-2}, it was found that the hot electron temperature scaled as

$$k_B T_e = \left(\sqrt{1 + \frac{I\lambda^2}{(I\lambda^2)_w}} - 1 \right) m_e c^2 \approx a_0 m_e c^2 \tag{3.50}$$

where $(I\lambda^2)_w = 1.37 \times 10^{18}$ Wμm^{2}cm^{-2} [92], and the approximation holds at high intensity. The high radiation pressure bores a hole through the critical density, and electron bunches are accelerated into the target twice per laser cycle, which matches the oscillation frequency in the vacuum p_x equation (3.42). Both electrons and ions are expected to accelerate in the laser propagation direction, but the lighter electrons achieve much greater speeds at our intensities of interest.

In the Wilks simulations, the absorption efficiency of laser energy to hot electron kinetic energy, $\eta_{l \to e}$ ranged from 10% to 50% for different target structures and pre-plasma conditions. These efficiencies also changed during the simulation as the critical density surface became warped [92].

3.4 Electron transport

Once the laser pulse ionises the front surface of the plasma and transfers some energy into a hot electron population, these electrons are injected into the solid. As the hot electrons pass through the electric fields of the solid nuclei, bremsstrahlung radiation can be produced as discussed in Section 2.2. This provides an energy loss mechanism, but it is not the only important process as the electrons traverse the solid. Non-radiative collisions can transfer hot electron energy to raising the target temperature, resistive return currents and Ohmic heating may be generated, along with a transfer of temperature between particle species. This section aims to describe the relevant physics pertaining to hot electron transport in solids.

3.4.1 Return current

The currents formed when laser-accelerated electrons pass through a solid can be very high. For example, a 10^{20} Wcm^{-2} laser pulse with a 40 fs duration, 1 µm wavelength and a focused area of 25 $\mu\mathrm{m}^2$ could deliver an energy of 1 J to a target placed at the focal spot. If 30% of this energy was absorbed by hot electrons with a mean energy $a_0 m_e c^2$, then there would be 4×10^{11} charge carriers, with a current of 2 MA [94].

Using the Ampère-Maxwell equation (2.4), it can be shown that the magnetic field inside a charged beam grows with radial distance, r from the beam centre. Alfvén showed that above some r, the magnetic field becomes so strong that the radius of curvature (gyroradius) becomes small enough to turn beam particles around, preventing forwards propagation and limiting the net forwards current [95]. The Alfvén-Lawson limit, I_{AL} is defined as a current where the gyroradius at the beam edge is half the beam radius, or

$$I_{AL} = \frac{4\pi}{q\mu_0} p \tag{3.51}$$

for beam particles of charge q and momentum p, which is equivalent to around $17000\gamma\beta$ Amperes [96, 97].

In our example I_{AL} is around 100 kA, which is significantly lower than the 2 MA estimate. Hence, some degree of current neutralisation is required to prevent the beam pinching and to allow the hot electrons to propagate. This implies a return current of thermal electrons must exist within the solid to balance out the fast electron current [94].

3.4.2 Resistivity

The resistivity, η_r of a solid determines the magnitude of the electric field created by the return current, and also determines the power dissipation in Ohmic heating. The definition of η_r comes from an equation linking the electrical current to the momentum transfer in collisions between particle species

$$\boldsymbol{P}_{ei} = \eta_r n_e e \boldsymbol{J} \tag{3.52}$$

where $\boldsymbol{P}_{ei}$ is defined in (3.15), and here refers to the electron response to collisions with ions [78]. Following the derivation of the reduced Boltzmann equations (3.16) and (3.17), but retaining the collisional $\boldsymbol{P}$ terms yields an expression for Ohm's law

$$\boldsymbol{E} = \eta_r \boldsymbol{J} \tag{3.53}$$

which describes the resistive fields generated from the currents in the solid.

Spitzer derives an order-of-magnitude estimate for η_r, by assuming extreme collisions where electrons of initial velocity $\boldsymbol{v}_e$ end up with the ion velocity $\boldsymbol{v}_i$ [78]. The average momentum transfer in one of these collisions is $\Delta p = m_e(\boldsymbol{v}_i - \boldsymbol{v}_e)$. For a collision rate per unit volume of n_e/τ where τ is the electron relaxation time, we have $\boldsymbol{P}_{ei} \approx \Delta p n_e/\tau$. Using this approximate form of $\boldsymbol{P}_{ei}$ in (3.52) yields the resistivity estimate

$$\eta_r = \frac{m_e}{n_e e^2 \tau} \tag{3.54}$$

for a current density $\boldsymbol{J} = e(n_i Z \boldsymbol{v}_i - n_e \boldsymbol{v}_e)$. Spitzer then considers a more complex model, using the Boltzmann equation (3.10) to calculate a more accurate current density. Electron-electron encounters were also included, yielding a resistivity of the form

$$\eta_r = \frac{\pi^{3/2} m_e^{1/2} Z^* e^2 \ln\Lambda}{2(2k_B T_e)^{3/2}(4\pi\epsilon_0)^2 \gamma_E} \tag{3.55}$$

where Z^* is the ion charge state, T_e is the plasma electron temperature, and γ_E is a correction factor which scales with Z^* ($\gamma_E = (0.582, 0.683, 0.785, 0.923, 1.000)$ for $Z^* = (1, 2, 4, 16, \infty)$, as given in Table 5.4 of Spitzer's textbook [78]).

A more detailed model for the resistivity is derived by Lee and More [98]. Here the

collisions are treated using a Coulomb-collision cross section, with cut-off parameters chosen to map the resistivity onto the results from quantum calculations which solve Schrödinger's equation. The Thomas-Fermi potential model is used in these quantum calculations, which describes degenerate electron behaviour in the electric fields of nuclei [99]. This results in a resistivity of the form

$$\eta_r = \frac{m_e}{Z^* n_i e^2 \tau A^\alpha} \tag{3.56}$$

where n_i is the ion number density of the background solid. The electron relaxation time for a plasma is given by

$$\tau = 24\pi\epsilon_0^2 \sqrt{\frac{m_e}{2}} \frac{(k_B T_e)^{3/2}}{(Z^*)^2 n_i e^4 \ln\Lambda} \left(1 + e^{-\mu/k_B T_e}\right) F_{1/2}\left(\frac{\mu}{k_B T_e}\right) \tag{3.57}$$

where $\ln\Lambda$ is the Coulomb logarithm, $F_{1/2}$ is a Fermi-Dirac integral of the form

$$F_j\left(\frac{\mu}{k_B T_e}\right) = \int_0^\infty \frac{t^j dt}{1 + e^{t-\mu/k_B T_e}} = -\frac{\sqrt{\pi}}{2} Li_{3/2}(-e^{\mu/k_B T_e}) \tag{3.58}$$

and $Li_{3/2}$ is a polylogarithm function of order 3/2 [98]. Lee and More present two models for calculating the electron relaxation time at temperatures below the plasma regime, with one requiring the melting temperature of the material and a fitting parameter. This model breaks down above the melting temperature, and is swapped out for

$$\tau = R_0 / v_e \tag{3.59}$$

where the ion sphere radius R_0 is given by

$$R_0 = (3/4\pi n_i)^{1/3} \tag{3.60}$$

and the mean electron speed v_e is calculated using the mean thermal velocity

$$v_e = \sqrt{3 k_B T_e / m_e}. \tag{3.61}$$

Finally, the coefficient A^α is given by

$$A^\alpha\left(\frac{\mu}{k_B T_e}\right) = \frac{4}{3}\frac{F_3}{(1+e^{-\mu/k_B T_e})(F_{1/2})^2}. \tag{3.62}$$

While the Lee-More resistivity has a more rigorous derivation, it also has many terms which are difficult to evaluate computationally. Hence, a reduced form of the equations is used for simulations in this thesis. A discussion of the approximations used is present in Section 5.5, along with a comparison to the Spitzer resistivity.

3.4.3 Ohmic heating

Electron currents traversing resistive materials will undergo power dissipation and deposit energy into the material (Ohmic heating). This proceeds through collisions and momentum transfer between the current electrons and background ions. The mean force per unit volume from ion impact is $\boldsymbol{P}_{ei}$ given by the resistivity definition (3.52), and the mean speed of electrons is $\boldsymbol{v} = \boldsymbol{J}/n_e e$. Hence, the power due to Ohmic heating, P_Ω within some small volume, $d^3\boldsymbol{x}$ is

$$P_\Omega = \eta_r \boldsymbol{J}\cdot\boldsymbol{J} d^3\boldsymbol{x} \tag{3.63}$$

as power is the scalar product of force and velocity [78].

The temperature increase of the material due to this heating power can be deduced from the heat capacity of the material. Bell [100] approximates this heat capacity by applying an analytic fit to numerical solutions of the Thomas-Fermi equations of state [101],

$$C = \frac{d\epsilon}{k_B dT_e} = 0.3 + 0.8\left(\mathrm{DUT3} + 1.5T'\frac{2.2+T'}{(1.1+T')^2}\right) \tag{3.64}$$

$$\mathrm{DUT3} = \frac{(10^{-18}V'^{-0.75} + \ln(10^{22}V'))(2.906\times10^8 T'^{-2.0733333} - 7.223\times10^6 T'^{-0.853333})}{(3.283\times10^7 T'^{0.146666} + 1.805\times10^8 T'^{-1.073333})^{2.5}} \tag{3.65}$$

which corresponds to the temperature rise of a single electron after receiving energy $d\epsilon$. These equations use reduced variables, where $T' = k_B T_e Z^{-4/3}/e$, and $V' = 10^6 ZV$, where V is the volume occupied by a single atom.

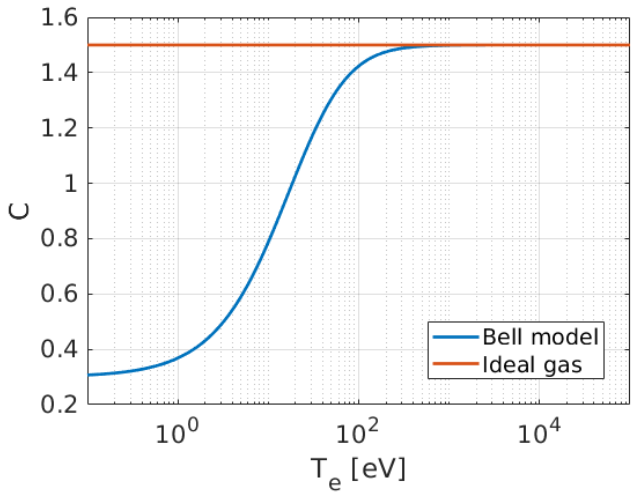

Figure 3.5: A comparison of the Bell model heat capacity [100] for Al, to that of a monatomic ideal gas.

The DUT3 term is often dropped when considering high-temperature solid-density systems. For an Al target at about 100 eV (1.2×10^6 K) electron temperature, we have $V' \approx 2 \times 10^{-22}$, and $T' \approx 3.3$ which returns DUT3 $\approx 2 \times 10^{-13}$. The second term in the brackets of (3.64) works out to about 1.4, and so the DUT3 term may be ignored. This yields the simple heat capacity at constant volume

$$C = 0.3 + 1.2T' \frac{2.2 + T'}{(1.1 + T')^2} \tag{3.66}$$

which has been plotted in Figure 3.5 for an Al target, and is compared to the equivalent C for a monatomic ideal gas.

Over a small time Δt in volume $d^3\boldsymbol{x}$, the energy transferred to the electrons is $P_\Omega dt$. If the energy is split evenly between the electrons in this volume, each one will receive an energy $V_e/d^3\boldsymbol{x}$, where the volume taken up by an electron V_e is approximately $1/n_e$. Hence, the temperature gain due to Ohmic heating can be written

$$\Delta T_e = \frac{\mathbf{j} \cdot \mathbf{j} \eta_r \Delta t}{n_e C k_B}. \tag{3.67}$$

3.4.4 Ionisation energy loss

As hot electrons pass through solids, they can lose energy to inelastic collisions with bound atomic electrons, which can result in ionisation. This background ionisation acts as an energy

loss mechanism for hot electrons, and can be parametrised by the mean excitation energy I_{ex} of the background solid (typically around $11Z$ eV, where Z is the solid atomic number) [102].

The nature of ionisation energy loss depends on the energies of the ionised background electrons. The electron emerging from the collision with the higher energy is considered the incident electron, and whichever is lower is termed a δ-ray, regardless of their state before the collision. This is due to the indistinguishable nature of electrons, and restricts the δ-ray kinetic energy, ϵ_k^δ to half that of the original incident electron. The cross sections corresponding to the energy transfer to bound electrons are derived using quantum scatter theory in the Born approximation [103]. Provided the δ-rays are below some critical energy, $\epsilon_{k,cut}$, the energy loss on the incident electron may be considered continuous, with a stopping power [102, 104]

$$\left.\frac{d\epsilon}{dx}\right|_{\epsilon_k^\delta<\epsilon_{k,cut}} = \frac{Zn_ie^4}{8\pi\epsilon_0^2 m_e v^2}\left(\ln\left(\frac{2(\gamma+1)m_e^2c^4}{I_{ex}^2}\right) + F^-(\tau,\tau_{up}) - \delta\right) \tag{3.68}$$

where v is the incident electron speed and δ is a density correction factor. The factor $F^-(\tau,\tau_{up})$ takes the form

$$F^-(\tau,\tau_{up}) = -1 - \left(\frac{v}{c}\right)^2 + \ln\left((\tau-\tau_{up})\tau_{up}\right) + \frac{\tau}{\tau-\tau_{up}} + \frac{1}{\gamma^2}\left(\frac{\tau_{up}^2}{2} + (2\tau+1)\ln\left(1-\frac{\tau_{up}}{\tau}\right)\right) \tag{3.69}$$

with additional parameters

$$\tau = \gamma - 1 \tag{3.70}$$

$$\tau_{up} = \min\left(\frac{\epsilon_{k,cut}}{m_ec^2}, \frac{\tau}{2}\right). \tag{3.71}$$

The density effect describes the reduction of the ionisation energy loss due to dielectric properties of the background material, as any polarisation may affect the electric fields from the hot electron [105]. Sternheimer [106] provides an analytic fit to the experimental density effect in a variety of targets, which can be described using a parameter x,

$$x = \frac{\ln(\gamma^2-1)}{4.606} \tag{3.72}$$

giving a density effect of the form

$$\delta(x) = \begin{cases} 0 & x < x_0 \\ 4.606x - C + a(x_1 - x)^3 & x_0 < x < x_1 \\ 4.606x - C & x > x_1 \end{cases} \tag{3.73}$$

with the additional parameters having values

$$C = 1 + 2\ln\left(\frac{I_{ex}}{\hbar}\sqrt{\frac{\epsilon_0 m_e}{Z n_i e^2}}\right) \tag{3.74}$$

$$a = 4.606\left(\frac{C}{4.606} - x_0\right)/(x_1 - x_0)^3 \tag{3.75}$$

$$(x_0, x_1) = \begin{cases} (0.2, 2) & I_{ex} < 100eV,\ C \leq 3.681 \\ (0.326C - 1, 2) & I_{ex} < 100eV,\ C > 3.681 \\ (0.2, 3) & I_{ex} \geq 100eV,\ C \leq 5.215 \\ (0.326C - 1.5, 3) & I_{ex} \geq 100eV,\ C > 5.215 \end{cases} \tag{3.76}$$

when considering condensed matter targets like solids.

In the continuous energy loss regime, the δ-rays lack the energy to move far from their atom and energy is deposited locally. As in Section 3.4.3, the energy deposition corresponds to a rise in solid temperature. Assuming the hot electron energy loss is shared equally between electrons in a local small volume $d^3\boldsymbol{x}$ on the hot electron trajectory, the background electron temperature gain is

$$\Delta T_e = \frac{\Sigma_h \Delta\epsilon_h}{Z n_i d^3\boldsymbol{x} C k_B} \tag{3.77}$$

where we sum the energy losses of each hot electron $\Delta\epsilon_h$, within this volume.

3.4.5 Møller scatter

Møller scatter and ionisation energy loss describe the same process - both consider hot electron energy loss to the ionisation of background atoms and ions. The distinction is in the energy of these ionised electrons (δ-rays). The model in Section 3.4.4 describes the creation of low-energy δ-rays, where the hot electron energy loss per ionisation is so small

and frequent that it may be treated as a drag force, with stopping power (3.68). Conversely, Møller scatter describes the discrete process of high energy δ-ray emission, with kinetic energy exceeding some value $\epsilon_{k,cut}$. Møller scatter provides a source of secondary hot electrons, and so the choice of $\epsilon_{k,cut}$ will depend on the minimum kinetic energy considered "hot" for the system of interest. Such events are infrequent, and provide large energy loss and scatter for the incident hot electron, and so a continuous stopping power is inappropriate here. Instead, a δ-ray emission cross section is considered for δ-ray energies exceeding $\epsilon_{k,cut}$.

The differential cross section per atom with respect to the energy transfer fraction $\epsilon = \epsilon_k^\delta / E_k$ is calculated from QED collisional theory [107], and is of the form

$$\frac{d\sigma}{d\epsilon} = \frac{Z}{8\pi\epsilon_0^2} \frac{e^4}{m_e v^2 E_k} \left(\frac{(\gamma-1)^2}{\gamma^2} + \frac{1}{\epsilon}\left(\frac{1}{\epsilon} - \frac{2\gamma-1}{\gamma^2}\right) + \frac{1}{1-\epsilon}\left(\frac{1}{1-\epsilon} - \frac{2\gamma-1}{\gamma^2}\right)\right) \tag{3.78}$$

where E_k, v and γ are the kinetic energy, speed and Lorentz factor of the incident electron before the collision. The total cross section per atom, σ_{atom} for creating a δ-ray with energy over $\epsilon_{k,cut}$ is found through integration of (3.78), which yields

$$\sigma_{atom} = \frac{e^4}{8\pi m_e \epsilon_0^2} \frac{Z}{v^2 \epsilon_k} \left(\frac{(\gamma-1)^2}{\gamma^2}\left(\frac{1}{2} - y\right) + \frac{1}{y} - \frac{1}{1-y} - \frac{2\gamma-1}{\gamma^2} \ln\left(\frac{1-y}{y}\right)\right) \tag{3.79}$$

where the parameter y represents $\epsilon_{k,cut}/E_k$ [104, 107, 108].

3.4.6 Thermal equilibration

The electrons in the background solid can exchange energy amongst themselves and the background ion population through collisions. This restores thermal equilibrium between the electron and ion species over some equilibration time-scale, which may be estimated from simple collisional analysis [36, 78]. If we work in the distant scattering limit, the ion can be assumed to be immobile, and the force on the electron is so weak that any deviation to its trajectory is small. A collision event in this set-up is shown diagrammatically in Figure 3.6. In this limit, integration of the electron-ion force over all time yields the change in momentum

$$\Delta p_\perp = \frac{Ze^2}{2\pi\epsilon_0 v_e b} \tag{3.80}$$

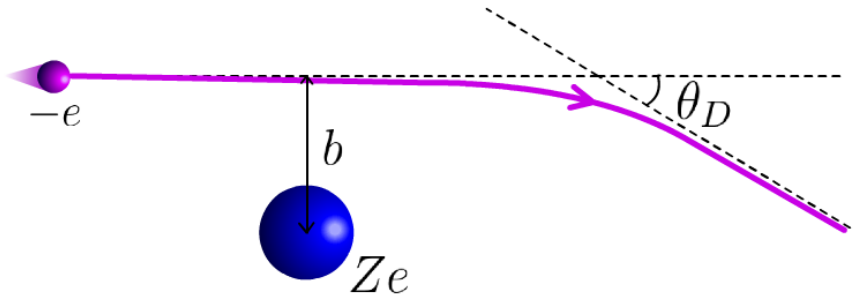

Figure 3.6: A schematic diagram showing a Coulomb collision between a hot electron and an ion.

where Ze is the ion charge, v_e the initial electron speed, and b is the distance of closest approach between the electron and ion in the absence of forces. This momentum change is perpendicular to the initial momentum direction of the electron, which results in a scatter angle

$$\theta_D \approx \frac{b_0}{b} \tag{3.81}$$

where the constant b_0 is defined to be

$$b_0 = \frac{Ze^2}{2\pi\epsilon_0 p_e v_e} \tag{3.82}$$

for initial electron momentum p_e. Small angle scattering occurs for $\theta_D \ll 1$, and so this approximation is useful for $b \gg b_0$.

The energy transfer in Coulomb collisions can be deduced from $\Delta p_\perp$ (3.80). This momentum must be gained by the ion to conserve momentum, and the corresponding rise in ion kinetic energy must be lost by the electron to conserve energy. This results in the energy transfer

$$\Delta E = \frac{m_e}{m_i}\frac{b_0^2}{b^2}\left(\frac{1}{2}m_e v_e^2\right) \tag{3.83}$$

for each collision.

In order to deduce the thermal equilibration rate between two particle species, we must

consider detailed calculations where both species are permitted to move, and have Maxwell-Boltzmann energy distributions. Performing these calculations yields the Spitzer expressions for thermal equilibration

$$\frac{dT_1}{dt} = \frac{T_2 - T_1}{t_{eq}} \tag{3.84}$$

$$\frac{1}{t_{eq}} = \frac{2}{3(2\pi k_B)^{3/2}} \frac{q_1^2 q_2^2 n_2 \sqrt{m_1 m_2} \ln \Lambda}{\epsilon_0^2 (T_1 m_2 + T_2 m_1)^{3/2}} \tag{3.85}$$

where we consider the rate of temperature change in species 1 through collisions with species 2 [78]. Here, the charge, mass, temperature and number density of species k are written as q_k, m_k, T_k and n_k respectively.

3.4.7 Elastic scatter

As hot electrons traverse the target, their trajectories will deviate due to elastic collisions with the background atoms and ions. In Section 3.4.6, equation (3.81) is derived to give the deflection angle from a single electron-ion collision in the limit of large impact parameters. However, it is impractical and unnecessary to calculate the angular deflection from each electron-ion pair. Instead we may calculate $\langle \Delta\theta^2(t) \rangle$, which describes the mean change in the squared deflection θ^2 by time t. Thus,

$$\Delta\theta^2(t) = \left(\sum_j^N \Delta\theta_j \right)^2 \tag{3.86}$$

which describes the sum of angular scatters $\Delta\theta$ from all collisions which occurred by time t. When squaring this sum, cross terms $\langle \Delta\theta_j \Delta\theta_k \rangle$ vanish, as each collision may be considered independent and $\langle \Delta\theta_j \rangle = 0$ in an isotropic plasma. Hence, (3.86) reduces to a sum of $\langle \Delta\theta_j^2 \rangle$, which may be expressed as

$$\langle \Delta\theta^2(t) \rangle = \int_{b_{min}}^{b_{max}} n_i (2\pi b db v_e t) \left(\frac{b_0}{b} \right)^2 \tag{3.87}$$

using (3.81) to express $\Delta\theta^2$ in terms of b and b_0. Here a volume is constructed, combining the area between impact parameters b and $b + db$ with the distance moved by the electron over time t, and the number of collisions is estimated to be the number of ions in this volume. This is integrated over the range of impact parameters corresponding to the small angle

scatter regime, resulting in

$$\langle \Delta\theta^2(t) \rangle = 2\pi n_i v_e t b_0^2 \ln\left(\frac{b_{max}}{b_{min}}\right) \tag{3.88}$$

where the Coulomb logarithm $\ln(b_{max}/b_{min})$ is often written as $\ln\Lambda$. To evaluate these terms in laser-solid systems, Davies chooses to use the atomic screening length for b_{max}, and also uses $b_{min} = \hbar/p$ motivated by the uncertainty principle [109, 110]. This yields an approximate value for $\langle \Delta\theta^2(t) \rangle$ of the form

$$\langle \Delta\theta^2 \rangle = \frac{Z^2 e^4 n_i}{2\pi\epsilon_0^2} \frac{\gamma m_e}{p^3} t \ln\left(\frac{4\epsilon_0 h}{Z^{1/3} m_e e^2} p\right) \tag{3.89}$$

for an electron of momentum p.

3.4.8 Collective electron transport phenomena

When considering the complex physics of hot electron transport in solid-density targets, a range of collective behaviours and instabilities can emerge which may affect the beam profile. These are discussed thoroughly in a review by Robinson *et al* [111], and are briefly summarised here.

From Ohm's law (3.53), it can be shown that the magnetic fields within the solid-density target evolve according to

$$\frac{\partial \boldsymbol{B}}{\partial t} = \eta_r \nabla \times \boldsymbol{j}_h + \nabla\eta_r \times \boldsymbol{j}_h + \frac{\eta_r}{\mu_0}\nabla^2 \boldsymbol{B} - \nabla\eta_r \times (\nabla \times \boldsymbol{B}) \tag{3.90}$$

using methods discussed in Section 5.4, where $\boldsymbol{j}_h$ denotes the hot electron current density. While the latter two terms in (3.90) describe magnetic diffusion and advection, the first two terms describe the generation of resistive magnetic fields.

Here, $\eta_r \nabla \times \boldsymbol{j}_f$ causes the magnetic field to grow in such a way that the fast electron beam is pinched, limiting divergence. The beam may also be hollowed by the $\nabla\eta_r \times \boldsymbol{j}_f$ term, as heating is concentrated in the beam centre where the electron density is the highest. This sets up a resistivity gradient in the transverse direction, which leads to electron expulsion from the beam centre. The resultant electron beam has a greater charge density around the edges than the centre. In this way, the resistive magnetic fields influence the profile of the hot electron beam.

The beam profile can be further modified through instabilities. Beam filamentation can arise due to anisotropies between the counter-propagating hot electrons and cool return currents. The resultant instability has the effect of fragmenting the beam, breaking it into smaller sub-structures [112]. It is expected that beam pinching, hollowing and filamentation will be present in the simulations performed in this thesis.

Chapter 4

EPOCH

4.1 The particle-in-cell method

EPOCH, the Extendible Particle-in-cell (PIC) Open Collaboration (with a silent 'H') is a code used to simulate plasmas with an international user-base [113, 114]. Numerical simulation of plasma physics typically falls into two categories: fluid codes (MHD) and kinetic codes (Vlasov, PIC). Hybrid codes also exist which combine aspects of these two code types [115]. In fluid codes, macroscopic quantities like density, velocity and temperature are calculated on a grid, and evolve according to fluid equations (conservation of mass, momentum, energy) where an equation of state is used to close the equations [80]. However, such a treatment is inappropriate when considering deviations from Maxwellian distributions, and so fluid codes cannot be used to describe phenomena like hot electron acceleration in short pulse lasers.

In kinetic models, the properties of individual particles are retained, and evolution occurs according to the plasma kinetic equation (3.10). Vlasov codes attempt to solve this directly, but as the phase-space density is a 6 dimensional quantity, these codes are often very computationally expensive to run. In some cases, phenomena may be suitably described without simulating all six dimensions [116–118], but even these Vlasov simulations can be time consuming.

Particle-in-cell codes divide the plasma phase space into macro-particles which represent many real particles, providing a light-weight simulation tool for a kinetic plasma treatment. These particles experience forces due to the electric and magnetic fields which are evaluated on a spatial grid, and interpolated to the particle position. The foundation of this methodology arose around the 1960's, where various authors showed that small systems of

a few thousand particles can accurately reproduce collective plasma behaviour [119–121]. As computer power increased, so too did the complexity of PIC codes, moving from simple collisionless plasmas on 1D spatial grids, to modern multidimensional codes like `EPOCH` with additional modules for collisions, photon generation and pair production.

This chapter will discuss the basic `EPOCH` framework, including certain physics modules and limitations of the code. Here we aim to support Chapter 5 which details our work on creating a hybrid extension for `EPOCH` to model laser-solid simulations. We acknowledge that the `EPOCH` code existed before this Ph.D. project and was not written by us; however, we did write the bremsstrahlung module discussed in Section 4.5.2, as `EPOCH` had no bremsstrahlung capability at the start of this project.

4.2 Particles

It should be unsurprising that Particle-In-Cell codes describe the passage of particles through cells. Each computational macro-particle represents many particles of the same particle species, such that all macro-particles combined approximate the phase-space density of the entire plasma. Macro-particles are described by their position, x^n and momentum, p^n at the current time-step n, along with their charge, mass and the number of real particles they represent (the macro-particle weight).

The code proceeds in discrete time-steps, updating physical quantities in a loop according to Figure 4.1. For particle variables, we are concerned with the three steps iterating $\boldsymbol{x}$ and $\boldsymbol{p}$, which are achieved using the particle velocity and the Lorentz force

$$\boldsymbol{x}^{n+1/2} = \boldsymbol{x}^n + \frac{\Delta t}{2}\frac{\boldsymbol{p}^n}{\gamma^n m} \tag{4.1}$$

$$\boldsymbol{p}^{n+1} = \boldsymbol{p}^n + q\Delta t\left(\boldsymbol{E}^{n+1/2} + \frac{1}{\gamma^{n+1/2}m}\boldsymbol{p}^{n+1/2} \times \boldsymbol{B}^{n+1/2}\right) \tag{4.2}$$

$$\boldsymbol{x}^{n+1} = \boldsymbol{x}^{n+1/2} + \frac{\Delta t}{2}\frac{\boldsymbol{p}^{n+1}}{\gamma^{n+1}m} \tag{4.3}$$

for a particle of mass m and charge q, where Δt is the time separation between time-steps n and $n+1$. The particle velocity is represented as $p/\gamma m$, where the Lorentz factor γ can be calculated from $\gamma = \sqrt{1 + (p/mc)^2}$. This is referred to as a leap-frog scheme, as $\boldsymbol{p}^n \to \boldsymbol{p}^{n+1}$ uses $\boldsymbol{x}^{n+1/2}$, and $\boldsymbol{x}^{n+1/2} \to \boldsymbol{x}^{n+3/2}$ uses $\boldsymbol{p}^{n+1}$. Both updates "hop over" each other, and quantities may only be evaluated at the same time if two half-steps are performed as in (4.1)

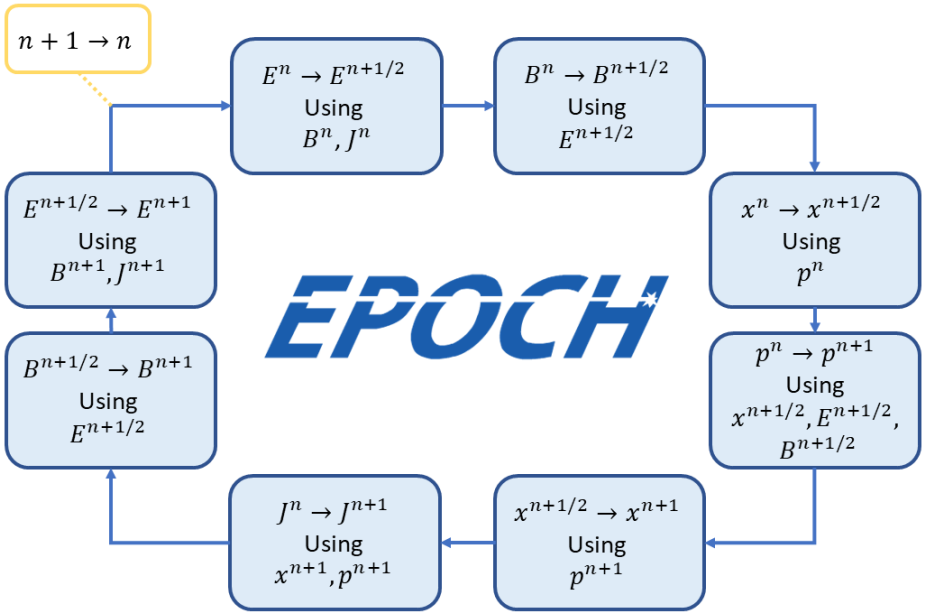

Figure 4.1: An illustration of the EPOCH PIC loop, detailing the order in which physical quantities are advanced, along with the terms used to perform each step. Initially, the position, $\boldsymbol{x}$, momentum $\boldsymbol{p}$, electric field, $\boldsymbol{E}$, magnetic field, $\boldsymbol{B}$, and current density, $\boldsymbol{J}$ are all evaluated at time-step n, and all end the loop at $n+1$. The point at which we switch notation from $n+1$ to n is labelled, and represents the start of the next loop.

and (4.3) [115].

Equation (4.2) requires the electric and magnetic fields acting on the particle, and so these grid quantities must be interpolated to the particle position. However, assigning the fields of the local cell to the particle position can produce noisy data as particles experience sudden field changes when passing from cell to cell. It is often better to average the fields over a few nearby cells, which is equivalent to assuming the macro-particle is distributed over some finite volume.

In EPOCH, the standard macro-particle distribution has a triangular shape $S(w)$, such that

$$S(w) = \begin{cases} 1 - |x_i - w|/dx & |x_i - w| < dx \\ 0 & \text{otherwise} \end{cases} \tag{4.4}$$

where x_i is the central particle position, the evaluation point is measured as some distance w from x_i, and dx is the spacing of grid points. The fraction of the macro-particle weight distribution over a given cell is found through integration of this shape over the cell boundaries,

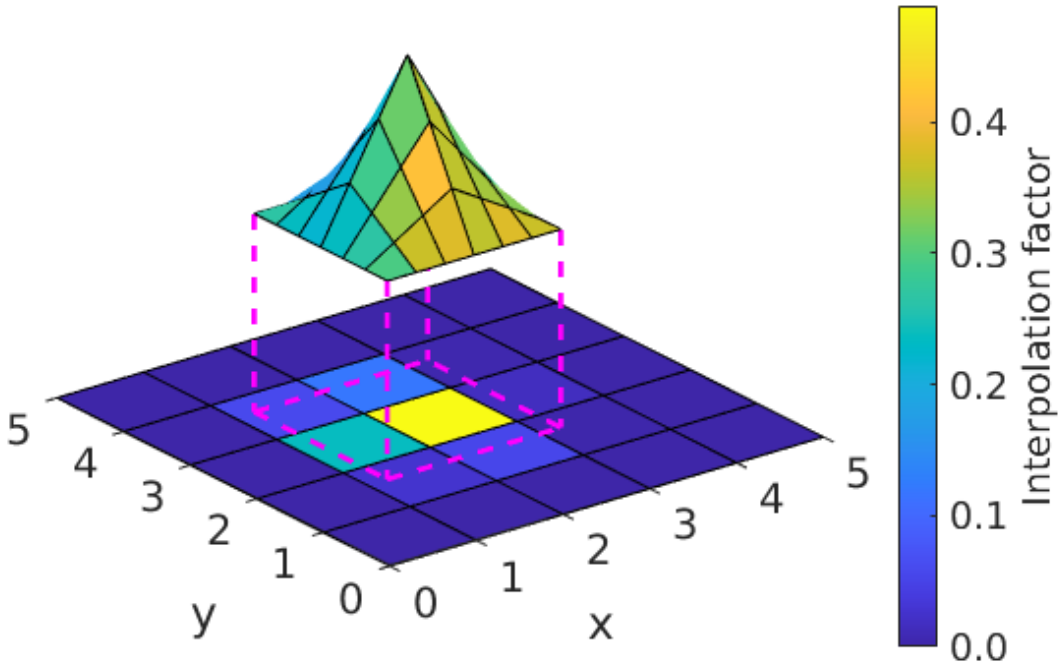

Figure 4.2: A diagram showing the contribution of each cell to the fields interpolated at the particle position in a 2D PIC simulation (see colour-bar). Interpolation fractions here represent those for variables which are evaluated at the cell centres. The corresponding particle is displayed above the cell grid, with a side-lit colour-map and coarse mesh to better show the 2-dimensional triangular weighting.

and so an interpolated field F may be written

$$F = \frac{1}{2}\left(\frac{1}{2} + \frac{X_j - x_i}{dx}\right)^2 F_{j-1} + \left(\frac{3}{4} - \frac{(X_j - x_i)^2}{dx^2}\right) F_j + \frac{1}{2}\left(\frac{1}{2} - \frac{X_j - x_i}{dx}\right)^2 F_{j+1} \qquad (4.5)$$

where X_j and F_j refer to the central position and field in cell j, assuming the field is evaluated in the cell centre. Contributions to the interpolated field can also be seen from the neighbouring cells F_{j-1} and F_{j+1}. In higher dimensions, $S(w)$ is calculated independently in each spatial direction, and the product of these 1D weights yields the full particle weight distribution. A 2D particle shape is shown in Figure 4.2, along with the multiplication factor applied to the fields in each cell when interpolating fields to the particle. Once the fields at the particle position are known, the momentum can be updated using the Boris algorithm [115, 122].

4.2.1 Boris particle pusher

The Boris particle pusher can advance the momentum vector forwards by a full time-step, according to (4.2) [115, 122]. The algorithm begins by defining two new vectors, $\boldsymbol{p}^+$ and $\boldsymbol{p}^-$, such that

$$\boldsymbol{p}^{n+1} = \boldsymbol{p}^+ + \frac{1}{2} q \boldsymbol{E}^{n+1/2} \Delta t \tag{4.6}$$

$$\boldsymbol{p}^{n} = \boldsymbol{p}^- - \frac{1}{2} q \boldsymbol{E}^{n+1/2} \Delta t \tag{4.7}$$

where $\boldsymbol{p}^+$ and $\boldsymbol{p}^-$ describe the momentum after applying half a time-step of $\boldsymbol{E}$ field acceleration to $\boldsymbol{p}^n$. Substitution of (4.6) and (4.7) into the momentum update (4.2) yields

$$\boldsymbol{p}^+ = \boldsymbol{p}^- + \frac{q\Delta t}{2m\gamma^{n+1/2}} \left(\boldsymbol{p}^+ + \boldsymbol{p}^-\right) \times \boldsymbol{B}^{n+1/2} \tag{4.8}$$

which shows $\boldsymbol{p}^+$ is simply a rotation of $\boldsymbol{p}^-$, where $|\boldsymbol{p}^+| = |\boldsymbol{p}^-|$. The components of $\boldsymbol{p}^+$ and $\boldsymbol{p}^-$ perpendicular to the magnetic field are sketched in Figure 4.3, where θ describes the rotation angle between these components. As $|\boldsymbol{p}^-|$ is the momentum after a half-acceleration, its magnitude is equivalent to $\boldsymbol{p}^{n+1/2}$, so $\gamma^{n+1/2} = \sqrt{1 + \boldsymbol{p}^- \cdot \boldsymbol{p}^- / mc}$.

We may evaluate the angle θ by noting that $\boldsymbol{p}^+$ and $\boldsymbol{p}^-$ may be replaced with $\boldsymbol{p}_\perp^+$ and $\boldsymbol{p}_\perp^-$ in (4.8), as any component parallel to the magnetic field has no contribution in the vector product. From the geometry of Figure 4.3, we write

$$\tan\left(\frac{\theta}{2}\right) = \frac{|\boldsymbol{p}_\perp^+ - \boldsymbol{p}_\perp^-|}{|\boldsymbol{p}_\perp^+ + \boldsymbol{p}_\perp^-|} = -\frac{qB^{n+1/2}}{2\gamma^{n+1/2}m} \Delta t \tag{4.9}$$

where the second equality comes from (4.8) using $\boldsymbol{p}_\perp^+$ and $\boldsymbol{p}_\perp^-$.

To proceed, two new vectors are defined

$$\boldsymbol{p}' = \boldsymbol{p}^- + \boldsymbol{p}^- \times \boldsymbol{t}_\theta \tag{4.10}$$

where $\boldsymbol{t}_\theta$ is chosen to make $\boldsymbol{p}'$ perpendicular to $(\boldsymbol{p}^+ - \boldsymbol{p}^-)$, as shown in Figure 4.3. This is satisfied for

$$\boldsymbol{t}_\theta = \frac{q\Delta t}{2m\gamma^{n+1/2}} \boldsymbol{B}^{n+1/2} \tag{4.11}$$

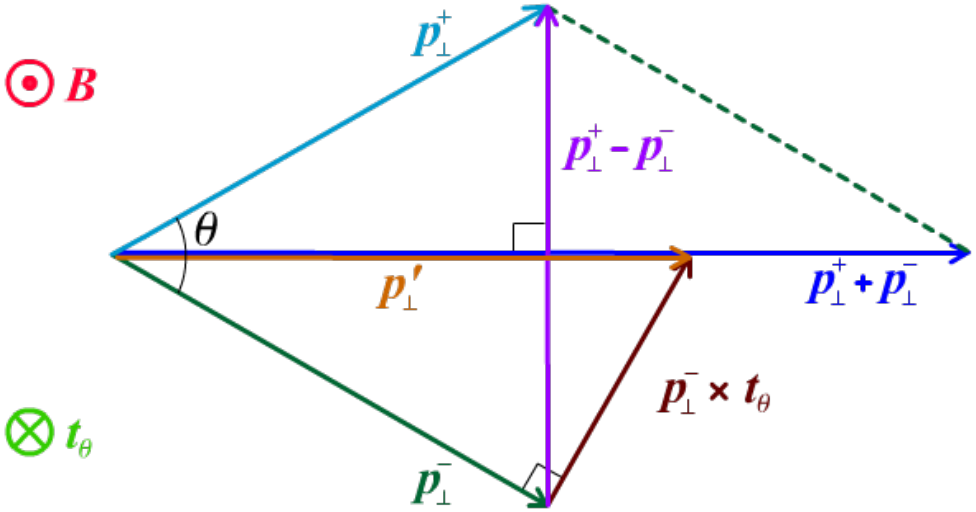

Figure 4.3: A depiction of important vectors and angles used in the particle pusher algorithm described by Boris [115,122]. Here the $\perp$ sub-script refers to vector components in the plane perpendicular to the magnetic field. Diagram is sketched for a negatively charged particle.

and $\boldsymbol{p}' \times \boldsymbol{t}_\theta$ returns a vector which is parallel to $(\boldsymbol{p}^+ - \boldsymbol{p}^-)$. Utilising the constraint $|\boldsymbol{p}^+| = |\boldsymbol{p}^-|$ results in the relationship

$$\boldsymbol{p}^+ = \frac{2}{1+t_\theta^2}(\boldsymbol{p}' \times \boldsymbol{t}_\theta) + \boldsymbol{p}^- \tag{4.12}$$

and so the momentum may be updated using equations (4.6)-(4.12).

4.3 Field solver

The EPOCH fields are evolved in time using discretised forms of the Faraday-Lenz (2.3) and the Ampère-Maxwell (2.4) equations. The four field updates present in Figure 4.1 are

$$\boldsymbol{E}^{n+1/2} = \boldsymbol{E}^n + \frac{1}{2}c^2\Delta t\left(\nabla \times \boldsymbol{B}^n - \mu_0 \boldsymbol{J}^n\right) \tag{4.13}$$

$$\boldsymbol{B}^{n+1/2} = \boldsymbol{B}^n + \frac{1}{2}\Delta t\left(\nabla \times \boldsymbol{E}^{n+1/2}\right) \tag{4.14}$$

$$\boldsymbol{B}^{n+1} = \boldsymbol{B}^{n+1/2} + \frac{1}{2}\Delta t\left(\nabla \times \boldsymbol{E}^{n+1/2}\right) \tag{4.15}$$

$$\boldsymbol{E}^{n+1} = \boldsymbol{E}^{n+1/2} + \frac{1}{2}c^2\Delta t\left(\nabla \times \boldsymbol{B}^{n+1} - \mu_0 \boldsymbol{J}^{n+1}\right) \tag{4.16}$$

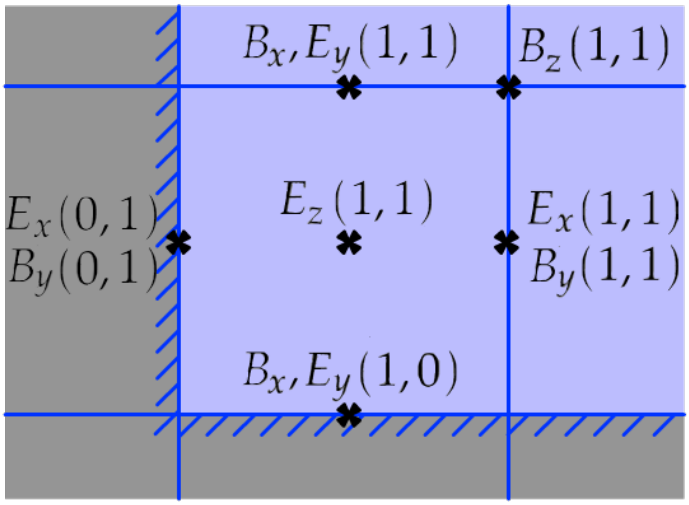

Figure 4.4: Visualisation of field staggering in an `EPOCH2D` simulation. Here we show how the fields are arranged on the $x_{\min}$, $y_{\min}$ simulation window corner, and fields are labelled by their cell indices. The greyed out cells denote ghost cells, starting at index 0.

which represent two full steps in $\boldsymbol{E}$ and $\boldsymbol{B}$, split into half-steps such that fields may be evaluated at the same time for the particle push.

As equations (4.13)-(4.16) rely on the curl of the fields, the code must find a way to discretise these operations too. If field variables F were evaluated in the centre of their cells, then the partial spatial derivative $\partial F/\partial x$ evaluated in cell i could be written as

$$\left.\frac{\partial F}{\partial x}\right|_i = \frac{F_{i+1} - F_{i-1}}{2\Delta x} \tag{4.17}$$

for a cell size Δx. Such schemes may develop instabilities as the gradient in cell i does not depend on the field in its own cell. This allows the grid to decouple into two cell groups according to an even-odd ("chequerboard") pattern, which can lead to non-physical numerical oscillations. Such issues are addressed by off-setting the field evaluation points using a Yee staggered grid [123], which has been drawn in Figure 4.4 for a 2D cell. It can be seen that this stagger allows calculation of gradients using only one neighbour. For example, $E_z(i,j)$ depends on the gradient $\partial B_y/\partial x$ evaluated at the centre of cell (i,j), which is given by

$$\left.\frac{\partial B_y}{\partial x}\right|_{i,j} = \frac{B_y(i,j) - B_y(i-1,j)}{\Delta x} \tag{4.18}$$

as can be seen in Figure 4.4.

Ghost cells must be positioned around the simulation boundary as particle shapes centred within the simulation may still reach outside. The treatment of fields associated with these ghost cells can determine the boundary conditions of the system. Ghost cell fields can form the mirror image of the adjacent simulation cells (reflective boundaries), a mirror image with field-signs then flipped in the ghost cells (open boundary conditions, fields are clamped to 0 on the simulation edges), or ghost cells can match the simulation cells on the opposite boundary (periodic boundaries). Similarly, particles passing these simulation edges either have a momentum component flipped (reflective), are removed from the simulation (open), or are re-injected into the opposite boundary (periodic). Lasers pulses may be injected through boundaries by ensuring the fields of the ghost cells satisfy the wave equation.

4.4 Currents

The final component to be addressed in the basic PIC loop shown in Figure 4.1 is the algorithm which updates the current density, which is a term used by the field solver (4.13) and (4.16). The general form for current density calculation is given by Villasenor and Buneman [124], where it is shown how the motion of a single particle can trigger current flow across several boundaries. This can also be seen in Figure 4.2, where a moving macro-particle would trigger a flow of current across all cell edges contained within the particle shape.

The specific current density calculation used by `EPOCH` is the Esirkepov current density decomposition scheme [125]. Here, the particle positions $x^{n+3/2}$ are calculated by advancing x^{n+1} forwards by half a timestep using the momentum at p^{n+1}. The total integrated macro-particle weight in each cell before and after the update are compared, and currents can be deduced. The full current density J^{n+1} is found from summing current contributions from all macro-particles in the simulation.

4.5 Radiation

The `EPOCH` code is sometimes referred to as a QED-PIC code, as it contains physics packages beyond the conventional PIC loop shown in Figure 4.1. Radiation is achieved by allowing macro-particles to emit secondary macro-particles (photons), according to a Monte Carlo algorithm [47,114,126]. Monte Carlo sampling allows the stochastic nature of photon emission

to be captured, and its implementation is discussed in the remainder of this section.

Let λ describe the rate of secondary particle emission, such that λdt describes the probability of an emission during some small time dt. The probability of no emission by time $t = Ndt$ would then be

$$P(L) = \lim_{N\to\infty} (1 - \lambda t/N)^N \tag{4.19}$$

$$\approx e^{-\tau} \tag{4.20}$$

where we can define the optical depth, τ as

$$\tau = \int_0^t \lambda(t')dt'. \tag{4.21}$$

Hence, the cumulative distribution function for photon emission by time t, $F(t)$ is

$$F(t) = 1 - e^{-\tau}. \tag{4.22}$$

An optical depth for emission, τ_e can be sampled for each macro-electron by rearranging (4.22) to $\tau = -\ln(1 - F(t))$, and replacing $F(t)$ with a uniformly distributed random number between 0 and 1. In each time-step, the optical depth travelled by each electron is saved, and an emission event is triggered when the total optical depth travelled exceeds τ_e. In emission, a new macro-particle is added to the simulation at the emitting macro-electron position, with a momentum drawn from a relevant distribution for the emission process and a weight matching the emitting macro-electron. Hence, X-ray photons are treated as particles in the code, and are distinct from the low frequency electromagnetic radiation tracked by the field solver (see Section 4.3). Once the secondary particle is created, the emitting macro-electron has its momentum reduced to conserve momentum, then its saved optical depth is reset and a new τ_e is sampled for the next emission.

The calculation of the optical depth depends on the emission mechanism. For processes described with an emission rate, the optical depth update in a given step is found from integrating this rate over the step interval as in (4.21). For emissions described by a cross section σ, we replace the idea of "emissions per unit time" with "emissions per unit length", and consider the step-length instead of the time-step. By the definition of σ, the probability of emission for a macro-electron taking a step of length dL, is $n_a\sigma_a dL$, where σ_a is the cross-

section per particle of species a, and n_a is the number density of that species at the macro-electron position. In cross section based systems, the τ_e sampling and emission behaves the same, but in each step the particle τ value evolves according to

$$\Delta\tau = \sum_a n_a \sigma_a v \Delta t \tag{4.23}$$

for a particle moving at speed v. Here the sum refers to a sum over all background species which can contribute to the emission process, and different species may have different cross sections.

4.5.1 Synchrotron

At the start of this project, the only X-ray generation module present in `EPOCH` was for synchrotron radiation [47, 114], as discussed in Section 2.4. These emissions are described by a rate of photon production, and so the synchrotron optical depth evolves according to (4.21).

In updating the optical depth travelled by a specific particle, the `EPOCH` algorithm first computes η by interpolating the local fields over the macro-particle shape, and using the η definition (2.52). It is assumed the rate is constant over a simulation time-step Δt, and so the change in synchrotron optical depth $\Delta\tau$ is

$$\Delta\tau = \frac{\Delta t \eta \alpha \sqrt{3} m_e c^2 h_s(\eta)}{2\pi h \gamma} \tag{4.24}$$

which comes from the synchrotron photon production rate (2.69). In `EPOCH`, the values of $h_s(\eta) = \int_0^{\eta/2} d\chi F(\eta,\chi)/\chi$ are logarithmically interpolated from a pre-calculated table *hsokolov.table* which contains η values from 10^{-5} to 10 [126]. A sample of this table is shown in Table 4.1.

The energy of the emitted photon is sampled using a cumulative density function, $\xi(\chi)$ of the double differential, $d^2N_\gamma/d\chi dt$ (2.66), where

$$\xi(\chi) = \frac{\int_{\chi_{\min}}^{\chi} (d^2N_\gamma/d\chi' dt) d\chi'}{\int_{\chi_{\min}}^{\eta/2} (d^2N_\gamma/d\chi' dt) d\chi'} \tag{4.25}$$

and we recall from Section 2.4.2 that the maximum χ for a given η is $\eta/2$. Here, the η parameter characterises the hot electron energy in the current field configuration (2.52), and

$\log_{10}(\eta)$	$\log_{10}(h_s(\eta))$
-5	0.7189960759048358
-4.987975951903808	0.7189959234513367
-4.975951903807616	0.7189957678439705
⋮	⋮
1	0.3459150912836859

Table 4.1: A sample of tabulated $\log_{10}(h_s(\eta))$ values, as present in the file *hsokolov.table* in the `EPOCH` source code. There are 500 data pairs in total.

χ describes the energy of the emitted photon in the background fields (2.67). The χ values between 0 and $\chi_{\min}$ are neglected for computational efficiency, and $\chi_{\min}$ is chosen such that the neglected low-energy photons account for only 10^{-9} of the total emitted energy. Values of $\chi_{\min}$ have been pre-calculated for each tabulated η, and are stored in the table *chimin.table*. By replacing $\xi(\chi)$ with a random number sampled from a uniform distribution between 0 and 1, we may re-arrange (4.25) to sample an emission χ. This corresponds to a photon energy

$$E_\gamma = \frac{2\chi}{\eta} E_e \tag{4.26}$$

where E_e is the electron total energy, and we have assumed the electron is ultra-relativistic such that the photon is emitted in the electron momentum direction.

To sample this in `EPOCH`, the code generates a 2D array with 100 rows corresponding to logarithmically spaced η values from 10^{-5} to 10, where each row contains 100 logarithmically spaced χ values between $\chi_{\min}$ and $\eta/2$. The code also loads ξ values from the file *ksi_sokolov.table*, which is another 100×100 array such that each element in the table corresponds to the ξ value for the (η, χ) pair in the generated array. Interpolation proceeds with η first (from particle), creating a list of 100 χ values from the generated array and 100 ξ values from the file, with χ being taken from interpolation of ξ (from random sample).

4.5.2 Bremsstrahlung

While `EPOCH` was already capable of synchrotron emission at the start of this Ph.D. project, there was no bremsstrahlung module present in the code. This section details the work that was undertaken as part of this Ph.D. to create the bremsstrahlung capability. We were not the first group to write bremsstrahlung modules for PIC codes - various groups had already

$\eta = 10^{-5}$		$\eta = 10$	
$\log_{10}(\chi)$	ξ	$\log_{10}(\chi)$	ξ
-17.30	0.004993870735451265	-6.30	0.005472539720644287
-17.18	0.0054807618431451655	-6.23	0.005777738754227076
-17.06	0.006015122525404382	-6.16	0.0060999584181248
	⋮		⋮
-5.30	1	0.70	1

Table 4.2: A sample of values used in assigning synchrotron photon energies. These show the first three and final generated $\log_{10}(\chi)$ values and their corresponding ξ for two different η. In the code, there are an additional 98 logarithmically spaced η values between these limits, and each η has 100 (χ, ξ) pairs.

implemented some form of bremsstrahlung radiation [28, 30, 31, 127–130], using different models to describe the cross section of this interaction. Pandit [31] used a classical form of the bremsstrahlung cross section [33], equivalent to our (2.29). While this approach can approximate the quantum result [41], it neglects the effect of screening. This is accounted for by other groups [28, 30, 127] who use the Seltzer-Berger bremsstrahlung cross sections [38], which are covered in Section 2.2.3. However, as discussed by Wu *et al* [128], the Seltzer-Berger cross sections come from models describing the screening effects due electrons orbiting atoms, whereas particle in cell simulations are mostly concerned with ions in plasma.

Wu *et al* [128] describe an approximate differential bremsstrahlung cross section for partially ionised targets. By combining the $d\chi/d\omega$ values for atomic targets (2.32) and fully ionised targets (2.35), a general $d\chi/d\omega$ may be written

$$\frac{d\chi}{d\omega} = \frac{e^2}{12\pi^3\epsilon_0^3 c}\left(\frac{e^2}{m_e c^2}\right)^2 Q^2 \left(\frac{Z^2}{Q^2}\ln\left|\frac{a m_e v}{\hbar}\right| + \ln\left|\frac{\lambda_D}{a}\right|\right). \tag{4.27}$$

which is parametrised by the ion charge Q (in units of e). For neutral atoms ($Q = 0$), this returns the atomic screened case, and the plasma case is returned for fully ionised materials ($Q = Z$). A simple interpolation between these limits is performed by (4.27) to estimate the differential radiation cross section for partially ionised materials. Wu *et al* report that for a significantly heated target, the bremsstrahlung cross section could be 2-3 times higher than that predicted by models which don't include these screening corrections [128]. It should be noted that the form presented in Wu *et al* is slightly different to our (4.27), as they quote the stopping power $dE/dx = n_i\chi$ in the relativistic approximation where $v = c$.

Equation (4.27) provides a good cross section approximation, but it is derived from

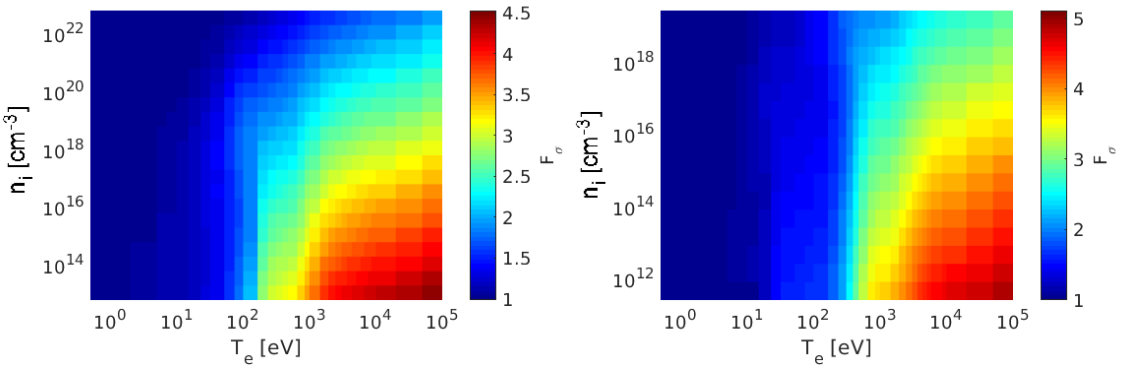

(a) Aluminium (b) Argon

Figure 4.5: Values of the cross section enhancement factor F_σ for plasma screening, as described in equation (4.28). The average charge state for a given temperature was found using `FLYCHK` data. For reference, aluminium at solid density has $n_i = 6.02 \times 10^{22}$ cm^{-3}, and argon at standard pressure and temperature has $n_i = 2.56 \times 10^{19}$ cm^{-3}.

classical theory which is only valid in the complete screening limit (electron energies $> 192Z^{-1/3}m_e c^2$, about 42 MeV in Al) [33]. The limitations of classical modelling are shown in Section 6.1.4, where equation (4.27) is benchmarked against an equivalent set-up using the quantum Seltzer-Berger cross sections. Instead, the theory of Wu *et al* can be used to derive a cross section multiplication factor F_σ, where

$$F_\sigma = \frac{d\chi(Q)/d\omega}{d\chi(Q=0)/d\omega} = 1 + \frac{Q^2}{Z^2}\frac{\ln(\lambda_D/a)}{\ln(am_e v/h)} \tag{4.28}$$

and this factor can be applied to the quantum differential cross sections of Seltzer and Berger [38, 39]. Figure 4.5 shows how this cross section enhancement varies with electron number density, n_e and electron temperature in two different targets (Al and Ar). Information on the average ionisation state Q for a given temperature and density was obtained using `FLYCHK` [37], and ion number density was found from $n_e = Qn_i$.

Unlike the synchrotron process, bremsstrahlung radiation uses an emission cross-section and so its optical depth evolves according to (4.23). Hence each time-step, the ion number density in each cell must be computed and interpolated to each macro-electron position for calculation of n_i, and the cross section must be known for each macro-electron kinetic energy ϵ_k. The tabulated Seltzer-Berger cross sections list $(v/Zc)^2 E_\gamma d\sigma/dE_\gamma$ in millibarns [38, 39], and so pre-processing must be performed to obtain σ. The form of the original tables is shown in Table 4.3.

$\ln(\epsilon_k/(1\text{ MeV}))$	E_γ/ϵ_k			
	10^{-12}	0.025	$\cdots$	1
-6.9078	7.85327	7.84905	$\cdots$	4.35999
-6.5023	7.25292	7.03983	$\cdots$	3.75610
$\vdots$	$\vdots$	$\vdots$		$\vdots$
9.2103	36.8182	35.4044	$\cdots$	0.04685

Table 4.3: Sample of the raw data from one of the Seltzer-Berger tables ($Z = 1$). For each pair of electron kinetic energy and photon energy, (ϵ_k, E_γ), the tables quote $(v/Zc)^2 E_\gamma d\sigma/dE_\gamma$ in millibarns where v is the electron speed. Tables exist for $Z = 1$ to 100.

Interpolation of the Seltzer-Berger tables mirror the treatment performed in Section 4.5.1, where η is replaced with ϵ_k, and E_γ plays a similar role to χ. For each atomic number Z, a new set of tables is constructed with parameters more useful to `EPOCH` simulations. The total cross section at each tabulated electron energy is calculated from

$$\sigma = \int_{E_{\gamma,\text{cut}}}^{\gamma m_e c^2} \frac{d\sigma}{dE_\gamma} dE_\gamma \tag{4.29}$$

where $E_{\gamma,\text{cut}}$ is defined such the energy radiated by photons with $0 < E_\gamma < E_{\gamma,\text{cut}}$ accounts for the fraction 10^{-9} of the full radiated energy

$$\int_0^{E_{\gamma,\text{cut}}} E_\gamma \frac{d\sigma}{dE_\gamma} dE_\gamma = 10^{-9} \int_0^{\gamma m_e c^2} E_\gamma \frac{d\sigma}{dE_\gamma}. \tag{4.30}$$

The use of $E_{\gamma,\text{cut}}$ is essential because $d\sigma/dE_\gamma \to \infty$ as $E_\gamma \to 0$, and the factor 10^{-9} was chosen to be consistent with the synchrotron cut-off already present in the code. Enhancements to σ due to F_σ (4.28) are calculated after the cross section has been sampled. A 2D table is then constructed to hold a line of E_γ sample points for each ϵ_k, where photon energies range from $E_{\gamma,\text{cut}}$ to ϵ_k. The cumulative density function, $\xi(E_\gamma)$ is calculated for each (ϵ_k, E_γ) pair using

$$\xi(E_\gamma) = \frac{1}{\sigma} \int_{E_{\gamma,\text{cut}}}^{E_\gamma} \frac{d\sigma}{dE'_\gamma} dE'_\gamma \tag{4.31}$$

which is used to calculate emitted photon energies in the same way as in the synchrotron algorithm.

In order to correctly describe the angular distribution of bremsstrahlung radiation from electrons which aren't ultra-relativistic, we must consider the scatter produced in the emis-

sion process itself. We have opted to use an algorithm documented in the `Geant4` Physics Reference Manual [104], which samples the emission angle using a fit to the Tsai differential cross section (DCS) [131, 132].

By using an approximate form of the full Tsai DCS, the polar angle θ is obtained using the following reject/accept algorithm:

$$b = \begin{cases} 0.625 & r_1 < 0.25 \\ 1.875 & r_1 \geq 0.25 \end{cases} \tag{4.32}$$

$$u = -\frac{\ln(r_2 r_3)}{b} \tag{4.33}$$

where r_1, r_2 and r_3 are uniformly distributed random numbers between 0 and 1. If $u \leq \gamma\pi$ where γ is the electron Lorentz factor, then the polar angle $\theta = u/\gamma$. Otherwise we generate three new random numbers and calculate a new u value, and repeat until we have $u \leq \gamma\pi$. The azimuthal angle, ϕ is assigned the value $\phi = 2\pi r_4$, where r_4 is also a random number taken from a uniform distribution between 0 and 1.

4.6 Limitations

PIC codes are useful as they provide a general code framework for calculating kinetic effects in a variety of problems. Despite this, some limitations can still arise when using these codes. While typically more versatile than Vlasov codes, PIC simulations can still be considered computationally expensive when compared to fluid codes - particularly when simulating cold dense plasmas. These computational demands impact the length and time-scales which can be simulated by PIC, and laser-solid simulations are typically restricted to 2D simulations over times on the order of 1 ps, with simulation windows only spanning tens of microns in each direction.

Performance can be enhanced through fine-tuning of the simulation parameters, although at low resolutions the code can suffer from problems such as self-heating. The specifics of these points are dealt with in the following sections.

4.6.1 Convergence parameters

If computational expense was no issue, each real particle could be represented by its own macro-particle. In this ideal world, the cell size and time intervals between steps could both be made small enough to achieve arbitrary spatial and temporal resolution in the simulation. In the real world, this would never work - computational limitations restrict the number of cells and time-steps available to us. By simulating larger time-steps for fewer macro-particles in larger cells, a computer can simulate larger volumes over longer times. However, as we relax the simulation parameters, the code will start to lose the ability to resolve fine details which can start to affect the results. In convergence testing, we seek a set of computational parameters such that further increases in resolution no longer produce any significant difference in our results.

The first parameter to consider is cell size. In a simulation window of fixed size, a larger cell size allows the system to be modelled with fewer cells. However, laser-solid simulations are often set-up with a vacuum layer between the simulation edge and the target to allow expansion - the laser must propagate through space in order to reach the solid. This propagation proceeds through Maxwell's equations, but this can only work if the laser wavelength is well resolved, otherwise the electro-magnetic fields would be too noisy to return a wave equation solution. As the typical wavelengths of interest are ~ 1 µm, an upper limit on cell size would be placed ~ 100 nm, although this scale-length may fail to resolve the plasma fully and self-heating may further restrict the cell size, as discussed in Section 4.6.2.

The most computationally expensive process in `EPOCH` is the particle-pusher, which updates the position and momentum of all particles in each step. Hence reducing the number of macro-particles per cell is a good way to speed up the code, but this can lead to less resolved currents and fewer macro-electrons result in fewer macro-photon emission events. Due to the Monte Carlo emission algorithm, many emitting macro-electrons lead to less statistical noise in bremsstrahlung energy/angular spectra, but there are other ways to achieve the same effect. By artificially increasing the bremsstrahlung cross section by some amount and reducing the macro-photon weight by the same amount, we can sample more bremsstrahlung emissions and retain the same total photon count/energy.

Finally we may consider the time-step. An upper limit on the `EPOCH` time-step is placed by the Courant-Friedrichs-Lewy (CFL) condition [133] for the stability of explicit numerical integrators. The CFL condition requires that the *numerical* information propagation speed

must be greater than the *physical* speed information can travel at. When updating the electro-magnetic fields of the cells, each update relies on a neighbouring cell and so field information can travel at a rate of one cell-length Δx per time-step Δt. In `EPOCH`, the physical speed limit of information propagation is set by c, so the CFL condition implies

$$\Delta t < \frac{\Delta x}{c} \tag{4.34}$$

for a 1D code. Further restrictions on the time-scale must be applied to ensure that macro-electrons do not emit multiple secondary particles for a given process per time-step, as the implementation restricts emission to one secondary per process per macro-electron [113].

4.6.2 Self-heating

The Debye length provides an appropriate length-scale for measuring plasma effects, but in a cold, solid density plasma this is often significantly smaller than the region of interest, and cannot be resolved by any reasonable cell size. However, large cells and time-steps can give rise to non-physical stochastic fields as macro-particles move around, which have the effect of heating the plasma [134, 135]. This self-heating is often unavoidable in laser-solid simulations, and sets an upper limit on how long the simulation results can be trusted. Self-heating is especially problematic when modelling radiation, as energy gained by electrons can be radiated away producing false X-ray signals. It is difficult to impose a "correct cell size", and simulation parameters are chosen to minimise the uncertainties caused by self-heating.

The rate of self-heating has been characterised by Arber *et al* in `EPOCH` simulations with a plasma of electron density $n_e = 1.11 \times 10^{29}$ m^{-3} [113]. An order of magnitude estimate for this rate in simulations with cell size, Δx and particles per cell, N_{ppc} was found to be

$$\frac{\partial T}{\partial t} \approx 3.2 \times 10^{-14} \alpha_H \frac{e}{k_B} \frac{n_e^{3/2} \Delta x^2}{N_{\text{ppc}}} \tag{4.35}$$

where $\alpha_H = 300$ for the default `EPOCH` settings, and all parameters are evaluated in SI units. As shown in (4.35), the effects of self heating can be reduced by decreasing the cell size or increasing the number of particles per cell. Additional improvements may be achieved by considering higher-order macro-particle shapes, which span over more cells than those shown in Section 4.2 and reduce α_H to 20 [113]. However, as these larger particle shapes are distributed over more cells, interpolation of cell fields to the particle position becomes more

computationally expensive - especially in 2D and 3D simulations. EPOCH also comes with current-smoothing capabilities, in which currents are averaged over surrounding cells [136]. This has the effect of reducing the stochastic error fields which arise in low resolution codes, resulting in lower α_H values of 60 and 2 for the default and higher-order particle shapes respectively.

Thus, self-heating can be reduced with smaller cells, more macro-particles, larger macro-particle shapes and current smoothing, although all of these reduce the performance of the code and ultimately limit the run-time and simulation size. In running PIC simulations of laser-solid interactions, one must balance the damaging effects of self-heating against the performance hit from each of these improvements. In order to run large, long time-scale laser-solid simulations in 3D, we must reduce the PIC algorithm into something more computationally efficient. This leads us to our hybrid-PIC extension for EPOCH, which is the focus of Chapter 5.

Chapter 5

Hybrid code

5.1 Overview

Particle-in-cell (PIC) simulations offer a computationally feasible framework for studying the interaction of high intensity lasers with matter, and have seen widespread use in modelling laser-wakefield [137], laser-electron-beam [51], and laser-solid systems [28, 30, 128]. In order to model solid materials in PIC codes, the user must represent them as a cold, dense plasma, which requires a very high resolution spatial grid and many macro-particles per cell to suppress the effects of numerical self-heating. These computational demands place heavy restrictions on the size and time-scales of these systems, and most authors limit themselves to only 2D simulations.

Hybrid-PIC codes (also called electron transport codes) present an alternative way to model solids in the PIC framework, treating the solid as a background fluid. This offers a significant speed boost as we no longer have huge numbers of solid macro-particles to track, which opens the possibility for 3D simulations of laser-solid systems. Additional hybrid routines are added to PIC codes which describe how electron temperatures and currents in the solid evolve over time, which influence the electric and magnetic fields within the solid. The laser is replaced by a hot electron injector which roughly characterises the expected hot electron distribution from the laser pulse, and further hybrid routines describe the interaction of hot electrons with the solid by modifying their trajectories and energies.

Several groups have already developed hybrid-PIC codes to describe laser-solid physics, but existing hybrid codes like `ZEPHYROS` (RAL) [138] and `THOR` (AWE) [139] are designed for low energy electrons, and `LSP` (Northrop Grumman) [140] is a commercial code which isn't

open-source. As multi-petawatt lasers start to become readily available, hot electron energies could exceed 100 MeV in these targets, which would require high energy physics packages like bremsstrahlung radiation and Møller scatter to model their propagation accurately.

We have developed a hybrid extension [141] to `EPOCH`, which follows the traditional hybrid-PIC framework of codes like `ZEPHYROS`, with additional high-energy subroutines taken from `Geant4` [142–144]. The hybrid mode consists of two main changes to `EPOCH`, the first of which being the hybrid-PIC loop which includes additional hybrid processes and is shown in Figure 5.1. Hybrid geometries are specified in the code using a new solid data-type, which stores all the relevant solid parameters. New field variables track the resistivity, η_r (3.56), and background electron, T_e and ion, T_i temperatures in each cell.

As in the normal PIC loop, the field update is split into two halves, such that we have time-centred fields for leap-frogging the particle push. This allows us to use the same particle pusher as in the traditional PIC code, with additional momentum-changing scripts like elastic scatter and ionisation loss occurring separately. The loop starts and finishes with the time-variable evaluated half a time-step ahead of the particles and fields, and we output with fields evaluated half a time-step behind the particles for consistency with the normal PIC loop.

The increase in computational efficiency comes at the expense of failing to fully model certain aspects of the laser-solid interaction. The background density is non-evolving, so target deformation due to hole-boring and expansion cannot be modelled. This restricts the upper limit of laser intensity which may be reliably modelled, however, such deformation is expected to be small for our lasers of interest. Thermal conduction between cells has been ignored, which limits the accuracy of the resistivity calculation. This accuracy is further limited by the field-solver, which lacks some magnetic transport properties such as the Nernst effect [145]. However, such background treatment is expected to have a limited effect on the X-rays produced by short (40 fs) electron bunches, which quickly diverge to low current densities inside the target. The remainder of this chapter will describe the additions made to the code in this hybrid extension.

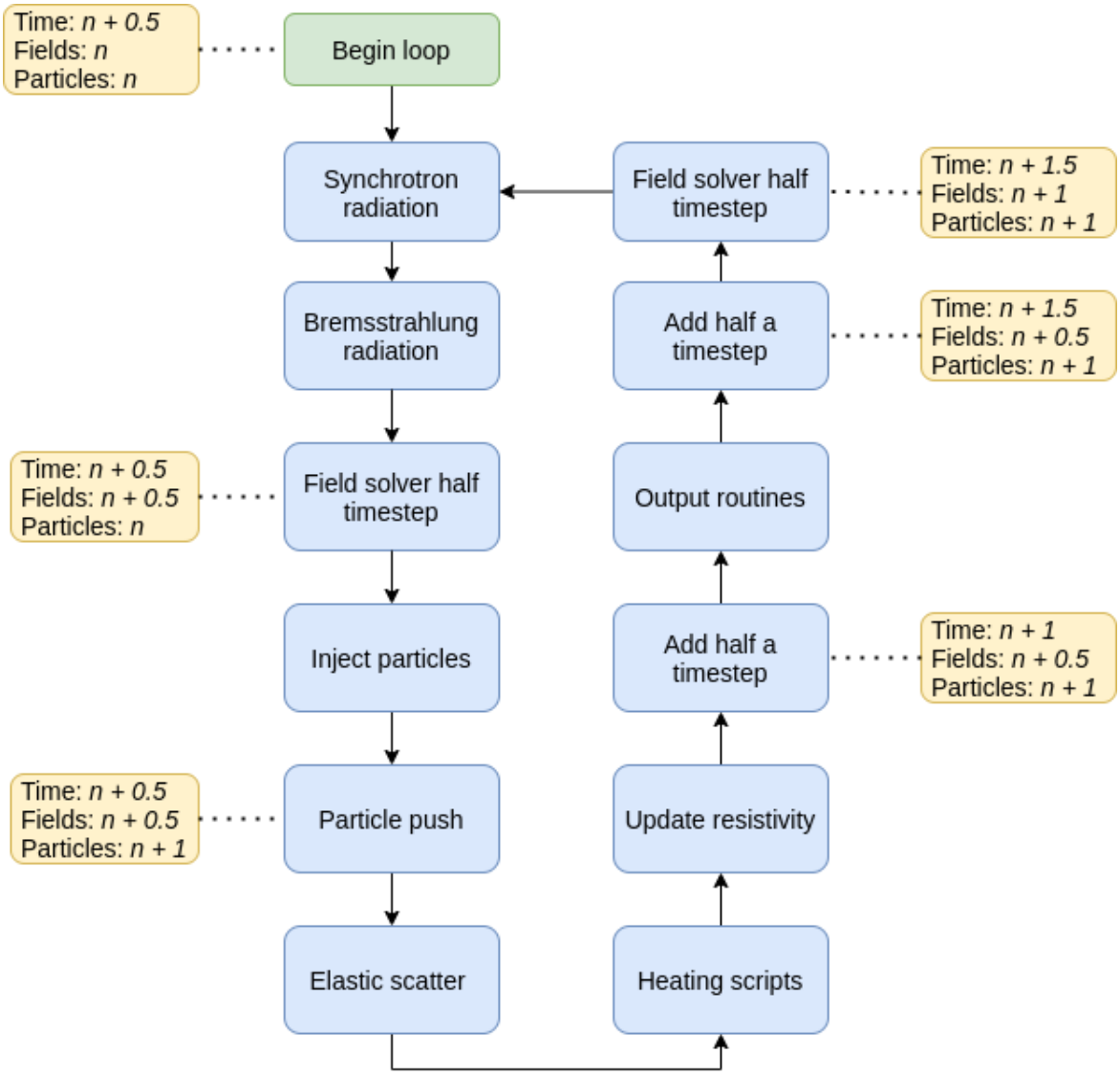

Figure 5.1: A flow chart which demonstrates the main subroutines called in a hybrid-PIC loop. For extra clarity, we also include the current timestep associated with the `EPOCH` time variable, the fields, and the particle positions. Ionisation loss, Ohmic heating, and thermal equilibration of electron and ion species all fall under the label of "heating scripts" in this figure.

5.2 Solids

To describe the solid materials which hot electrons interact with, we introduce a new "solid" concept to `EPOCH`. Solids are defined by an atomic number, Z, mean excitation energy, I_{ex}, and atomic mass number, A. For each solid that is introduced to the simulation window, three new field arrays are added to describe the heat capacity, C, and electron, n_e and ion, n_i number densities for the solid in each cell. By setting n_i to zero in some cells, complex targets of spatially separated materials may be defined. While individual solid types refer to a single elemental material, compound targets can be created by spatially overlapping solids. For example, plastic could be made by defining a carbon solid and a hydrogen solid in the same cells, with the ion densities of each solid summing to the ion density of the plastic as a whole.

The hybrid-PIC code described by Davies uses the heat capacity (3.66), and the heating equations of Ohmic (3.67) and collisional (3.77) heating [110]. When applying these equations to compound targets, Davies creates a single "average solid" in each cell, using a target-averaged atomic number (for example, $\langle Z \rangle \approx 2.7$ for plastic). While this works for the heating subroutines, this would lead to inaccuracies in the bremsstrahlung spectra as the bremsstrahlung cross section scales roughly with Z^2 as in (4.27). In bremsstrahlung radiation from electrons in plastic, the parameter $\langle Z^2 \rangle \approx 12.7$ is important, yet the target-averaged $\langle Z \rangle^2 \approx 7.1$ which demonstrates the limitation with an average-target approach. To fix this, we treat each solid independently and have extended the Davies heating model to consider the heating of multiple targets within a single PIC cell.

The heat capacity of each solid is worked out independently using (3.66), and these are combined in compound targets by defining an effective inverse heat capacity term, C_{eff}^{-1}

$$C_{\text{eff}}^{-1} = \sum_{\text{sol}} \left(\frac{Z^{\text{sol}} n_i^{\text{sol}}}{C^{\text{sol}}} \right) \tag{5.1}$$

where we sum over each solid (sol) present in a given cell. Here, Z^{sol}, n_i^{sol} and C^{sol} refer to the atomic number, ion number density and heat capacity of a solid respectively. This variable can be used to obtain the solid-averaged inverse heat capacity

$$\left\langle \frac{1}{C} \right\rangle_{\text{sol}} = \frac{C_{\text{eff}}^{-1}}{\sum_{\text{sol}} \left(Z^{\text{sol}} n_i^{\text{sol}} \right)} = \frac{C_{\text{eff}}^{-1}}{n_e^{\text{tot}}} \tag{5.2}$$

where we have written the total electron number density in the cell as n_e^{tot} for conciseness. Hence, the Ohmic and collisional heating equations for compound targets may be written as

$$\Delta T_e = \frac{\mathbf{j}\cdot\mathbf{j}\eta_r dt}{n_e^{\text{tot}} k_B}\left\langle\frac{1}{C}\right\rangle_{\text{sol}} \tag{5.3}$$

$$\Delta T_e = \frac{\Sigma_h \Delta\epsilon_h}{n_e^{\text{tot}} V_c k_B}\left\langle\frac{1}{C}\right\rangle_{\text{sol}} \tag{5.4}$$

using (3.67) and (3.77), where we have considered the cell volume V_c as our small volume $d^3\boldsymbol{x}$. While solids are treated independently, there is a global background electron/ion temperature present in each cell, and thermal equilibration subroutines allow background electrons to share thermal energy with the background ions. This is achieved using a discretised form of the thermal equilibration equations (3.84-3.85). Thus, if the time between steps n and $n+1$ is Δt, the temperature of species s at step $n+1$, T_s^{n+1} can be written

$$T_e^{n+1} = T_e^n + \Delta t \frac{2}{3(2\pi k_B)^{3/2}} \frac{(Z^*)^2 e^4 n_i \sqrt{m_e m_i}\ln\Lambda}{\epsilon_0^2 (T_e^n m_i + T_i^n m_e)^{3/2}}(T_i^n - T_e^n) \tag{5.5}$$

$$T_i^{n+1} = T_e^n + \Delta t \frac{2}{3(2\pi k_B)^{3/2}} \frac{(Z^*)^3 e^4 n_i \sqrt{m_e m_i}\ln\Lambda}{\epsilon_0^2 (T_e^n m_i + T_i^n m_e)^{3/2}}(T_e^n - T_i^n) \tag{5.6}$$

where s has been swapped for i and e to describe ions and electrons respectively. Here we have written the electron number density as $Z^* n_i$ for ion charge state Z^*, and $\ln\Lambda$ is the Coulomb logarithm (see Section 5.5 for calculation).

5.3 Electron injection

In general, the nature of hot electrons in a laser-solid interaction will depend on the pre-plasma density profile, laser intensity, and the temporal and spatial structure of the laser-pulse. Electron transport codes often approximate this distribution by considering a small number of easily customisable parameters, including an efficiency parameter $\eta_{l\to e}$ describing the fraction of laser energy absorbed by the electrons in the pre-plasma.

The mean energy of the electron distribution is approximately $a_0 m_e c^2$, as given by Wilks scaling (3.50). To determine how many electrons must be injected at a given point and time through a simulation boundary, $(\mathbf{r}, t)$, we have to characterise the spatial $f(\mathbf{r})$ and temporal $g(t)$ distributions of the laser respectively. If these represent fractions of the peak laser intensity I_0, then we have the laser intensity $I(\mathbf{r}, t) = I_0 f(\mathbf{r}) g(t)$. The laser energy passing

through a small area dA at position $\mathbf{r}$ over times t to $t+dt$ is $I(\mathbf{r},t)dAdt$, and if the fraction $\eta_{l\to e}$ is transferred to hot electrons of average kinetic energy $\langle\epsilon_k\rangle = a_0(\mathbf{r},t)m_ec^2$, then the number of electrons to inject, $N(\mathbf{r},t)$ is

$$N(\mathbf{r},t) = \frac{I_0 f(\mathbf{r})g(t)dAdt\eta_{l\to e}}{\langle\epsilon\rangle}, \tag{5.7}$$

where $a_0(\mathbf{r},t)$ is evaluated using $I(\mathbf{r},t)$, according to the pump strength definition (3.45).

Typically hot electrons follow an exponential energy distribution, and for a laser of normal incidence, we expect electrons to be injected into a cone with a peak angle described by Moore scaling (3.49) [93]. In the code, particle rotation routines have been developed to rotate an electron from its initial momentum direction through polar angle θ and azimuthal angle ϕ, and are described in Section 5.3.1.

5.3.1 Particle rotation

When particles undergo any kind of scatter, their trajectories are deflected by a polar angle θ relative to their initial direction. An azimuthal rotation about the polar axis, ϕ is also applied, sampled from a uniform distribution between 0 and 2π in all cases of rotation used in the code. To apply this rotation to an arbitrary momentum 3-vector, we find the direction cosines using the same geometric arguments as presented by Peplow [146]. The derivation of this method starts by noting that any vector in spherical polar coordinates can be written as

$$\boldsymbol{\Omega} = r\cos\theta\hat{\boldsymbol{z}} + r\sin\theta\cos\phi\hat{\boldsymbol{x}} + rsin\theta\sin\phi\hat{\boldsymbol{y}} \tag{5.8}$$

where $\hat{\boldsymbol{z}}$ is a unit vector in the polar direction, with $\hat{\boldsymbol{x}}$ and $\hat{\boldsymbol{y}}$ forming two additional unit vectors, such that all three are mutually perpendicular. As our rotations are relative to the initial momentum, $\boldsymbol{p}$, let us label the momentum direction unit vector such that

$$\frac{\boldsymbol{p}}{|\boldsymbol{p}|} = \begin{pmatrix} u \\ v \\ w \end{pmatrix} = \hat{\boldsymbol{z}}. \tag{5.9}$$

As shown by Peplow [146], we can form mutually perpendicular unit vectors $\hat{\boldsymbol{x}}$ and $\hat{\boldsymbol{y}}$ in terms of the momentum direction components

$$\hat{\boldsymbol{x}} = \frac{1}{\sqrt{1-w^2}} \begin{pmatrix} uw \\ vw \\ w^2-1 \end{pmatrix} \tag{5.10}$$

$$\hat{\boldsymbol{y}} = \frac{1}{\sqrt{1-w^2}} \begin{pmatrix} -v \\ u \\ 0 \end{pmatrix} \tag{5.11}$$

and so $\boldsymbol{p}'$, the momentum vector of a particle after rotation through a polar angle θ and an azimuthal angle ϕ, can be calculated using

$$\boldsymbol{p}' = |\boldsymbol{p}| \begin{pmatrix} u\cos\theta + \cos\phi\sin\theta\frac{uw}{\sqrt{1-w^2}} - \sin\phi\sin\theta\frac{v}{\sqrt{1-w^2}} \\ v\cos\theta + \cos\phi\sin\theta\frac{vw}{\sqrt{1-w^2}} + \sin\phi\sin\theta\frac{u}{\sqrt{1-w^2}} \\ w\cos\theta + \cos\phi\sin\theta\frac{w^2-1}{\sqrt{1-w^2}} \end{pmatrix}. \tag{5.12}$$

These equations become undefined at $w = \pm 1$, so in the case where the polar direction is on the z axis, we resort to the standard polar case and retain the sign of w

$$\boldsymbol{p}' = |\boldsymbol{p}| \begin{pmatrix} \sin\theta\cos\phi \\ \sin\theta\sin\phi \\ \frac{w}{|w|}\cos\theta \end{pmatrix}. \tag{5.13}$$

By using the fraction $w/|w|$ in the final component of (5.13), we can apply this rotation to w values which are very close to one in machine precision, and still generate a unit vector to prevent momentum loss.

5.4 Field solver

The hybrid field solver follows the method described by Davies *et al* [109, 110]. We assume the propagation of hot electrons is neutralised by a return current of background electrons,

which establishes an Ohmic electric field, $\mathbf{E}$ due to the resistivity, η_r of the solid

$$\mathbf{E} = \eta_r \mathbf{j}_b \tag{5.14}$$

where $\mathbf{j}_b$ is the current density of the background electrons. Assuming total current density $\mathbf{j}$ is the sum of $\mathbf{j}_b$ and the hot electron current density $\mathbf{j}_h$, the Ampère-Maxwell law can be written as

$$\mathbf{E} = \eta_r \left(\frac{1}{\mu_0} \nabla \times \mathbf{B} - \mathbf{j}_h \right) \tag{5.15}$$

where μ_0 is the permeability of free space. We have neglected the displacement current using the arguments of Davies *et al* [109], where they assert this is only important while the return current establishes itself. They calculate this time-scale to be of order $\epsilon_0 \eta_r$ (about 0.02 fs for aluminium targets), which is negligible over picosecond pulses. The magnetic field evolves according to the Faraday-Lenz law (2.3) as in regular PIC codes. Discretisation of the hybrid field equations (5.15) and (2.3) can be achieved in a similar way to the traditional PIC field solver. The step is performed in two half-steps, but with a simple first-order step for the electric field. In 3D, the update for the x-component of the magnetic field in a given cell, $B_x^{n+1/2}(i_x, i_y, i_z)$ reads:

$$\begin{aligned} B_x^{n+1/2}(i_x, i_y, i_z) = B_x^n(i_x, i_y, i_z) &- \frac{\Delta t}{2\Delta y} \left(E_z^n(i_x, i_y + 1, i_z) - E_z^n(i_x, i_y, i_z) \right) \\ &+ \frac{\Delta t}{2\Delta z} \left(E_y^n(i_x, i_y, i_z + 1) - E_y^n(i_x, i_y, i_z) \right) \end{aligned} \tag{5.16}$$

where Δt denotes the timestep, n denotes the time index, and Δy, Δz are the cell sizes in the y and z directions. The hybrid field solver is only a first order method, as the electric fields are simply recalculated at the B timestep after B has been updated, via

$$\begin{aligned} E_x^{n+1/2}(i_x, i_y, i_z) = \frac{1}{2} &\left(\eta_r(i_x + 1, i_y, i_z) + \eta_r(i_x, i_y, i_z) \right) \\ &\left[\frac{1}{\mu_0 \Delta y} \left(B_z^{n+1/2}(i_x, i_y + 1, i_z) - B_z^{n+1/2}(i_x, i_y, i_z) \right) \right. \\ &- \frac{1}{\mu_0 \Delta z} \left(B_y^{n+1/2}(i_x, i_y, i_z + 1) - B_y^{n+1/2}(i_x, i_y, i_z) \right) \\ &\left. - J_x(i_x, i_y, i_z) \right] \end{aligned} \tag{5.17}$$

where we note that the resistivity, η_r is a cell-centred variable, and the current density, $\mathbf{J}$ shares the same Yee stagger as the electric field [123]. The resistivity and current density in (5.17) are evaluated at different times relative to the B in the two half steps, and could be written as η_r^n, J_x^n for the update after *bremsstrahlung radiation*, and $\eta_r^{n+1/2}$, $J_x^{n+1/2}$ for the update before *synchrotron radiation* (see Figure 5.1).

We must also consider the boundary conditions of our new field solver. The distribution of field evaluation points on the staggered grid has been shown for a 2D grid in Figure 4.4. The field point $E_z(1,1)$ depends on the neighbouring values $B_y(1,1)$, $B_x(1,1)$, and also ghost cell field points $B_x(1,0)$ and $B_y(0,1)$. If these ghost cell points were set to match their closest simulation-cell counterparts, the gradient across $E_z(1,1)$ would always be zero, and no magnetic field could contribute to the electric field in this point. To correct for this, we update the fields in all cells from indices 0 to $nx+1$ (for x, where nx is the number of simulation cells). We then apply zero-curl boundary conditions to cells which are not directly involved in the calculation of simulation window fields. This boundary condition sets the values of ghost cells to match the first ghost cell, for example, $E_x(-1,1)$, $E_x(-2,1)$, ... $E_x(1-ng,1)$ would be set to $E_x(0,1)$, where ng is the number of ghost cells.

5.5 Reduced Lee-More resistivity model

The Lee-More resistivity model discussed in Section 3.4.2 provides a model for calculating the resistivity in heated solid-density targets. However, the full form involves calculation of polylogarithm functions for the Fermi-Dirac integrals, and calculation of the chemical potential, μ which also requires a Fermi-Dirac treatment. This results in a model which is computationally expensive - especially for a process which must be calculated in every cell for each time-step. Instead, we introduce a reduced Lee-More model as is present in the `ZEPHYROS` code [138], which avoids direct calculation of μ and varies between the high and low temperature limits of the full model. In the following discussion, several terms have been pre-defined in Section 3.4.2.

In the Lee-More resistivity (3.56), the only terms which depend on the chemical potential are the electron relaxation time τ (3.57), and the A^α factor (3.62). The original Lee-More

paper [98] quotes these terms in the non-degenerate plasma limit $\mu \to -\infty$,

$$A^{\alpha} \to \frac{32}{3\pi} \tag{5.18}$$

$$\tau \to \frac{12\pi^2\epsilon_0^2}{e^4}\sqrt{\frac{m_e}{2\pi}}\frac{(k_b T_e)^{3/2}}{(Z^*)^2 n_i \ln\Lambda} \tag{5.19}$$

which are the SI equivalents of the paper's (27 [98]) and (28a [98]) respectively, and the terms have the same meaning as in Section 3.4.2. The Lee-More paper also provides a low temperature relaxation time, τ_{cold} given by (3.59), with a corresponding A^{α} value of 1.

Our ZEPHYROS-style reduced Lee More model starts with an effective hot electron relaxation time, $\tau_{\text{hot}} = A^{\alpha}\tau$ evaluated in the non-degenerate limit. As the temperature falls, τ_{hot} becomes unphysically small and we switch to an effective cold relaxation time, τ_{cold}

$$\tau_{\text{cold}} = \lambda_1 \frac{R_0}{v_e} \tag{5.20}$$

which is the low temperature relaxation time (3.59) with an additional fitting parameter, λ_1. Our reduced Lee-More resistivity formula reads

$$\eta_r = \frac{m_e}{Z^* n_i e^2 \tau_{\text{eff}}}\lambda_2 \tag{5.21}$$

$$\tau_{\text{eff}} = \max(\tau_{\text{hot}}, \tau_{\text{cold}}) \tag{5.22}$$

where λ_2 is a second fitting parameter for scaling the total resistivity.

The ion charge state, Z^* can be calculated using a fit to the Thomas-Fermi ionisation states given by More [147] in their Table IV, reproduced in our Table 5.1 for completeness.

The equations used in calculating the Coulomb logarithm for (5.19) are presented in Section III.B of the Lee-More paper [98], and are summarised in SI units in here. The authors use a Coulomb logarithm of the form

$$\ln\Lambda = \max\left(\frac{1}{2}\ln\left(1 + \left(\frac{b_{\max}}{b_{\min}}\right)^2\right), 2\right) \tag{5.23}$$

where $b_{\max}$ and $b_{\min}$ denote the upper and lower cut-offs of the Coulomb interaction respectively. The upper limit, $b_{\max}$ is taken to be the largest of the ion sphere radius R_0 (3.60)

Algorithm
$T_0 = T_{e,eV} Z^{-4/3}$
$R = \rho_{g/cm^3}/A_Z Z$
$T_F = T_0/(1+T_0)$
$A = a_1 T_0^{a_2} + a_3 T_0^{a_4}$
$B = -\exp(b_0 + b_1 T_F + b_2 T_F^7)$
$C = c_1 T_F + c_2$
$Q_1 = AR^B$
$Q = (R^C + Q_1^C)^{1/C}$
$x = \alpha Q^\beta$
$Z^* = Zx/(1+x+\sqrt{1+2x})$

Parameters	
a_1	3.323×10^{-3}
a_2	0.9718
a_3	9.26148×10^{-5}
a_4	3.10165
b_0	-1.7630
b_1	1.43175
b_2	0.31546
c_1	-0.366667
c_2	0.983333
α	14.3139
β	0.6624

Table 5.1: Algorithm for determining the ionisation state of the solid background [147]. Here we have used the solid mass density (in g/cm^3), ρ_{g/cm^3}, with A_Z and Z representing the mass number and atomic number of the solid atoms respectively, and $T_{e,eV}$ denoting the background electron temperature in eV.

and the Debye-Hückel screening length λ_{DH}, such that

$$b_{\max} = \max(\lambda_{DH}, R_0) \tag{5.24}$$

where

$$\frac{1}{\lambda_{DH}^2} = \frac{Z^* e^2 n_i}{\epsilon_0} \left(\frac{1}{\sqrt{(k_B T_e)^2 + \epsilon_F^2}} + \frac{Z^*}{k_B T_i} \right) \tag{5.25}$$

and T_i is the temperature of the background ions. The Fermi energy, ϵ_F has the form

$$\epsilon_F = \frac{\hbar^2}{2m_e} \left(3\pi^2 Z^* n_i\right)^{2/3}. \tag{5.26}$$

The lower limit, $b_{\min}$ is taken to be the largest of the de Broglie wavelength, λ_{dB} and the classical distance of closest approach b_{impact}, where

$$b_{\text{impact}} = \frac{Z^* e^2}{4\pi\epsilon_0 m_e v_e^2} \tag{5.27}$$

$$\lambda_{dB} = \frac{h}{2m_e v_e} \tag{5.28}$$

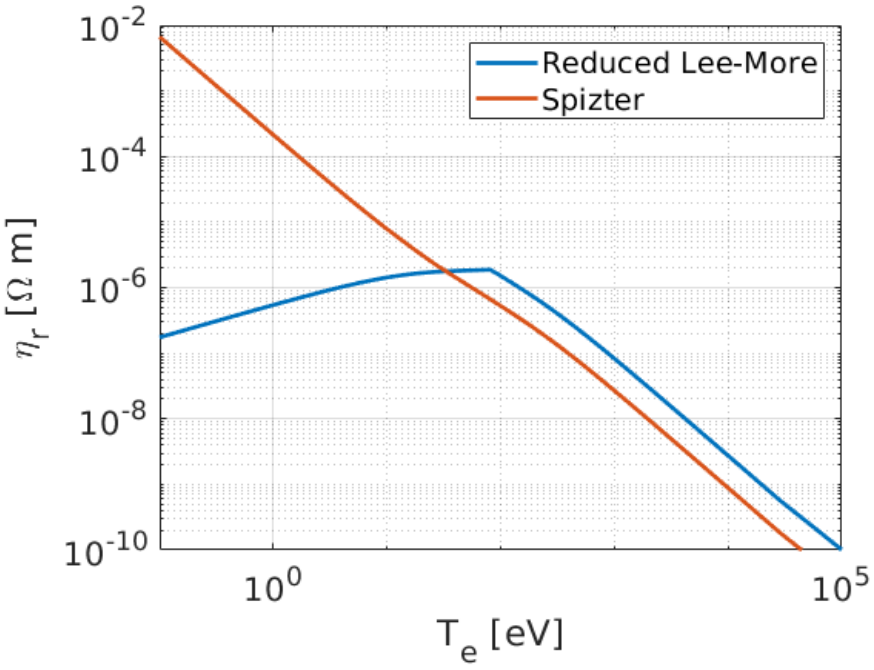

Figure 5.2: A comparison between the reduced Lee-More resistivity model in Section 5.5 and the Spitzer resistivity (3.55). The fitting parameters (λ_1, λ_2) have been set to (7, 3.5). The Z^* and $\ln\Lambda$ parameters in the Spitzer equation have been calculated in the same way as in the reduced Lee-More model.

and so

$$b_{\min} = \max(b_{\text{impact}}, \lambda_{dB}) \tag{5.29}$$

where we have evaluated the background electron velocity again using the mean thermal speed (3.61).

A comparison between this reduced Lee-More resistivity and the Spitzer resistivity (3.55) has been presented in Figure 5.2 for an Al target. Here, the model fit parameters λ_1 and λ_2 have been set to 7 and 3.5 respectively, following a fit to experimental data shown in Section 6.6. The drawback of this approach is that the model now over-estimates the Spitzer resistivity at high temperatures by a factor of λ_2. The sensitivity of resistive heating to these fitting parameters has been explored in Section 6.7.

5.6 Ionisation energy loss and Møller scatter

As discussed in Section 3.4.4, ionisation energy loss treatment can be split between a continuous energy loss due to the creation of low energy δ-rays, and discrete emission considering the recoil due to high energy δ-rays. Here, the term δ-ray is used to describe background electrons which are excited by incident hot electrons. The hybrid model treats ionisation energy loss and Møller scatter as two separate processes performed one after another. First the hot electron is slowed using a continuous stopping power, then the optical depth increase is calculated for the Møller scatter emission. In this way, ionisation energy loss and secondary hot electron production for all δ-ray energies is considered.

The continuous energy loss treatment calculates the density correction (3.73), then calculates the energy loss, $d\epsilon$ from the stopping power (3.68) and the step size. After applying this loss to the macro-electron, the $d\epsilon$ values are summed in each cell and are used for heating calculations.

Just as in bremsstrahlung and synchrotron emission, high energy δ-rays are emitted according to an optical depth model, with an emission mechanism characterised by a cross section and so their optical depth evolves according to (4.23). Here, σ refers to the cross section for high energy δ-ray emission (3.79), and the background species density, n_a is replaced with n_i, the background ion number density evaluated at the hot electron position.

Once a discrete Møller scatter event takes place, the δ-ray energy is sampled from the Møller scattering differential cross section using the following algorithm:

1. Generate two uniformly distributed random numbers between 0 and 1 (r_1 and r_2)

2. Draw a ξ using
$$\xi = \frac{\xi_0}{1 - (1 - 2\xi_0)r_1}$$

3. Calculate $g(\xi)$ using
$$g(\xi) = \frac{4}{9\gamma^2 - 10\gamma + 5}\left((\xi(\gamma - 1))^2 - (2\gamma^2 + 2\gamma - 1)\frac{\xi}{1 - \xi} + \frac{\gamma^2}{(1 - \xi)^2}\right)$$

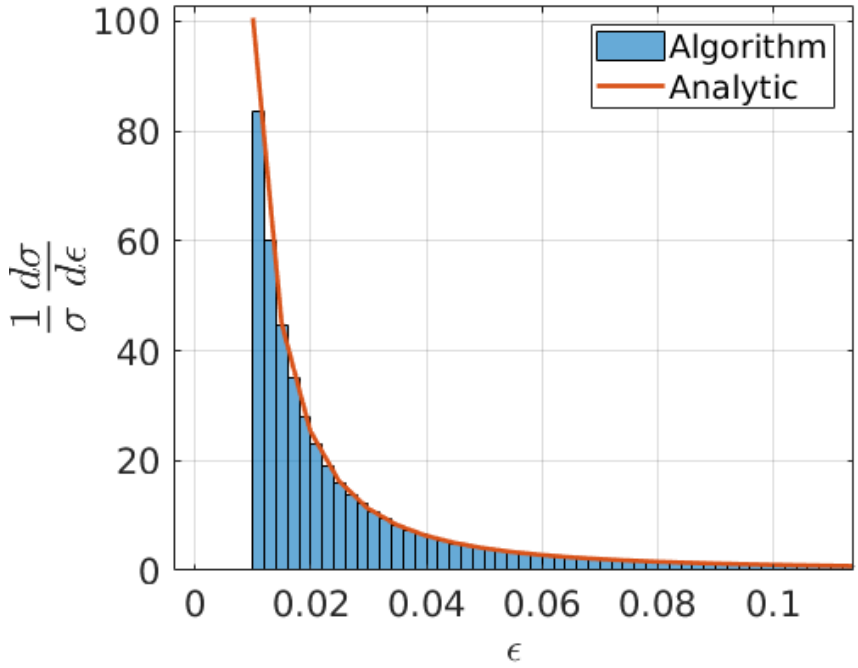

Figure 5.3: A comparison between the analytic differential cross section for Møller scatter, and that produced by employing the `Geant4` sampling algorithm. Here, $\epsilon = \epsilon_{\mathrm{k,cut}}/\epsilon_k$, for hot electrons with $\epsilon_k = 100$ MeV, $\epsilon_{\mathrm{k,\ cut}} = 1$ MeV in an Al target.

4. Reject or accept δ-ray kinetic energy

$$\epsilon_k^{\delta} = \begin{cases} \epsilon_k \xi & r_2 \leq g(\xi) \\ \text{Go back to step 1.} & r_2 > g(\xi) \end{cases}$$

where $\xi_0 = \epsilon_{k,cut}/\epsilon_k$. This algorithm is shown to reproduce the δ-ray energy distribution in Figure 5.3, and is taken from the `Geant4` Physics Reference Manual [104].

The direction of the δ-ray momentum, $\mathbf{p}_\delta$ with respect to the incident hot electron momentum $\mathbf{p}_i$ can be expressed in terms of azimuthal, ϕ_δ and polar, θ_δ deflection angles, with an equivalent pair of angles, ϕ_e, θ_e describing the momentum of the scattered hot electron $\mathbf{p}_e$. We firstly assume that emission is isotropic in the azimuthal direction, so we randomly sample ϕ_δ and let $\phi_e = \pi + \phi_\delta$. As we have already sampled the δ-ray kinetic energy, we can

solve for the polar angles through conservation of energy and momentum

$$p_i = p_e \cos(\theta_e) + p_\delta \cos(\theta_\delta) \tag{5.30}$$

$$p_e \sin(\theta_e) = p_\delta \sin(\theta_\delta) \tag{5.31}$$

$$p_e = \frac{1}{c}\sqrt{((\epsilon_k + m_e c^2) + m_e c^2 - (\epsilon_k^\delta + m_e c^2))^2 - m_e^2 c^4} \tag{5.32}$$

$$p_\delta = \frac{1}{c}\sqrt{(\epsilon_k^\delta + m_e c^2)^2 - m_e^2 c^4} \tag{5.33}$$

which can be rearranged to give

$$\cos(\theta_e) = \frac{p_e^2 - p_\delta^2 + p_i^2}{2 p_i p_e} \tag{5.34}$$

$$\cos(\theta_\delta) = \frac{p_\delta^2 - p_e^2 + p_i^2}{2 p_i p_\delta} \tag{5.35}$$

where we have assumed our δ-ray electron is initially at rest. Particle rotation then proceeds via the method presented in Section 5.3.1.

5.7 Target normal sheath acceleration

The hybrid-PIC code simulates electrons travelling through the solid, but we must also consider what happens to the electrons when they break out from the target. As hot electrons pass from the solid out into the vacuum, they establish negatively charged sheath fields on the solid surface which reflect electrons back into the solid, and accelerate ions out in target normal sheath acceleration (TNSA). Recent studies [30, 76] have found that hot electrons lose energy when refluxing in the sheath field, providing an additional energy-loss mechanism in these systems as energy is transferred to ion acceleration.

In order to incorporate these effects into the hybrid-PIC code, we created special boundary conditions to emulate the complex electron refluxing behaviour. This behaviour was studied in both 1D and 2D full-PIC simulations of electrons refluxing in the sheath field, which were performed using the unmodified version of `EPOCH`. This characterisation study was similar to that performed by Rusby *et al* [76], and our simulation set-up, characterisation, and hybrid-PIC implementation is discussed in the remainder of this section.

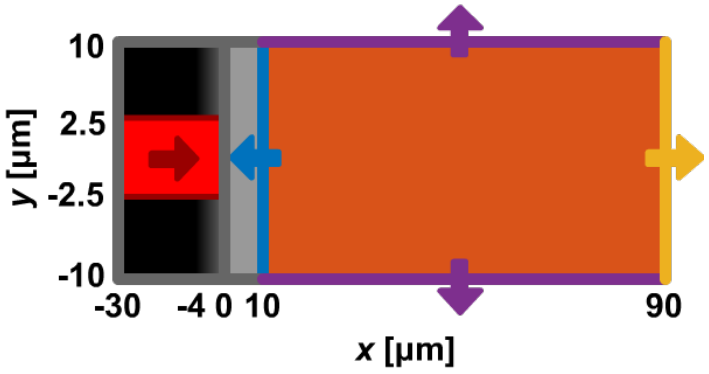

Figure 5.4: Schematic diagram to show how the end states of particles are characterised, and the path of the laser pulse. We monitor electrons starting in an exponential pre-plasma with 2 µm scale-length between $x = -4$ µm and $x = 0$ µm. Once these electrons pass the rear surface of the solid ($x = 10$ µm), they can reflux back into the solid (blue), remain outside the solid but within the simulation window (orange), or escape in the longitudinal (yellow) or transverse (purple) directions.

5.7.1 Simulation setup

Our 2D simulations study 10 µm fully ionised carbon targets, and 2 µm gold targets with an ionisation state of 51^+ (corresponding to a 5 keV ionisation potential, as in Vyskočil *et al* [30]). The solid-density regions of C and Au targets had electron number densities of 6.8×10^{29} m^{-3} [148] and 3.0×10^{30} m^{-3} [149] respectively. Both targets included a 4 µm exponential pre-plasma on the laser-facing side, with a 2 µm exponential scale length. The targets were simulated with shots from 10^{20} Wcm^{-2} and 10^{22} Wcm^{-2} laser pulses, creating 4 simulations in total.

In the C target simulations, square cells of side 20 nm were used, with 300 macro-particles per cell (1 in 6 were macro-ions, the rest macro-electrons). The simulation domain ranged -30 µm to 90 µm in x, and the target and simulation window spanned -10 µm to 10 µm in y. The laser pulse had a Gaussian profile with a 40 fs full width half maximum, and had a focal spot size of 5 µm, as shown schematically in Figure 5.4.

It was found that Au^{51+} targets required a greater resolution to suppress self-heating (see Section 5.7.2), and so these simulations ran with 5 nm cells and 150 ppc, for 160 fs in a smaller simulation window. This reduced window spanned -10 µm to 10 µm in x (pre-plasma $x = -4$ µm to 0, solid $x = 0$ to 2 µm), and from -4 µm to 4 µm in y. The temporal and spatial profiles of the laser pulse remained the same as the C runs, and all runs were performed with current smoothing.

To test the effects of refluxing over long time-scales, the C 10^{22} Wcm^{-2} simulation was repeated in 1D for an extended run-time of 10 ps. This simulation studied a target with the same pre-plasma structure as the 2D case, but had a larger solid density region between $(0 < x < 20)$ µm, in a simulation window which spanned $(-100 < x < 130)$ µm. The cell size was reduced to 10 nm, and the macro-particle per cell counts were increased to 600 for macro-electrons and 120 for macro-ions.

Simulations were run without collisions for computational efficiency. While this is a poor approximation for the cold background particles, the sheath fields develop according to the hot electron characteristics, which are mostly unaffected by collisions over the considered time-scales [150, 151]. Using the equation for calculating the elastic scatter angle (3.89), the time taken for a hot electron of energy $a_0 m_e c^2$ to scatter 90 degrees is at least eight times greater than the simulation run-time in all cases. The energy lost to collisions for this electron is estimated to be under 10% for all simulations according to the collisional stopping power (3.68).

In our simulations, we used enhanced particle probes which output particle momentum, ID and the time the particle passes the probe. By placing probes at $x = \{-29, 0, 10, 89\}$ µm in C simulations, we could categorise electrons leaving the solid by their four possible end-states, also summarised in Figure 5.4. Electrons could be reflected by the sheath field and reflux back into the target, or could possess enough energy to overcome the sheath field and escape through the $x_{\max}$ boundary. Electrons could also escape through a y-boundary in 2D simulations, but this doesn't tell us if they would escape the solid or if they would eventually reflux if we simulated more space in the y direction, so we consider these electrons lost. Finally, electrons could be absorbed into the sheath field, and end the simulation outside the solid region but still within the simulation window. Note that this "absorbed" category will also include refluxing and escaping electrons when the simulation ends before they can complete their journey.

In these characterisation studies, we only track the evolution of electrons which initially started in the pre-plasma ($x < 0$ µm), and only after passing the rear target surface for the first time. This is because the electrons may trigger the front probe multiple times on their way into the target, but they won't act like hot electrons until they possess the energy to fully traverse the solid. Hot electrons may reflux multiple times on both boundaries before escaping or becoming lost or absorbed, and each reflux event is treated separately.

The probe positions remain fixed throughout the simulation, although the plasma density distribution is expected to change over the simulation run-time. At later times, the rear probe will no longer describe a target-vacuum interface due to target expansion, but the probe information is still useful for two reasons. Firstly, if an appreciable plasma density exists beyond the probe, then electrons refluxing at the new target edge would be missed if the electron stops before returning to the probe. However, such electrons may no longer be considered hot if they lack the energy to return to the probe, and "absorbed" would still be a suitable label for them. Secondly, this characterisation is done to support a hybrid-PIC code with fixed edges, so only the properties of electrons passing the initial solid density boundaries are important.

5.7.2 Self-heating checks

When performing these PIC simulations, it is important to minimise the effects of self-heating. We are interested in the change in momentum when electrons reflux through boundaries, and so a non-physical increase in momentum would introduce errors into the analysis. To determine an acceptable level of self-heating, we turn to the sheath field characterisation study performed by Rusby *et al* [76]. Their study identified changing field strength on the electron as the dominant source of reflux energy loss, and they measured the change in electron temperature when refluxing on the rear surface. To perform these simulations, Rusby *et al* used the `EPOCH` PIC code to model He targets set to 50 times the critical density (5.58×10^{28} m^{-3} assuming $\lambda = 1$ µm), with 30 macro-particles per cell, N_{ppc} in square cells of side $\Delta x = 20$ nm. Their 2D simulations run for up to 1 ps, and while they make no mention of current smoothing or higher-order particle shapes, let us assume they are using the default `EPOCH` particle shape with current smoothing for comparison to our 2D runs. As 1D simulations have a reduced computational cost, it was possible to perform these with higher-order (5th-order) particle shapes.

To measure the extent of self-heating from our Section 5.7.1 parameters, we may simulate a small grid (10×10 cells) with the same N_{ppc} and Δx as the full simulation, and apply periodic boundary conditions. The particle number densities in these cells are set to match the solid-density region in the full simulations, and an initial temperature of 1.2×10^7 K (1 keV) is set for the electron and ion populations. It was found that 1D simulations had negligible self-heating over these time-scales, but some self-heating was present in 2D. The

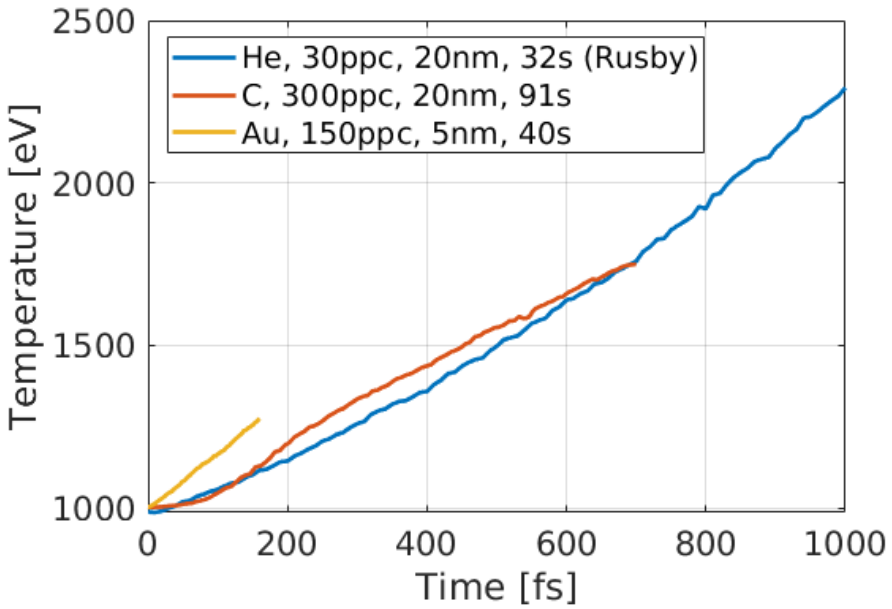

Figure 5.5: Self-heating in small-scale test simulations with the same parameters as the larger sheath-field characterisation studies. The heating present in Rusby *et al* [76] is compared to the simulation parameters described in Section 5.7.1. Each simulation is labelled in the legend with the target material, particle per cell count, square-cell width, and the run-time on 4 processors.

evolution of the cell-averaged temperature in 2D simulations is shown in Figure 5.5, where a comparison to the Rusby *et al* [76] parameters has been made. These quick test simulations verify that even though the rate of self-heating is higher in our simulations, the absolute heating is less than observed in similar studies due to our reduced run-time in 2D. We also show that the computation times are roughly comparable to those of Rusby *et al*, although we have to simulate shorter time-scales for our higher density simulations.

This level of self-heating is also acceptable from a physics perspective. The temperature increase in Figure 5.5 describes the heating of background particles, which remain cool compared to the hot electron population at all points in the simulation. Secondly, the typical time-scale for a hot electron reflux event was found to be 10-100 fs (see Section 5.7.3), and so any hot electron numerical heating would have a minimal effect when tracking the energy change over a reflux.

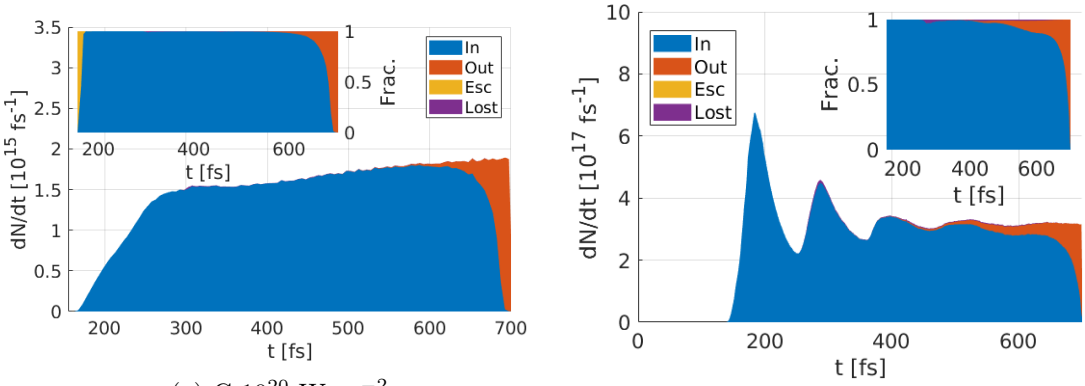

(a) C 10^{20} Wcm^{-2} (b) C 10^{22} Wcm^{-2}

Figure 5.6: The number spectra of electrons leaving the solid through the rear surface for the two carbon 2D simulations, binned by outgoing time. The plots are coloured to show the proportion of particles going into each of the four end-states. A normalised fraction of end-states is provided in the sub-figures to show areas which are under-represented in dN/dt.

5.7.3 Characterisation in 2D simulations

In Section 5.7.1, we discuss the set-up for the modelling of hot electrons exiting the solid density region in laser-solid interactions, and also the four possible end-states for particles once they have left the solid (Figure 5.4). We will begin by discussing the results of the 2D simulations in order to demonstrate the observed behaviour of electron refluxing. The 1D results are included in Section 5.7.4 to demonstrate how the 2D characterisation may be extrapolated to long time-scales.

Firstly, let us consider the fate of particles leaving the solid-density region at different times in the 2D simulations. In Figure 5.6, electrons are binned by the times they leave solid through the $x = 10$ µm (rear) probe in the C target runs, and the number spectrum of these particles was plotted and coloured according to the end-state of particles in each bin. Electrons can be counted more than once if they reflux back in and leave the target again.

Figure 5.6 shows that most electrons reflux back into the target, and we only see particles escaping through $x_{\max}$ early in the simulation before a sheath field is established (as seen in the Figure 5.6(a) insert for low t). While some electrons end the simulation in the vacuum region behind the solid, this mostly occurs for electrons exiting towards the simulation end. This rise in the "out" population is expected at later times, as some of these may be refluxing electrons which just happen to be outside the target at the simulation end. The lack of lost electrons suggests the transverse simulation window size is sufficient for capturing most

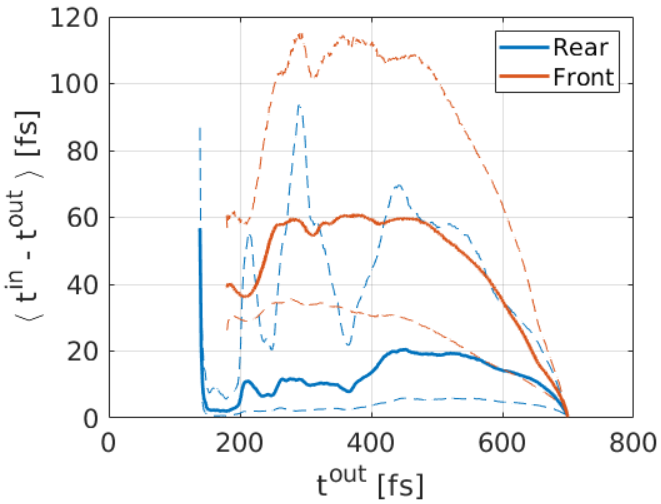

Figure 5.7: Solid lines depict the mean time taken for a reflux event on the rear (solid-vacuum) and front (pre-plasma to solid) surfaces, for electrons binned by outgoing times in the C 10^{22} Wcm^{-2} 2D simulation. The dashed lines denote the average deviation above and below the mean in each bin.

electron end-states.

To test if the rise in the "out" population could be explained by incomplete refluxing, refluxing electrons were binned by their outgoing time and the mean reflux time was calculated in each bin. These mean times are shown graphically in Figure 5.7 for the C 10^{22} Wcm^{-2} simulation. It was found that the typical time taken to reflux on the rear surface was around 10-20 fs, which can explain some of the rise in "out" states in Figure 5.6(b).

We then inspected the end states of particles after binning by outgoing total momentum, as shown in Figure 5.8. Again, in both C simulations we find the majority of electrons reflux back into the target, except for the highest energy electrons which escape. We also find that it is typically the lower energy electrons which end the simulation outside the solid. This implies that the high energy electron population still refluxing at the simulation end is small, as we would expect to see some caught outside mid-reflux if they were still refluxing at this point.

Figures 5.6 and 5.8 confirm that electrons mostly reflux back into the target when escaping through the rear solid boundary, but we can also look at how electron energy changes when refluxing. We binned refluxing electrons by the outgoing x-component of momentum on the rear boundary, p_x^{out} in all four simulations, and calculated the average value of $|p_x^{\text{in}}/p_x^{\text{out}}|$ in each bin. These curves have been shown in Figure 5.9, along with a shaded area

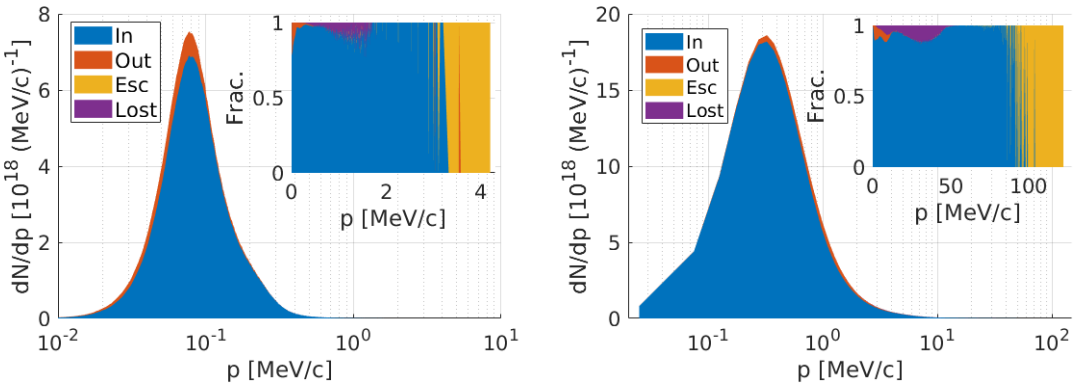

(a) C 10^{20} Wcm^{-2} (b) C 10^{22} Wcm^{-2}

Figure 5.8: The number spectra of electrons leaving the solid through the rear surface for the two carbon 2D simulations, binned by outgoing total momentum. The plots are coloured to show the proportion of particles in each of the four end-states. A normalised fraction of end-states is provided in the sub-figures to show areas which are under-represented in dN/dp.

to show the variation of the momentum change in each bin.

We find the momentum loss behaviour is quite similar for targets of different thickness and density, and is qualitatively similar at different laser intensities. The highest energy electrons seem to lose the most energy when refluxing, with the lower energy electrons staying at similar p_x magnitude when returning. The lowest energy electrons appear to gain energy when refluxing, but these results may be less accurate as self-heating will have a larger proportional effect on lower energy electrons. The different qualitative behaviours at different laser intensities may be due to different laser absorption characteristics. In C simulations, the ratio of injected hot electron energy to total laser energy, $\eta_{l\to e}$ was 0.27 in the 10^{22} Wcm^{-2} run, but only 0.03 in the 10^{20} Wcm^{-2} run. This reduction in absorbed energy could explain the reduced peak momentum achieved relative to the ponderomotive momentum $a_0 m_e c$ for the 10^{20} Wcm^{-2} simulations.

As seen in Figure 5.8, the majority of probe-hits occur for lower energy electrons. Hence, it is also useful to look at the total momentum loss in each bin to see where the electron energy is going, as shown in Figure 5.10. Figure 5.10(a) shows that most of the longitudinal momentum is lost by the lower energy electrons. A loss of longitudinal momentum agrees with observations by Vyskočil *et al* [30], who suggest the loss would explain the increase in bremsstrahlung emission angle. Our results go further, and suggest that an increased angle can be attributed to both a decrease in p_x, and an increase in p_y when refluxing.

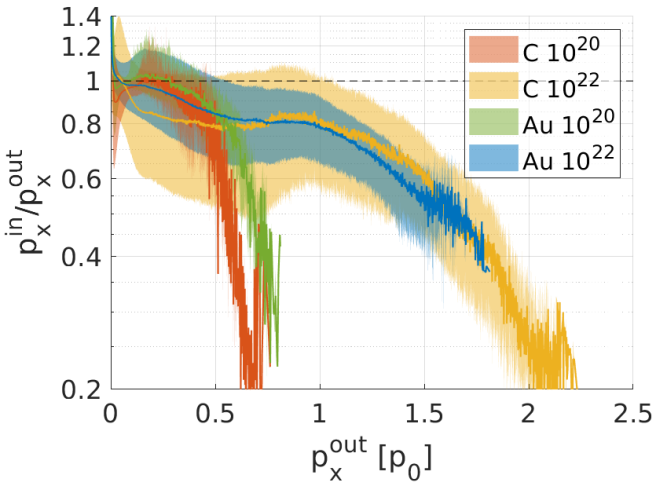

Figure 5.9: The longitudinal momentum loss in a refluxing event on the rear solid surface, binned by outgoing hot electron momentum in 2D simulations. The solid line shows the average momentum change in a bin, and the shaded regions represent the average deviation both above and below the solid line. The dotted line represents no change in the momentum magnitude - everything below has lost momentum, everything above has gained it. The outgoing momentum is in units of the ponderomotive momentum $p_0 = a_0 m_e c$, and simulations are labelled by the target material, and the laser intensity in Wcm^{-2}.

This relationship is less clear in the higher intensity Figure 5.10(b), but we still observe a dominant loss in longitudinal momentum and a gain in transverse momentum.

We also note that the gain in p_y is less than the loss in p_x, and so on average, electrons lose energy when refluxing. The average loss of total momentum during a reflux event has been calculated for each boundary in each simulation, and is given in Table 5.2.

Target	$\langle \Delta p \rangle$ [keV/c]		
	Front	Rear	Total
10^{20} Wcm^{-2}, C	-28.2766	-3.82309	-7.46456
10^{20} Wcm^{-2}, Au	-112.953	-3.04252	-6.95298
10^{22} Wcm^{-2}, C	-159.474	-196.172	-180.774
10^{22} Wcm^{-2}, Au	-139.194	-141.853	-141.149

Table 5.2: Mean total momentum changes for all refluxing electrons, broken down into front reflux events (solid into pre-plasma), rear reflux events (solid into vacuum), and all reflux events combined.

As the momentum components are changing in different ways, the angular spectrum of electrons leaving the solid will be different to the spectrum of electrons coming back in. These spectra are compared for rear boundary refluxing electrons in Figure 5.11 for the two

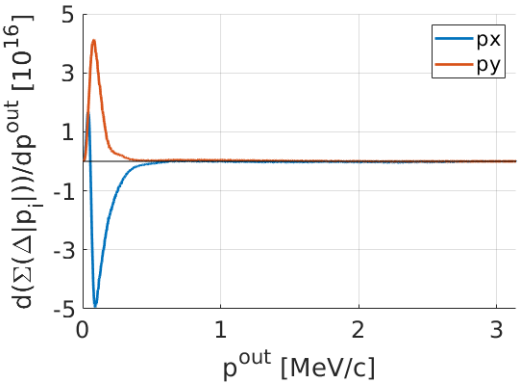

(a) C 10^{20} Wcm^{-2}

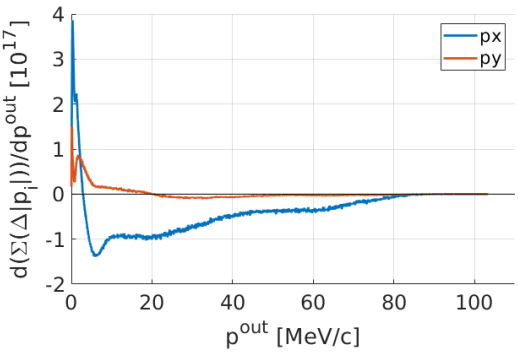

(b) C 10^{22} Wcm^{-2}

Figure 5.10: Electrons which reflux on the rear surface are binned by their outgoing total momentum. The changes in the momentum component magnitude ($\Delta|p_i| = |p_i^{\text{in}}| - |p_i^{\text{out}}|$) are summed over all electrons in the bin, and $d(\Sigma(\Delta|p_i|))/dp^{\text{out}}$ is plotted for p_x and p_y. Thus, the area under the curve between two p^{out} limits represents the total p_i change for refluxing electrons exiting between these p^{out} limits. No p_z change has been plotted, as this remained 0 for all particles in our 2D simulations.

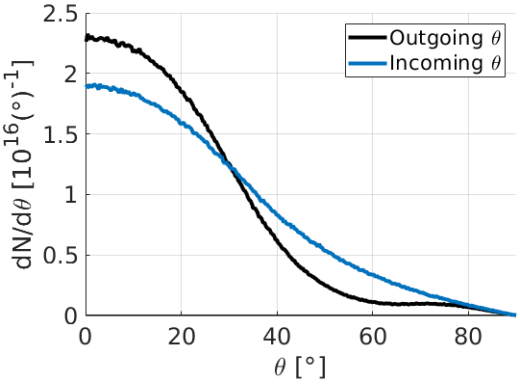

(a) C 10^{20} Wcm^{-2}

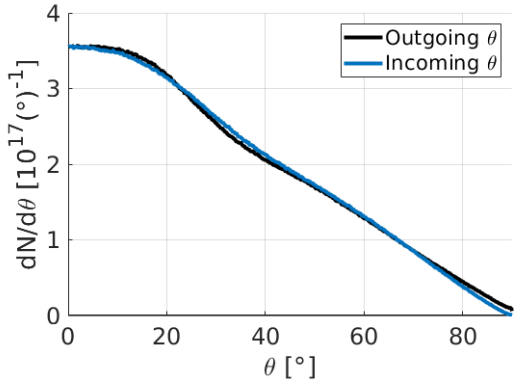

(b) C 10^{22} Wcm^{-2}

Figure 5.11: Angular distributions of refluxing electrons when escaping the solid target (outgoing) and returning to the solid (incoming) for rear surface reflux events.

C simulations. In Figure 5.11(a) we see the angular spectra tending to a more uniform distribution, while we see little change in the total spectrum in the higher intensity Figure 5.11(b).

We can characterise the angular distributions for refluxing electrons further. In Figure 5.12, we bin refluxing electrons by their outgoing angle, and compare it to their incoming angle. On average, we find that electrons with low θ typically come back in with a larger angle to the laser axis, and electrons leaving with high θ come back lower.

Despite little change in the Figure 5.11(b) data, we can see from Figure 5.12 that there

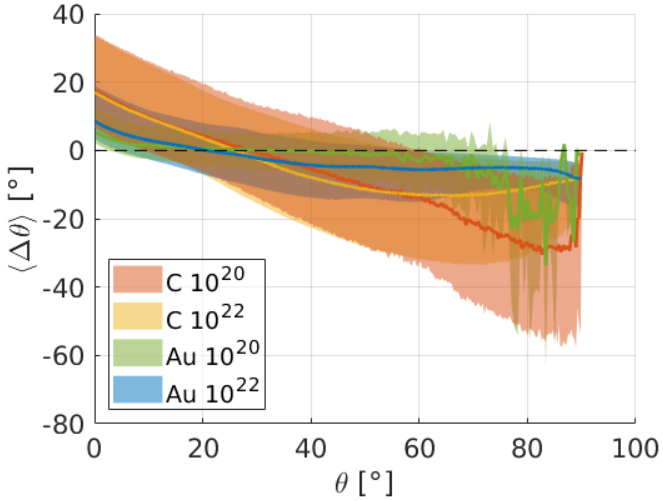

Figure 5.12: Refluxing electrons were binned by their outgoing angle with respect to the laser axis θ when leaving the solid on either the front or rear surfaces. The mean angle change upon returning to the solid has been calcuated in each bin, and is shown as the solid line for all 4 simulations. The upper and lower shaded regions span up to the average deviation $|\Delta\theta - \langle\Delta\theta\rangle|$ for all electrons above and below $\langle\Delta\theta\rangle$ respectively.

is still some scatter when refluxing. As the shaded area of uncertainty remains a similar size for all outgoing θ, this could provide a useful measure in characterising the amount of scatter in a reflux event. The average values of the bin uncertainty range $\sigma_{\langle\Delta\theta\rangle}$, weighted by the number of electrons in each bin, have been provided in Table 5.3.

Target	$\sigma_{\langle\Delta\theta\rangle}$ [°]		
	Front	Rear	Total
10^{20} Wcm^{-2}, C	27.609	25.398	27.2838
10^{20} Wcm^{-2}, Au	10.2631	14.8376	10.4962
10^{22} Wcm^{-2}, C	27.3305	34.8999	31.7729
10^{22} Wcm^{-2}, Au	15.0984	30.796	21.7208

Table 5.3: Mean widths of the shaded error region in Figure 5.12. This mean-width is calculated using an average weighted by the number of electrons in each bin.

5.7.4 TNSA boundaries

As shown in Section 5.7.3, hot electrons execute complex behaviours when leaving the solid. Such sheath fields cannot be modelled in our hybrid-PIC code, so we instead seek to create special boundary conditions which can emulate the observed behaviour. This has led to the introduction of a reduced reflux model, characterised by 3 empirical parameters: κ_{esc}, κ_{tnsa}

and $\sigma_{\langle\Delta\theta\rangle}$.

The κ_{esc} parameter is prompted by the sharp switch in end-states seen in Figure 5.8, and describes the energy required to escape the solid in the x direction. Here, κ_{esc} is defined such that $\kappa_{\text{esc}} a_0 m_e c^2$ is the energy associated with the first bin in Figure 5.8 which had all electrons escape after passing into the vacuum. In our boundary conditions, all electrons which reach the boundary with energy below $\kappa_{\text{esc}} a_0 m_e c^2$ are reflected back into the simulation window, and the rest are removed from the simulation. This characterisation is limited by the dimensionality of the code, as 2D sheath fields will decay slower with distance than fields in 3D space, so these cut-off energies are likely over-estimates.

From figures 5.6 and 5.8 it is clear that most electrons reflux, and figures 5.9 and 5.10 show that reflux events typically result in some energy loss. Hence, the κ_{tnsa} parameter is defined such that $\kappa_{\text{tnsa}} a_0 m_e c$ is the average momentum loss for all hot electrons exiting and re-entering the solid on both the front and rear sides. When macro-electrons reflux in the hybrid-PIC code, their momentum will be reduced by $\kappa_{\text{tnsa}} a_0 m_e c$ to model this reflux energy loss. The limitation in this parameter is the over-simplification of the energy loss properties. In Figure 5.9, we see that high energy electrons typically lose a large proportion of their total energy in a reflux. Hence, we may over-estimate how far high energy refluxing electrons will travel in the solid.

Finally, to describe the angular scatter seen in Figure 5.12 we use the $\sigma_{\langle\Delta\theta\rangle}$ parameter. The actual $\langle\Delta\theta\rangle$ values are ignored as there seems to be a large and roughly constant range of scatter angles for all outgoing angles, which suggests refluxing provides a random scatter process. We define $\sigma_{\langle\Delta\theta\rangle}$ as the average size of the shaded area across all bins in Figure 5.12, weighted by the total electron weight in each bin. These shaded regions denote the upper and lower average deviation from the bin-average in each bin. When electrons reflux from a simulation boundary in the hybrid-PIC code, the reflected momentum will undergo deflection by an angle randomly sampled from $\pm 0.5\sigma_{\langle\Delta\theta\rangle}$, with an azimuthal angle randomly sampled between 0 and 2π.

These parameters were calculated for all four 2D simulations (160-700 fs), and the 1D simulation (10 ps), and have been summarised in Table 5.4. The parameters are shown to be similar across the 2D simulations, although there are some disagreements at longer time-scales. In the 1D simulation, it was found that there was no electron energy bin which had a 100% escape chance, and so no κ_{esc} parameter could be assigned. This can be attributed

to the field solver in 1D simulations, as the electric field does not decay with distance as it does in 2D or 3D. The lower value of $\sigma_{\langle\Delta\theta\rangle}$ may also be a feature of 1D simulation, as this code could not model a transverse sheath field structure which may have influenced the change in p_y during a reflux. Despite this, the comparable value of κ_{tnsa} suggests the 2D characterisations may still hold over multi-picosecond time-scales.

Run	Parameters		
	κ_{esc}	κ_{tnsa}	$\sigma_{\langle\Delta\theta\rangle}$ [deg]
10^{20}, C (2D)	0.81	1.7×10^{-3}	27
10^{20}, Au (2D)	0.75	1.6×10^{-3}	10
10^{22}, C (2D)	1.9	4.2×10^{-3}	32
10^{22}, Au (2D)	1.6	3.2×10^{-3}	22
10^{22}, C (1D)	N/A	1.2×10^{-3}	9

Table 5.4: Reflux boundary characterisation parameters from full-PIC simulations, labelled by laser intensity in Wcm^{-2}, and target material.

Chapter 6

Benchmarking

The bremsstrahlung radiation routines of Section 4.5.2 and the hybrid-PIC code presented in Chapter 5 both introduce many new physics packages to the `EPOCH` code. To ensure these modules are working accurately, we have created a suite of benchmarks designed to test each individual addition. Some benchmarks test the code against actual experimental results, which helps to verify the usefulness of the code for real-world applications. Here we expect only qualitative agreement with the data, as true experimental conditions are difficult to reproduce. Our simplified macro-electron injector in hybrid-PIC simulations will only approximately describe the true injection characteristics, as these are complicated by non-perfect focal spots and pre-plasmas which are not typically reported alongside the experimental results.

For precision tests of individual routines, we turn to numerical benchmarks. Here the outputs from our code are tested against other codes or analytic solutions. These benchmarks allow more control over the initial conditions in each code, and more direct quantitative agreement can be sought. However, such benchmarks are less rigorous as they do not test the code against real results, only simulated ones. These numerical benchmarks have been grouped in Section 6.1, with the remaining sections describing experimental benchmarks.

6.1 Numerical benchmarks

In some cases, experimental evidence was not available, and we instead compare the results of `EPOCH` against the Monte Carlo electron transport code `Geant4`. These presented a greater degree of control over initial conditions than experimental results, and a high level of

agreement between the codes could be expected. Whenever Geant4 lacks the functionality to test the physics of interest, simple prototype programs have been written in MATLAB for comparison.

6.1.1 Møller scatter δ-rays

To test the creation of δ-rays, the hybrid-PIC code ran simulations which injected 10^5 electrons of kinetic energy 50 MeV into an aluminium target. This injection was achieved by passing 10^5 macro-electrons of unit weight through the $x_{\min}$ boundary, for a simulation window which spanned 0-101 µm over 128 cells in x. Higher dimensions were 8 cells wide spanning 20 µm, with periodic boundary conditions to simulate targets of infinite transverse area. In the input deck, the fields and electron physics routines were switched off with only ionisation energy loss remaining on. Discrete emission and hot electron recoil were considered for δ-rays over 1 keV kinetic energy, but only δ-rays above 50 keV energy were actually added to the simulation window as macro-particles. An EPOCH probe was positioned at 100 µm to detect passing electrons and δ-rays, and the angular distributions and energy spectra of the particles were recorded.

This set-up was repeated in Geant4 for simulations using ionisation energy loss, but which had all other electromagnetic physics processes removed from the physics library. Here, electron and δ-ray momenta were output as they escaped through the rear surface of a 100 µm aluminium volume. Figure 6.1 shows the energy and angular spectra of all electrons (both original and δ-rays) passing the 100 µm point.

This figure shows that the two codes have good agreement. It can be seen that most electrons remain close to 50 MeV, but a smaller peak in the energy spectra is also present at low electron energies, which corresponds to the δ-rays added to the simulation. The angular distributions of electrons passing the probe are similar in both codes, but EPOCH over-estimates the large angle scatter. This is because Geant4 also considers the binding energy of the δ-ray electron when calculating the energy and momentum conservation (5.30). As this is a small effect which mostly affects lower energy electrons, this is ignored in EPOCH and δ-rays are initially considered free and at rest.

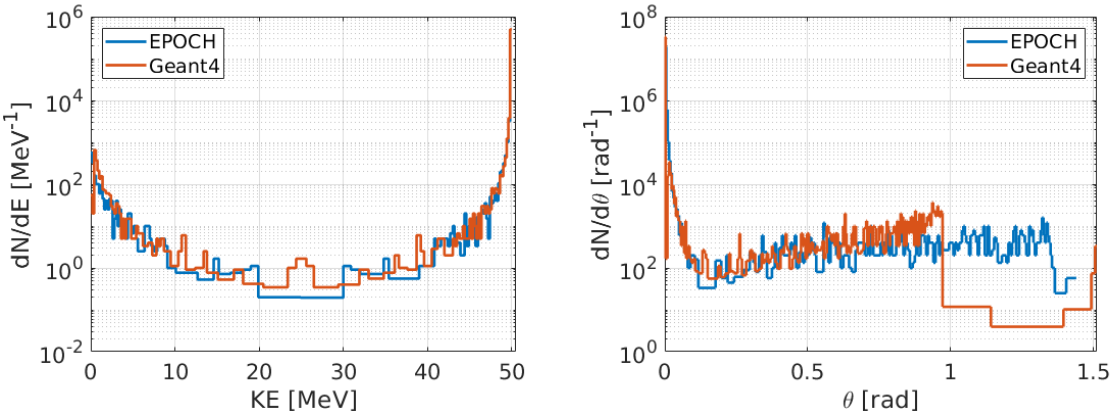

(a) Electron energy spectrum (b) Electron angular distribution

Figure 6.1: The energy spectrum (a) and angular distribution (b) of electrons passing 100 µm in an Al target. The initial bunch consisted of 10^5 forwards-propagating electrons ($\theta = 0$), with kinetic energy 50 MeV. Simulations were performed in both `EPOCH` and `Geant4`.

6.1.2 Thermal equilibration

Thermal equilibration describes the rate of thermal transfer between background electron and ion populations, and is derived from Coulomb collisional theory as discussed in Section 3.4.6. We were unable to find experimental data for the temporal evolution of electron and ion temperatures in a solid, so a simple numerical integrator was built for the thermal equilibration equations (5.5) and (5.6) in `MATLAB`. This analytic solution was tested against a hybrid-PIC `EPOCH` simulation, where the only physics package switched on was thermal equilibration, and no macro-particles were injected. The electron and ion temperatures were initialised to 100 eV and 50 eV respectively, and an aluminium target was considered. Figure 6.2 shows the temporal equilibration of temperature for both `MATLAB` and `EPOCH`, demonstrating a good agreement between the two codes.

6.1.3 TNSA boundaries

The boundary conditions for the hybrid-PIC code allow high energy macro-electrons to escape, while lower energy macro-electrons are reflected with some energy loss and scatter as discussed in Section 5.7. To test the correct implementation of these conditions, an input deck was constructed to trigger all the boundary physics. This simulation injected two electron bunches, one with a mean kinetic energy of 100 MeV, the other with 5 MeV. Here, the escape kinetic energy threshold was set to 10 MeV, momentum loss was set to 1 MeV/c,

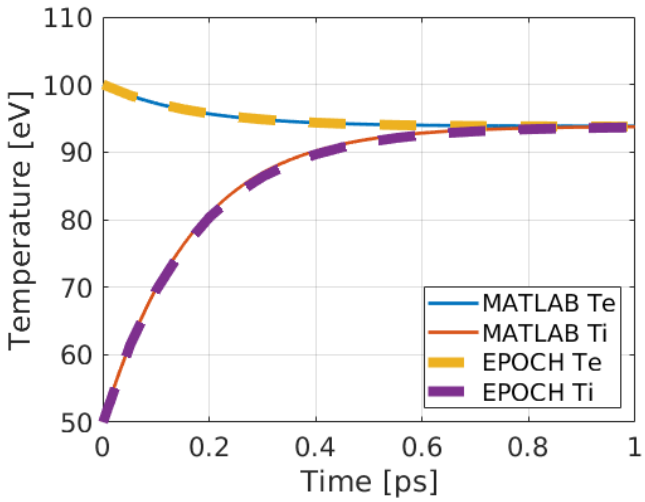

Figure 6.2: The temporal evolution of temperature for ions T_i and electrons T_e in an aluminium target. The `EPOCH` hybrid-PIC code is tested against a `MATLAB` prototype to demonstrate that the thermal equilibration routines are behaving as expected.

and the scatter angle uncertainty was set to 20°. These simulations had the field solver and electron physics switched off, and so the only feature capable of changing the injected electron momenta was the boundary treatment.

In these simulations, it was found that all 100 MeV electrons passed through the TNSA boundary as expected from the escape energy threshold. All of the 5 MeV electrons were reflected with a momentum magnitude change of -5.341 $\times$ 10^{-22} kgms^{-1}, also as expected from the κ_{tnsa} parameter chosen. To demonstrate the scatter behaviour, Figure 6.3 shows the outgoing angles for the reflected electrons. This figure shows scatter into angles which are uniformly distributed between $\pm 10°$, which demonstrates the desired behaviour.

6.1.4 Classical bremsstrahlung

Two potential implementations of bremsstrahlung radiation are discussed in Section 4.5.2: a method by Wu *et al* [128] based on classical theory and another following the quantum theory from Seltzer and Berger [38]. Both methods were tested in `EPOCH` simulations, and were compared to the Seltzer-Berger implementation in `Geant4`. In this section, the classical `EPOCH` model is compared to the quantum `Geant4` model for systems of interest to this project, to study the usability of a classical description. These simulations followed the passage of 10^5 electrons (initial energy 100 MeV) traversing to a plane displaced 5 mm away from the injection point in the initial electron momentum direction.

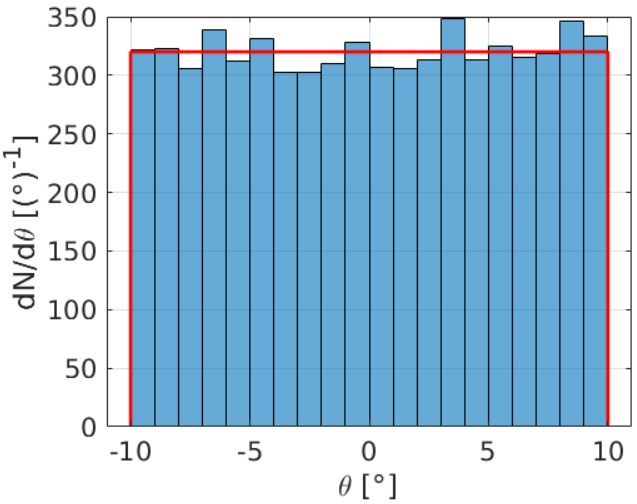

Figure 6.3: Angular distribution of an electron bunch below the escape energy threshold after refluxing through a hybrid TNSA boundary. All electrons approached the boundary with $\theta = 0$. The solid red line shows the expected reflected distribution from our empirical model, corresponding to a uniform distribution between $\pm 10°$.

In `EPOCH`, these electrons were represented by macro-particles of unit weight which populated the first cell in the x-direction. Each cell had a width of 21.5 µm (the first cell spanned $x = 0$ to $x = 21.5$ µm), and the background material was represented by immobile neutral macro-particles at solid density for Al and Au targets. The self-generated fields in the electron bunch were negligible over the distances considered, and the only other process acting on the electrons was bremsstrahlung radiation. The electron energy spectra were recorded as electrons passed the $x = 5$ mm probe, and are plotted in Figure 6.4. The classical bremsstrahlung model used the differential cross section given in (4.27) for $Q = 0$, and assumed photons were emitted in the electron direction (ultra-relativistic electron approximation).

The electron energy spectra from `Geant4` were computed in a similar way, using a reduced physics library which only sampled bremsstrahlung emission. Electron energies were recorded as electrons escaped the 5 mm thick target, and make up the `Geant4` (Seltzer-Berger) curves in Figure 6.4. This figure demonstrates the limitations of the Wu *et al* [128] model for bremsstrahlung radiation, as the emitted spectrum deviates from the quantum results outside the complete screening limit.

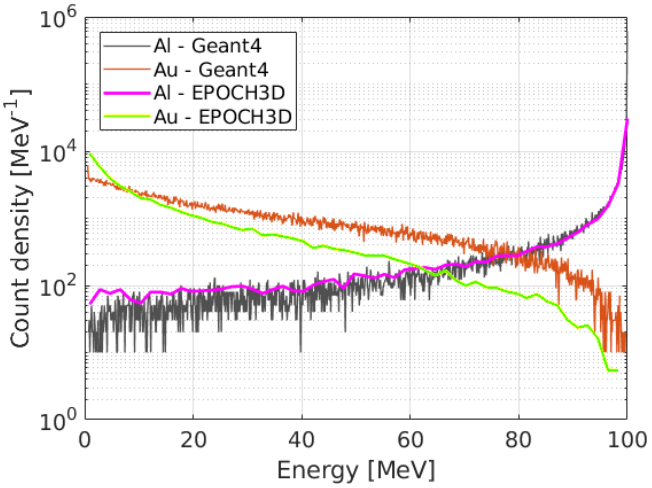

Figure 6.4: Electron energy spectra obtained after 10^5 electrons of initial energy 100 MeV passed through 5 mm of different atomic targets. The results of `Geant4` are compared to equivalent runs in `EPOCH` using the classical bremsstrahlung model given by (4.27).

6.1.5 Quantum bremsstrahlung

Following the inadequacy of the classical implementation of bremsstrahlung radiation (see Section 6.1.4), the Seltzer-Berger cross section tables [38] were incorporated into `EPOCH` and are now included in the official `EPOCH` release. In order to test that this has been implemented correctly, a comparison experiment was set-up between `EPOCH` and `Geant4` as in Section 6.1.4. In this section, we also sought to benchmark the angular distribution routines for photon emission and electron recoil.

A version of `Geant4` was modified such that the electromagnetic physics library only contained bremsstrahlung routines. In these bremsstrahlung-only simulations, a beam of 10^5 electrons of total energy 100 MeV was injected into a 5 mm gold target. The momenta of electrons as they passed the 5 mm point were recorded, and photon momenta were recorded after the photons had taken their first step. This simulation was performed twice: once with Grichine's dipole model for angular bremsstrahlung emission [152], and again with the Tsai sampling method [104,131,132]. While the Grichine sampling method is the default angular distribution model in `Geant4`, we chose to use the Tsai model in `EPOCH` as this is the method discussed in the `Geant4` documentation. The equivalence of these methods is shown in these simulations.

The simulation was repeated in `EPOCH`, where an electron bunch was initialised in the first cell of a gold target, and travelled to a particle probe positioned at 5 mm. This bunch

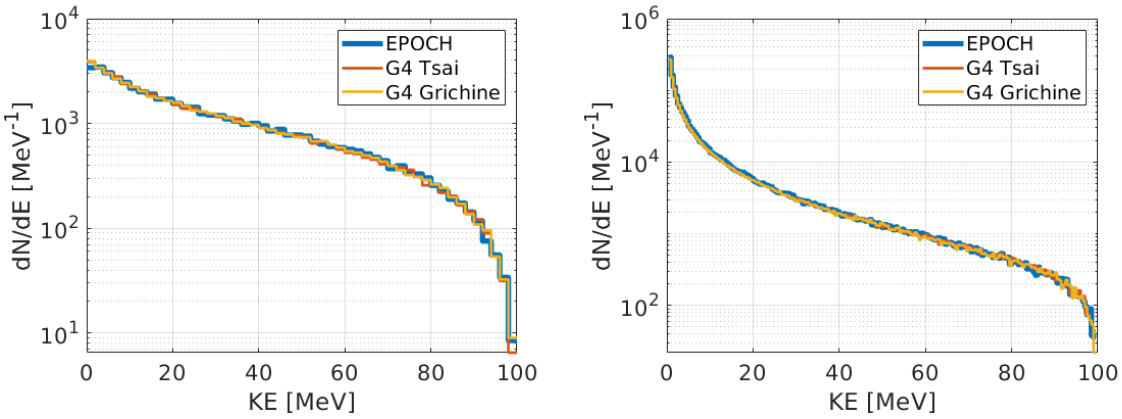

(a) Electrons (b) Photons

Figure 6.5: Energy distributions from a 100 MeV electron bunch (10^5 electrons) when passing the probe at 5 mm, from the `Geant4` and `EPOCH` simulations. `Geant4` data is given for both Tsai and Grichine angular bremsstrahlung models.

consisted of 10^5 real particles, and was given a drift momentum equivalent to setting a total electron energy of 100 MeV for consistency with the `Geant4` run. The bremsstrahlung photons were made immobile, but electron recoil due to photon emissions was still applied. Photons below 500 keV energy were not added to the simulation (and the angular scatter is neglected), and so these photons were also ignored in the `Geant4` data when plotting spectra.

Once these simulations were run, a set of spectra was obtained for comparison between the two codes. Figure 6.5 measures the energy distributions of electrons at 5 mm and photons upon creation. This verifies agreement between the quantum implementation of bremsstrahlung radiation in `EPOCH`, and the models used in `Geant4`. Figure 6.6(a) shows the angular distribution of electrons as they pass the probe at $x = 5$ mm. In the absence of angular scattering, we would expect all particles to register $\theta = 0$ (no deflection from the original direction).

As can be seen, the angular electron distribution from `EPOCH` shows good agreement with the two different `Geant4` models, which suggests the electron recoil is being calculated correctly. The slight discrepancies at high θ come from the finite run-time of the `EPOCH` simulations, as electrons with larger scattering angles take longer to reach the $x = 5$ mm particle probe than can be reasonably simulated. However, the `Geant4` simulations run until all particles escape the volume, and so even electrons with high θ run to completion. Figure 6.6(b) shows the angular distribution of photons upon creation, and demonstrates that the photon directions are being sampled correctly too.

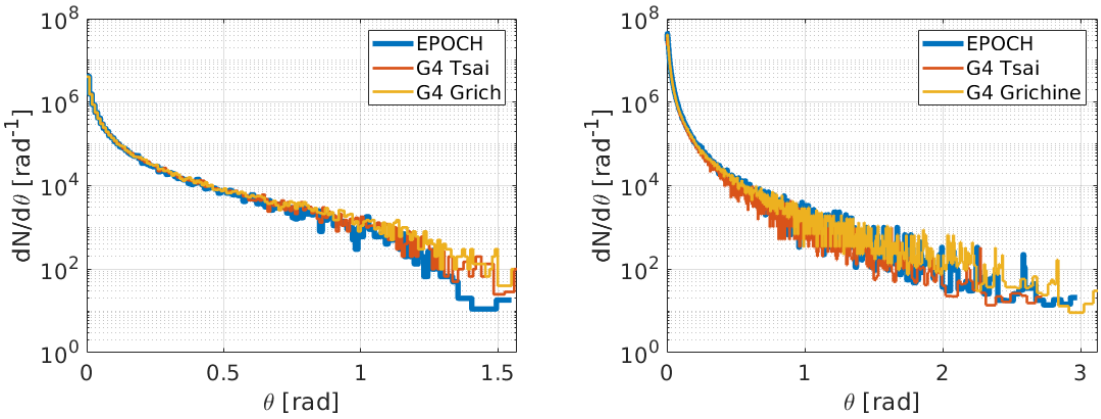

(a) Electrons (b) Photons

Figure 6.6: Angular distributions from a 100 MeV electron bunch (10^5 electrons) when passing the probe at 5 mm, from the `Geant4` (Tsai and Grichine models) and `EPOCH` simulations. Here the angle is with respect to the initial direction of the electron bunch.

6.2 Elastic scatter

The elastic scatter routines in the hybrid-PIC code can be benchmarked against the experimental results of Hanson *et al* [153]. Their experiment measured the elastic scatter of 15.7 MeV electrons traversing gold foil targets, and we attempt to recreate the scatter distribution shown in their Figure 3, for the 18.66 mg/cm^2 (9.67 µm) target. The `EPOCH` input deck injected 15.7 MeV (kinetic energy) electron bunches into gold targets with a particle probe positioned at 9.67 µm. The field solver and all electron physics were switched off, with the exception of electron elastic scatter routines. The decision to switch off physics processes was due to the short target size, low electron current and high electron energy present in this simulation, which implies field effects and radiation play a negligible role in the electron scatter. The code injected electrons from the $x_{\min}$ boundary, with open boundaries on $x_{\min}$ and $x_{\max}$, and reflective boundaries in y and z. In total, 4.8×10^4 macro-electrons were injected into the simulation window, and passed through cubic cells of side 100 nm. The resulting scatter distribution is shown in Figure 6.7.

For most electrons the scatter distribution has good agreement with the Hanson data, but `EPOCH` does a poor job recreating the rarer large angle scatter events. This is unsurprising, as the equations used to derive the elastic scatter model, (3.89) assumed small angle scatter events only. As large angle scatter events are rare in these systems, it is unclear from Figure 6.7 how much this uncertainty would affect the macroscopic properties of the system. This

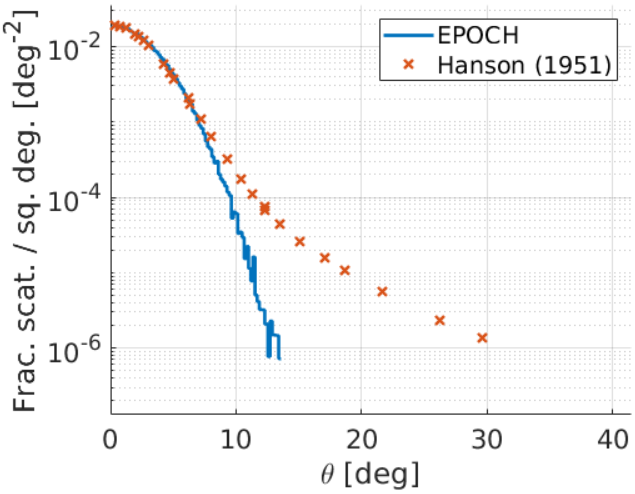

Figure 6.7: The fraction of injected 15.7 MeV electrons passing a particle probe placed 9.67 µm away from the injection point in a gold target. This number is normalised to the solid angle traced by each θ bin, in units of square degrees. The simulated scatter results are compared to the experimental findings of Hanson *et al* [153].

is addressed in Section 6.3.

6.3 Ionisation loss

This benchmark tests both the elastic scatter and continuous ionisation energy loss routines. The experimental data comes from Lockwood *et al* [154], where energy deposition was measured from electron beams passing through a variety of targets from different angles of incidence. Here, we reproduce the depth-dose curve for normal incidence 0.5 MeV electrons in tantalum, as shown in pages 100 and 101 of their report [154]. These simulations injected 0.5 MeV electron bunches, and the deposited energy was inferred from the temperature increase and heat capacity of the solid. This benchmark only tests heating of the target due to ionisation energy loss, as the electron currents in this beam are assumed too low to generate significant Ohmic heating.

The `EPOCH` simulations modelled elastic scatter and ionisation energy loss, with all other physics switched off. Due to the low electron energy present, δ-ray emission was not considered. Cells of dimensions $590 \times 250 \times 250$ nm^3 split up a simulation window of size $150 \times 2 \times 2$ µm^3, labelled in $x \times y \times z$ order. In total, 3200 macro-electrons of unit weight were injected through the $x_{\min}$ boundary, where x boundaries were treated as open, and y and z boundaries were periodic. These open x boundaries were important as it was found some electrons

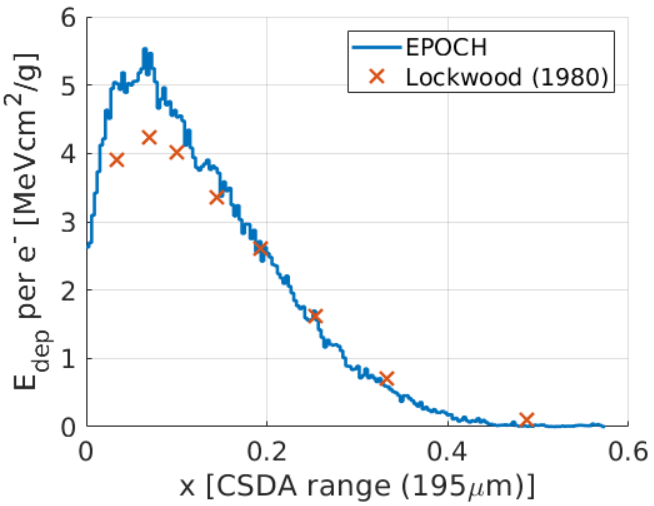

Figure 6.8: Energy deposition as a function of depth for 0.5 MeV electrons in tantalum. The depth, x is measured in units of expected range of electrons in the material, using the continuous slowing down approximation (CDSA). The energy deposition is quoted as the total energy deposited in MeV per x bin size (cm) per material density (g/cm^3), divided by the total number of incident electrons. The `EPOCH` results are compared to the experimental data of Lockwood *et al* [154].

were deflected over 180°, and open boundaries allowed electrons to escape from the front of the target. Figure 6.8 shows depth-dose curves created using the `EPOCH` hybrid-PIC mode.

The code produces reasonable agreement with the experimental data, with the greatest uncertainties appearing at low x (high scatter). These discrepancies may be attributed to approximations made in the elastic scatter routines, as ionisation energy loss is incapable of scattering electrons without δ-ray emission, and the scatter controls how far electrons penetrate into the target.

6.4 Electron stopping power

In order to test the ionisation and bremsstrahlung energy loss mechanisms for electrons, we repeat the test performed by Wu *et al* [128] and measure the total electron stopping power. This benchmark injected five electron bunches at different energies, and calculated their energy loss and step size each step. The electrons in these bunches had kinetic energies sampled from uniform distributions with mean energies given by $\langle\epsilon_k\rangle$, and energy ranges between $0.01\langle\epsilon_k\rangle$ and $1.99\langle\epsilon_k\rangle$. To sample enough electrons to span multiple orders of magnitude, the five injectors used $\langle\epsilon_k\rangle$ values of 50 keV, 500 keV, 5 MeV, 50 MeV and 500 MeV.

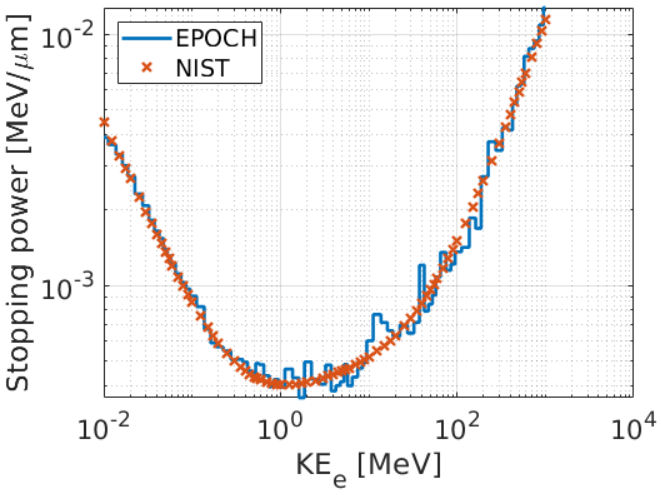

Figure 6.9: Stopping power of electrons in Al targets, as a function of the electron kinetic energy.

Each injector added 10^4 macro-particles to the simulation window, which spanned $35 \times 2 \times 2$ μm^3 and was split into cells of size $68 \times 250 \times 250$ nm^3 (using $x \times y \times z$ order). In order to get a smoother bremsstrahlung curve, the photon weight was reduced to 0.005, which makes emission 200 times more likely. The bremsstrahlung macro-photons were assigned reduced macro-particle weights, equivalent to 0.005 the weight of the emitting macro-electron to conserve real particle number, which also reduced the electron recoil from momentum conservation.

The electron stopping powers are shown in Figure 6.9 for an Al target, plotted alongside the expected NIST stopping powers [155]. These results were obtained from tracking electrons by their particle ID in the output dumps, and saving the kinetic energy and particle position at each dump. Electrons could then be binned by the kinetic energy in each step, and stopping powers were calculated by taking the ratio of energy lost to distance travelled by each electron between subsequent steps, with the average stopping power calculated for each bin. The simulation was run for 100 fs, and output dumps were written every 1 fs. Figure 6.9 shows excellent agreement between `EPOCH` and NIST, recreating both the ionisation-driven peak at low electron energies, and the high energy bremsstrahlung-driven regime.

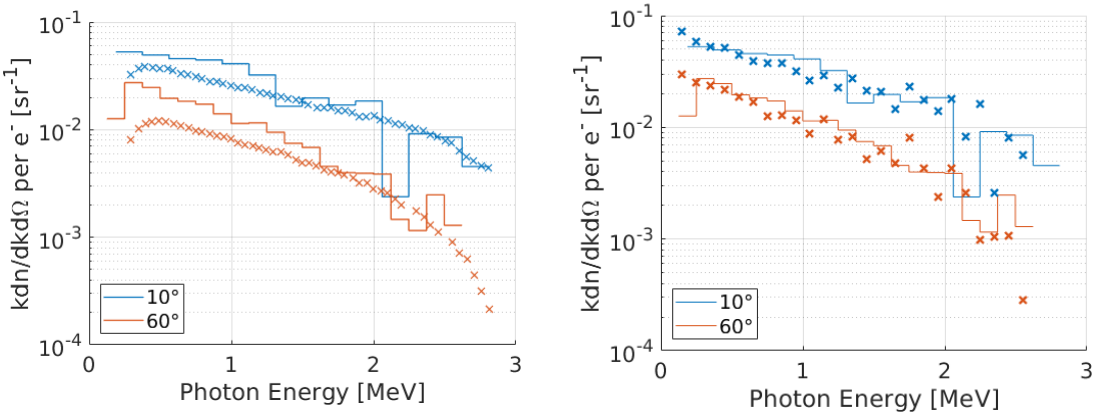

(a) EPOCH vs Rester (1970)

(b) EPOCH vs Geant4 without photo-electric effect

Figure 6.10: Energy spectra of bremsstrahlung radiation from 2.8 MeV electrons traversing a 1.176 mm gold target. Bremsstrahlung photons have been grouped by outgoing direction relative to the electron injection axis, θ. The energy spectrum is given as the total X-ray energy in a photon energy bin, divided by the product of the bin energy range, the total number of injected electrons, and the solid angle range of the θ bin (which spans $\pm 5°$ of the quoted angle for simulated data). The solid line in both figures is the EPOCH data, and the crosses denote the experimental Rester data in (a), and results from a Geant4 simulation with all physics switched on apart from the photo-electric effect in (b).

6.5 Bremsstrahlung photon production

While Section 6.4 considered the electron energy loss due to bremsstrahlung radiation, the emission of X-rays was not tested. We benchmark X-ray production by reproducing the experimental bremsstrahlung spectra shown by Rester *et al* in their Figure 17 [156]. This experiment measured the X-ray energy spectrum created when 2.8 MeV electrons passed through a 2.27 g/cm^2 thick (1.176 mm) gold target, for X-rays escaping the target at 10° and 60° to the electron injection direction.

The EPOCH simulations injected 5×10^4 electrons of energy 2.8 MeV and weight 0.2 into a 1.176 mm gold target, with elastic scatter, ionisation loss and bremsstrahlung switched on. The minimum photon energy added to the simulation was 200 keV, and no bremsstrahlung macro-photon weight modification was used. Photon macro-particles were made immobile to speed up the simulation. The simulation window spanned $1176 \times 120 \times 120$ µm^3 and was split into cells of size $2.3 \times 15 \times 15$ µm^3 (using $x \times y \times z$ order), where electrons were injected through $x_{\min}$.

Bremsstrahlung X-rays within $\pm 5°$ of the angles used by Rester were grouped, and their energy distributions have been plotted in Figure 6.10. It was found that using angular

bremsstrahlung emissions made almost no difference to the angular distribution of X-rays, as elastic scatter of electrons dominated. The EPOCH results show generally good agreement with the Rester data, but EPOCH overestimates the low energy X-ray spectra, particularly in the 60° data. This benchmark was repeated in Geant4, and while full Geant4 simulations successfully reproduced the Rester data, we could also reproduce the EPOCH data when switching off attenuation from the photo-electric effect. This effect provides an energy loss mechanism for lower energy X-rays which is not included in EPOCH, explaining the deviation in this thick, high-Z target. Hence, EPOCH bremsstrahlung spectra can only be trusted for high energy X-rays, or in thin targets where X-ray attenuation is negligible.

6.6 Resistivity

In Section 5.5, we introduced the ZEPHYROS-style reduced Lee-More resistivity model which switched between the hot and cold limits of Lee-More theory [98]. The accuracy of this reduced model may be tested by comparing it to the experimental resistivity values found by Milchberg *et al* in heated aluminium targets [157].

To test the EPOCH implementation, an input deck was used in which the initial cell temperatures rose linearly in the x-direction between 0.1 K and 3.4×10^6 K (8 µeV to 300 eV). The resistivity was then calculated by the code in each cell, and this variable was output when the simulation ended. No macro-electrons were injected, and nothing changed during the short run-time of 1 fs. This benchmark tested the reduced Lee-More resistivity model in two simulations, one without any model parameter modification, and another where λ_1 and λ_2 have been changed to show better agreement with the data. The resistivity output in each cell was paired with the temperature of that cell to create the curves of Figure 6.11.

The model parameter λ_1 has the effect of causing the peak resistivity to occur at a higher electron temperature, and λ_2 changes the height of the peak. While the parametrisation allows for greater control over the low temperature side of the resistivity curve, changing λ_2 from 1 will prevent the resistivity from reproducing the high temperature limit of the full Lee-More model.

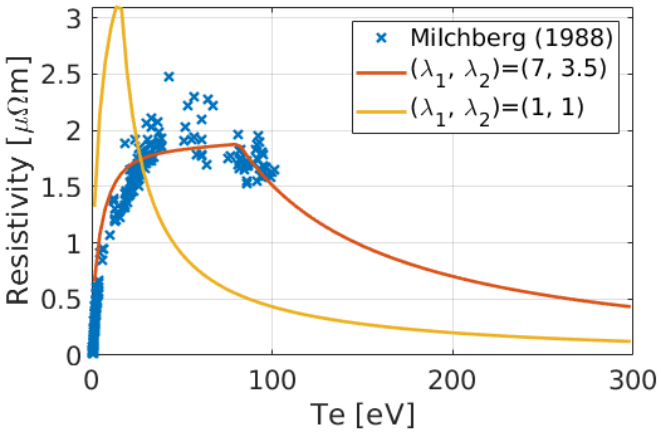

Figure 6.11: Resistivity curves using the reduced Lee-More resistivity model, plotted against the experimental Milchberg data [157]. The model parameters λ_1 and λ_2 have been varied between the two curves, one modified to overlap with the data, the other without any modification.

6.7 Ohmic heating

Ohmic heating has been neglected in the previous benchmarks, as the low current densities reached by electron beams are insufficient to generate any significant resistive fields in the target. To adequately test these routines, we must instead consider a full laser-solid interaction. A good candidate for this is the experimental work of Evans *et al* [158], which measured the temperature as a function of depth in solid targets after exposure to a high-intensity short-pulse laser. These 800 fs shots focused 300 J of laser energy into a 10 µm focal spot, corresponding to a peak intensity of around 3.1×10^{20} Wcm^{-2}. Plastic targets were used for this experiment, with a 0.2 µm Al tracer layer sandwiched at various depths in different targets for experimental temperature measurements. While we can roughly reproduce these laser parameters, we have had to make assumptions on the electron injection angle (set to 20°), and absorption efficiency (set to 4%), so we are not expecting a perfect fit to the data.

The `EPOCH` simulation set up to reproduce these results used an exponential distribution of injected electrons, with the energy dependent Moore angle (3.49) also applied. The input deck used ionisation loss with Møller scatter, but only added δ-rays over 50 keV kinetic energy to the simulation. Below this energy, the δ-ray kinetic energy was dumped to the cell for background electron heating. It is assumed that the temperatures reported by Evans *et al* [158] refer to the peak electron temperatures reached at each depth, and so the transfer

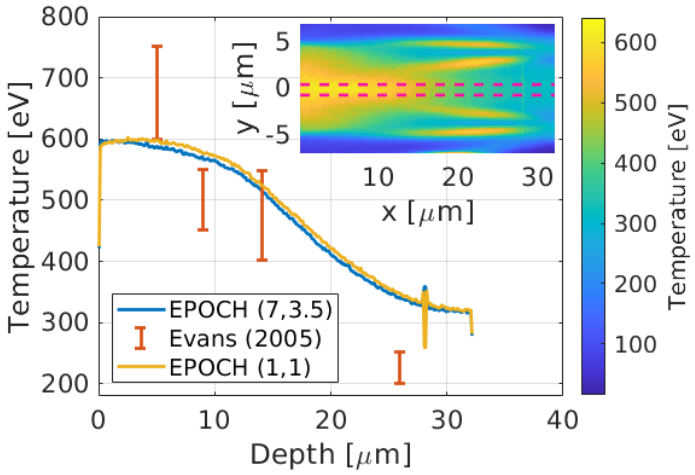

Figure 6.12: Electron temperature distributions for the CH-Al-CH target after exposure to a 800 fs laser of peak intensity $3.1{\times}10^{20}$ Wcm^{-2}. The main figure shows a line-out of the temperature averaged over the central 5×5 cells, and a heat-map of the temperature distribution is provided in the insert. This heat-map corresponds to the temperature averaged over the central 5 cells in the z direction, and the central 5 cells in y used to calculate the line-out are marked by the pink dashed lines.

of thermal energy from the electrons to the ions was not considered. Bremsstrahlung energy loss and recoil for the electrons was switched on, but no X-ray macro-particles were added to the simulation. Reflective boundaries were used for $x_{\min}$ and $x_{\max}$, and boundaries in y and z were left open. The full target in these simulations spanned 0 to 32.2 µm in x, with an Al tracer layer present between 28 µm and 28.2 µm. The simulation window was 20 µm long in y and z, and was populated with cells of size $100 \times 400 \times 400$ nm^3 ($x \times y \times z$ order). The laser temporal envelope, $g(t)$ was modelled as a 1D Gaussian with a fwhm (full width at half maximum) of $t_{fwhm} = 800$ fs, and the spatial envelope $f(r)$ at the injection point was modelled by a 2D Gaussian with fwhm $r_{fwhm} = 10$ µm. This simulation injected a total of 1.5×10^6 macro-electrons into cells with $f(r) > 0.5$ over time-steps which satisfied $g(t) > 0.1$. The temperature distribution is shown in Figure 6.12 at a 1.57 ps snapshot, where little change was found at later times. This simulation was repeated for both the default resistivity λ_1 and λ_2 values (7, 3.5), and for a run which ignored fitting parameters (1, 1).

This figure shows a fairly accurate qualitative agreement with the experimental data, given the uncertainties of the over-simplified electron injection model. The influence of the Al layer can be seen by the slight temperature change at 28 µm, which demonstrates the complex target capability of the code. It can also be seen from the heat-map that the

electron beam has broken into filaments, which is causing hot-spots to form outside the central averaging region. This creates additional uncertainty in presenting a single line-out for the temperature data.

The sensitivity of the results to the fitting parameters λ_1 and λ_2 are low, as the variants of the reduced Lee-More resistivity model used here produced very similar temperature curves. The greatest difference is seen where the Al tracer layer has been positioned, as the fitted curve shows a temperature increase, while the non-fitted curve shows both a rise and fall in temperature. This suggests a greater resolution is required to adequately measure thin complex targets.

6.8 Laser-solid bremsstrahlung emission

While Section 6.7 benchmarked Ohmic heating in a laser-solid interaction, there were no bremsstrahlung results to compare against in the paper of Evans *et al* [158]. In this section, the code attempts to benchmark the bremsstrahlung emission in laser-solid interactions by recreating the results of a similar experiment by Clarke *et al* [159]. Here, a bremsstrahlung spectrum was measured for photons travelling into a 40° forward cone, from 4×10^{20} Wcm^{-2} Vulcan shots on thick Au targets. The code modelled a 3 mm $\times 100^2$ µm^2 Au solid (cubic cells of length 0.7 µm), and ran to 12 ps. Hot electrons were injected with $t_{fwhm} = 800$ fs, $r_{fwhm} = 5$ µm, and $\eta_{l \to e} = 0.3$, using the same envelope treatment and angular distribution as in Section 6.7.

Figure 6.13 shows the number spectrum of bremsstrahlung photons created with angle less than 20° to the mean injection direction. While we expect to over-estimate the low energy bremsstrahlung emission as our code lacks photoelectric attenuation [160], we see that low energy X-rays are actually under-estimated here. Due to the success of the bremsstrahlung benchmarks in sections 6.1.4 and 6.1.5, we conclude that these discrepancies must come from the hybrid injector, and not the bremsstrahlung routines.

6.9 Summary

In general, we are capable of qualitatively reproducing relevant experimental results, and demonstrate good agreement with other simulation codes like `Geant4`. One inaccuracy revealed in these tests is the lack of the photo-electric effect, which causes `EPOCH` to overestimate

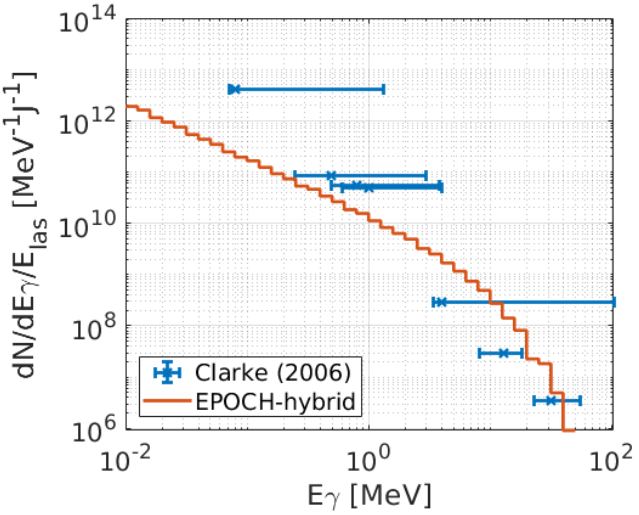

Figure 6.13: Number spectrum of X-ray photons from a 4×10^{20} Wcm^{-2} shot on a 3 mm Au target, for X-rays falling within a 40° cone (20° half-angle) about the injection direction. Experimental data is compared to an equivalent run using the hybrid-PIC code.

the X-ray spectra of low energy X-rays escaping thick targets. The code also overestimates the large-angle scattering of δ-ray emission, as we do not consider the binding energy of electrons as they are excited.

It was found that the dominant form of uncertainty when comparing to experimental results is the over-simplified hot electron injection. This could be improved by simulating the laser absorption using a PIC code, and injecting the resultant hot electron distribution into the hybrid-PIC code. However, this is still prone to uncertainty, as the pre-plasma conditions on the target surface and distribution of laser intensity over the focal spot must still be approximated. Additionally, such simulations would include high density regions, making them unsuitable for 3D full-PIC simulation of long pulses. Electron injection is a complicated issue, and instead of optimising our initial conditions to reproduce a particular experimental set-up, we will instead use a simple, consistent method for modelling our hot electron injection in this thesis.

Chapter 7

Bremsstrahlung characterisation

7.1 Introduction

As discussed in previous chapters, a high-intensity laser pulse can ionise the front surface of a solid target and form a plasma. This plasma is further heated by the laser, and a large current of high energy (hot) electrons can be injected into the solid [161]. Multipetawatt laser facilities such as ELI [23] and Apollon [24] are expected to reach intensities between 10^{22}-10^{23} Wcm^{-2}, creating hot electrons over 100 MeV in energy. Such electrons could lead to efficient X-ray generation through either synchrotron radiation in the laser focus, or through bremsstrahlung as the electrons traverse the solid. Referring back to Chapter 1, such multi-MeV X-rays could act as a source for photonuclear reactions [162], radiotherapy [163], radiography [164], or in pair production for laboratory astrophysics [165]. As X-rays are emitted in the direction of motion for ultra-relativistic particles, angular distributions may also act as a diagnostic for electron motion and divergence within the solid.

Laser-solid interactions provide a promising source for brilliant multi-MeV X-rays, but characterisation is difficult. Estimation of the conversion efficiency from hot electron energy to bremsstrahlung X-rays is complicated by competing energy loss mechanisms, shown graphically in Figure 7.1. There are five channels for hot electron energy loss in these systems: bremsstrahlung radiation, ionisation energy loss, resistive fields, reflux losses and escaping energies, all of which must be characterised separately. The escaping electron energy is sketched differently in Figure 7.1, as only the highest energy electrons were found to escape in Section 5.7. Hence, once these electrons escape, the rest remain trapped by the sheath fields and lose energy through the remaining four processes.

Figure 7.1: Visual representation of different processes simultaneously competing for the same electron energy. Labelled processes include bremsstrahlung (Br.), ionisation energy loss (Io.), resistive field losses (Fi.), reflux losses in the sheath fields (Re.) and escaping electron energy (Es.).

Previous attempts [28, 30] have been made to characterise the bremsstrahlung efficiency with full-PIC codes, but these considered the energy radiated in 36 fs and 300 fs, which are insufficient to capture a full bremsstrahlung emission. Other groups [166–169] have used Monte Carlo codes like `Geant4` [142–144] to model X-ray production in these systems, with assumed electron injection characteristics from PIC modelling or theory. While Monte Carlo codes can sample the full bremsstrahlung emission, each electron is treated independently and collective effects such as reflux losses, resistive fields and self-generated magnetic fields are neglected.

In this section, we use our hybrid-PIC code [141] to model the efficiency of hot-electron energy to bremsstrahlung X-rays over 1 MeV. While similar functionality may be achieved with the commercial hybrid-PIC code `LSP` [140] (with the exception of reflux boundaries), our code is open source with freely available documentation, which is advantageous for this kind of research. We have performed 3D (cartesian) simulations of the full bremsstrahlung emission with some collective effects, which cannot be done using traditional PIC or Monte Carlo codes. The simulation set-up is presented in Section 7.2, with bremsstrahlung characteristics reported in Section 7.3. An analysis of the hot electron motion which gives rise to these characteristics has been presented in Section 7.4. The bremsstrahlung efficiency is given in Section 7.5, and Section 7.6 provides figures and scaling laws which show how

electron energy is distributed between the five channels. In this chapter, we are interested in electron loss after injection into the solid, so we ignore X-rays produced in the laser focal spot by synchrotron emisison. A discussion of the results is present in Section 7.7.

7.2 Simulation setup

Hybrid-PIC simulations were run to model the hot electron to bremsstrahlung efficiency, $\eta_{e\to\gamma}$ for a variety of targets at different intensities. To improve statistics, the bremsstrahlung cross section was increased by a factor of 10, and macro-photon weights were reduced by the same factor to conserve real particle number. The efficiency of laser energy to hot-electron energy was set to $\eta_{l\to e} = 0.3$, and the background electron and ion temperatures were initialised at 300 K.

Hot electrons were injected into the simulation through the $x_{\min}$ boundary, with spatial and temporal envelope functions, $f(r)$ and $g(t)$ respectively. A 2D Gaussian was used for $f(r)$, characterised by a radial fwhm, $r_{fwhm} = 5$ µm. Similarly, a 1D Gaussian was used for $g(t)$, described by the fwhm, $t_{fwhm} = 800$ fs. To cut off low-weight macro-electrons, nothing was injected when $g(t) < 0.1$, or into cells with $f(r) < 0.5$. This gave a mean envelope of $\langle fg\rangle \approx 0.41$ for cells injecting electrons, with a mean root envelope $\langle\sqrt{fg}\rangle \approx 0.61$. The laser intensity was varied in the range 10^{20}-10^{22} Wcm^{-2}, and 1226 macro-electrons per time-step were injected into each cell which satisfied the envelope conditions. Macro-electrons were uniformly injected into a cone where the half angle was the smaller of 20° or the Moore angle (3.49). The empirical refluxing parameters were assigned values $\kappa_{\text{esc}} = 2$, $\kappa_{\text{tnsa}} = 2.7 \times 10^{-3}$ and $\sigma_{\langle\Delta\theta\rangle} = 23°$, based on averaged values from Table 5.4. Here we have chosen a high κ_{esc} value to closely match the C 10^{22} Wcm^{-2} simulation, as this had the most similar $\eta_{l\to e}$ out of all the sheath field characterisation runs.

The cell-size was determined by seeking convergence in the B_z field in test runs on a $10 \times 10 \times 10$ µm^3 Al target, which ran for 3.3 ps. The laser intensity was set to 4×10^{20} Wcm^{-2}, and one macro-electron was injected per cell with $f(r) > 0.5$, for each time-step when $g(t) > 0.1$. Figure 7.2 shows the B_z values averaged over all cells in the y and z directions for two cell sizes, which shows that cells of size 700 nm appear to reproduce the results of the smaller 300 nm cells. Thus, cubic cells of side length 700 nm were chosen in this simulation.

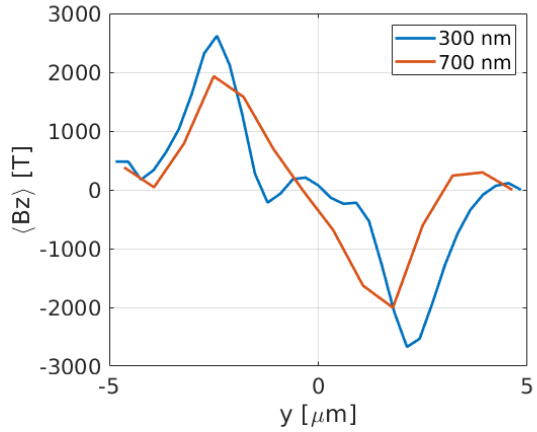

Figure 7.2: Magnetic field component B_z averaged over cells in the y and z directions for a 4×10^{20} Wcm^{-2} shot on Al, simulated by the hybrid-PIC code for two different cell sizes.

7.3 Full bremsstrahlung emission

To estimate the run-times required to capture a full bremsstrahlung emission, the X-ray characteristics were found for different targets shot by a 10^{22} Wcm^{-2} pulse. Figure 7.3 shows the rate of X-ray production for photons over 1 MeV in energy. The emission lasts on the order of 10-100 ps, with a strong dependence on target shape when using the empirical reflux boundaries, as electrons in smaller targets spend less time between reflux events and lose energy faster. The emission from lower Z targets lasts longer, as ionisation loss and bremsstrahlung have reduced stopping powers. This plot shows X-rays created within the solid and not the X-rays measured outside, as the code lacks target self-attenuation from the photoelectric effect.

The angular distribution of X-ray energy also varied with target geometry as shown in Figure 7.4, although no target reproduced the lobes observed by Vyskočil *et al* [30]. While these results do produce lobes when plotting energy per radian, $dE/d\theta$, in 3D simulations it is more appropriate to plot energy per steradian, $dE/d\Omega$ which re-weights the bins and shows a dominant emission in the forwards and backwards directions. A novel angular distribution is observed for the small foil 10×50^2 µm^3 target, which shows some emission perpendicular to the injection direction. This is because electrons deflected into a transverse direction can travel for a long time in a foil target, and emit many X-rays before hitting another boundary and scattering away. The perpendicular emission is less visible in the large foil 50 µm×1 mm^2 target as electrons experience reflux scatter less often, and so more energy is lost by

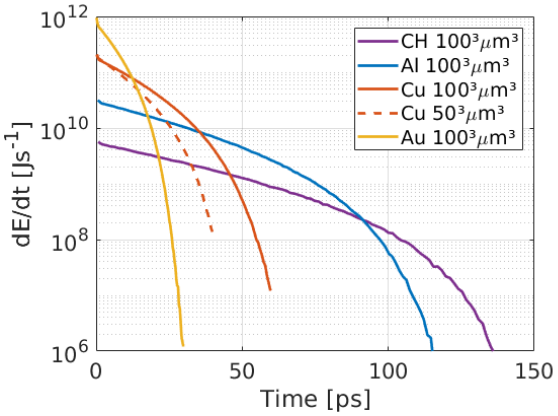

Figure 7.3: Temporal distribution of bremsstrahlung radiation from hybrid-PIC simulations, with a laser of intensity 10^{22} Wcm^{-2} on cubic targets of various compositions and sizes (labelled l^3 for side-length l).

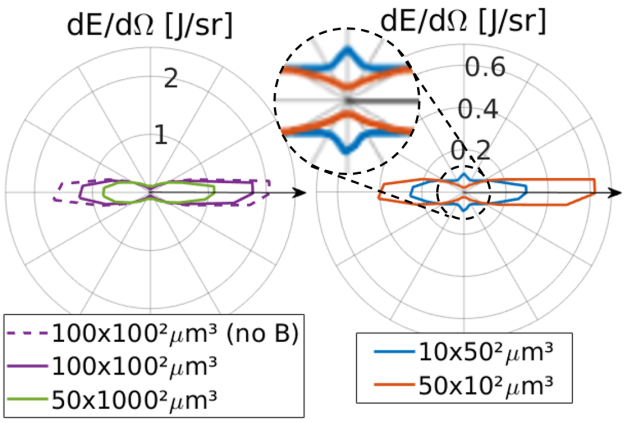

Figure 7.4: Angular distribution of bremsstrahlung radiation from hybrid-PIC simulations (10^{22} Wcm^{-2}, Cu). The injection direction is given by the arrow, and the sign of p_y determines the deviation direction for the macro-photon angles. Target dimensions are labelled as $l \times w^2$, where l is the length parallel to electron injection, and the transverse area is $w \times w$. The dashed line result refers to a test where the magnetic field was held at 0 in all cells throughout the simulation.

the time they scatter into a perpendicular direction.

Figure 7.4 also shows that magnetic B fields reduce the emission. While B fields cannot take energy from the electrons, it was found that their presence led to more energy loss by resistive fields. This suggests B fields reduce electron divergence, leading to higher current densities and stronger electric fields according to the resistive field equation (5.14).

In Figure 7.5, the bremsstrahlung energy spectra are given for some Cu targets. These spectra have a sharp gradient change at $E_\gamma \approx 86$ MeV, as the only electrons which can

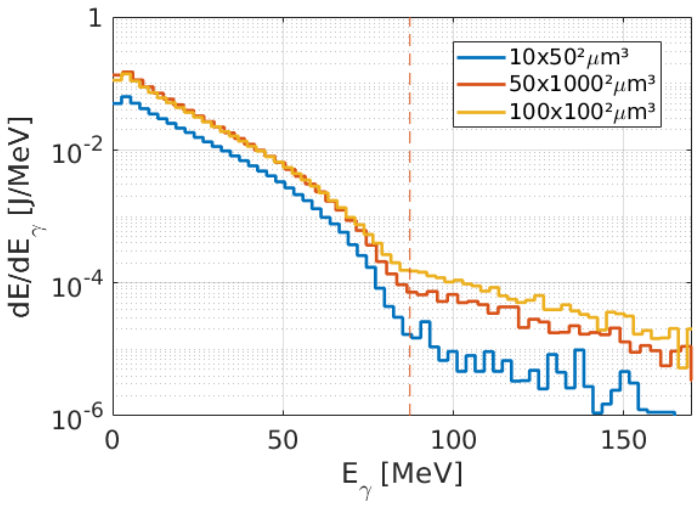

Figure 7.5: Photon energy distribution of bremsstrahlung radiation from hybrid-PIC simulations (10^{22} Wcm^{-2}, Cu). Target dimensions are labelled as in Figure 7.4. The pink line denotes the electron escape energy.

radiate above this energy escape the target after only one pass. The size of the target in x determines the length of this pass, and the energy spectra beyond 86 MeV are grouped by this size. Smaller targets produce less bremsstrahlung radiation overall, as reflux events are more common and take away a greater proportion of the hot electron energy.

To test the effects of δ-ray production on bremsstrahlung emission, the 10×50^2 µm^3 Cu target was repeated without δ-ray emission. Instead of adding δ-rays as macro-electrons which can go on to produce photons, their energy was instead dumped to the local cell as a temperature increase. The resulting spectrum showed no significant difference to the case with δ-rays, which suggests the rare high-energy photon emissions from rare high-energy δ-rays play a negligible role in the total bremsstrahlung emission.

7.4 Electron transport

The bremsstrahlung characteristics are best understood when the evolution of the hot electron population within the target is considered. To illustrate this point, additional diagnostics were performed for the simulation which modelled a 10^{22} Wcm^{-2} shot on a $100\times100\times100$ µm^3, Al target. Figure 7.6 shows snapshots of the x-component of the hot electron current density, J_x, in simulations with and without magnetic field evolution. In both cases, the electron bunch initially propagates in the laser-direction (direction of increasing x). Due to

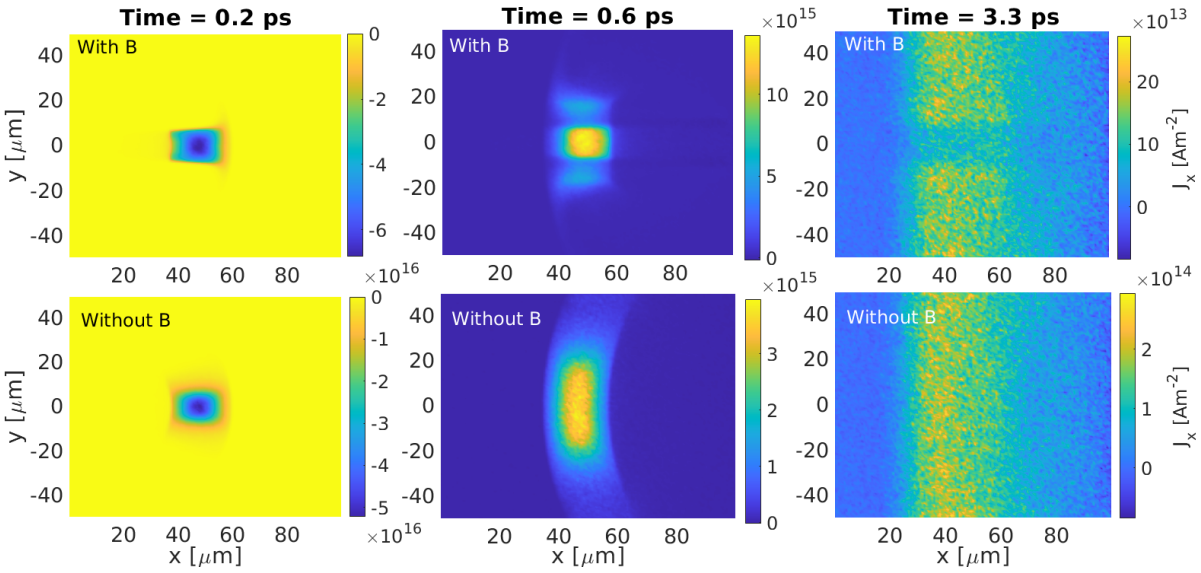

Figure 7.6: Hot electron current density J_x distributions at different snapshots from a 10^{22} Wcm^{-2} shot on Al. The top row comes from a simulation with B field evolution, and the lower has $B = 0$ in all cells. These 2D heatmaps represent J_x values averaged over the central 11 cells in the z-direction.

the high intensity laser pulse, most of the hot electrons have sufficient energy to travel at speeds close to c, and so there is little bunch dispersion in the x-direction.

As the electron bunch moves forwards, resistive fields are set up which lead to magnetic B-field generation. These B-fields are shown in Figure 7.7 for the simulation which allowed magnetic field evolution. It can be seen that in early times, the B-fields form a ring around the electron bunch position, and persist when the bunch moves on. At 0.2 ps, the effect of this B-field is to pinch the hot electron bunch, leading to a slightly higher current density in Figure 7.6 when compared to simulations with no B-fields.

Once the electron bunch reaches the rear boundary, the highest energy electrons escape and the rest reflect with some scatter. By 0.6 ps, the reflected bunch has crossed halfway along the x-direction, and the greatest difference between the B-field and no B-field simulations becomes apparent. In Figure 7.6, the 0.6 ps no-B snapshot shows a bunch spread out in the transverse direction by reflux scatter, but the B snapshot shows an electron bunch with less transverse spread and a greater current density. This is because the hot electrons have been reflected into a pre-existing B-field channel, which has not yet had time to diffuse away. These differences are clearly seen in Figure 7.8, which shows how the peak current density in the simulation window changes over time in both cases.

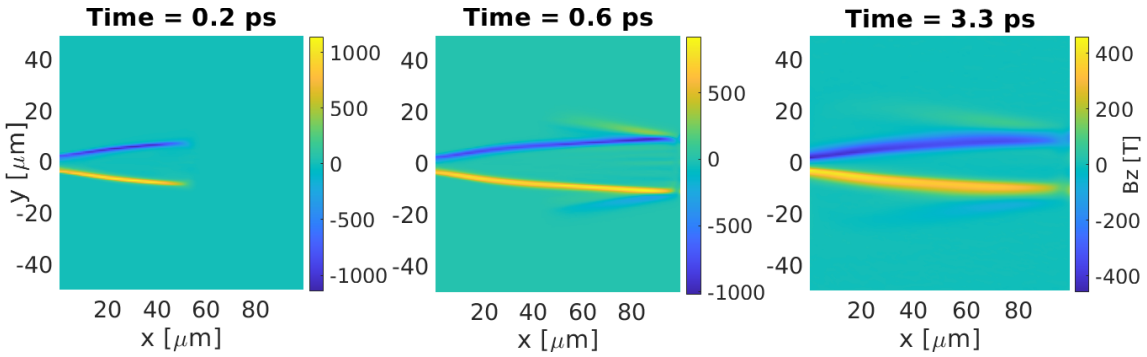

Figure 7.7: Magnetic field B_z at different snapshots, averaged over the 11 central cells in the z direction. These heatmaps correspond to the simulation in Figure 7.6 with magnetic fields enabled.

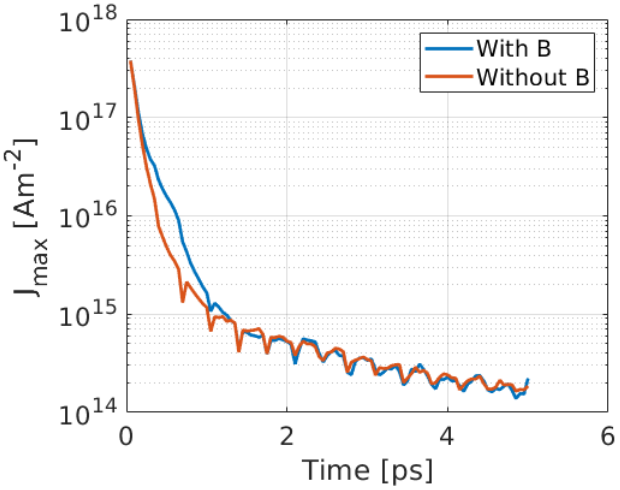

Figure 7.8: Temporal evolution of the peak current density J, from the simulations in Figure 7.6.

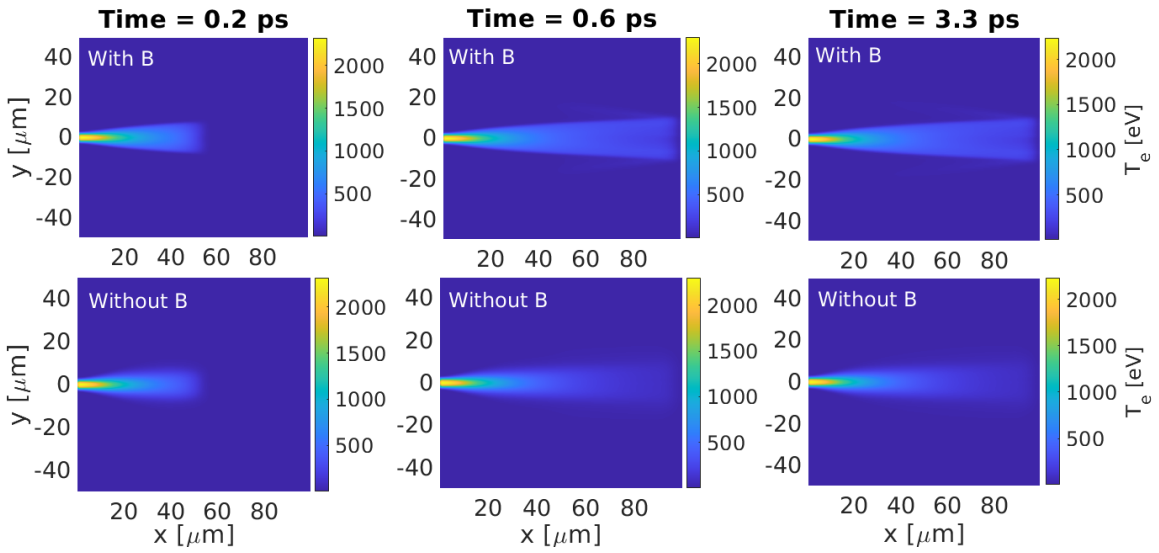

Figure 7.9: Background target electron temperature T_e distributions at different snapshots, averaged over the 11 central cells in the z direction. These heatmaps correspond to the same simulations as in Figure 7.6.

After a few more refluxes at 3.3 ps, the hot electrons have spread throughout the target, causing the current density to drop further. The resultant resistive electric fields are now much lower, and Ohmic heating becomes less important. This can be seen in Figure 7.9, which shows how the background electron temperature of the target evolves over time. Here it can be seen that heating is important in the first electron pass, but little heating occurs after this when the electrons scatter from the reflux.

As the system evolves, the differences between the B and no-B simulations becomes less apparent. With the low current densities after the first reflux, the resistive fields become much weaker, and the self-induced magnetic fields become negligible. The pre-existing B-field channel from the first pass diffuses over time, and with little to replace it, the peak magnetic field in the simulation drops. This decay has been plotted in Figure 7.10. The diffuse hot electron population then continues to scatter inside the target, and the remaining energy is lost to bremsstrahlung radiation, ionisation energy loss and reflux losses.

It can be seen that the drop in resistive fields and heating occurs much faster than the bremsstrahlnug emission, on time-scales of a few picoseconds. Despite this, these effects occur at the beginning of the simulation when the hot electron energies are highest, and during peak production of the high-energy bremsstrahlung photons. As a result, these short-lived resistive effects can influence the bremsstrahlung properties, as seen in Figure 7.4. The

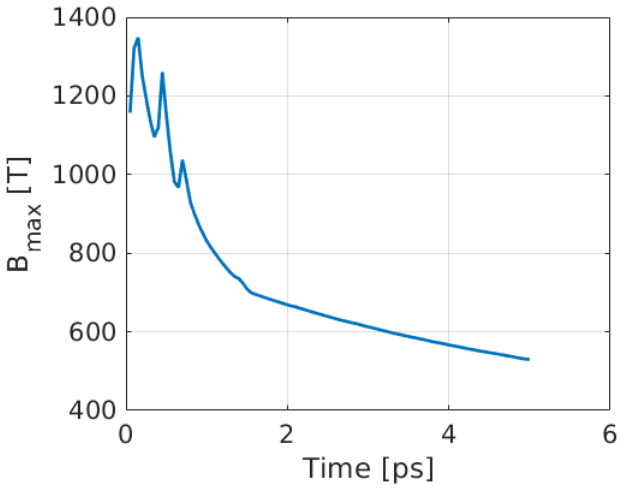

Figure 7.10: Temporal evolution of the peak magnetic field B, from the simulation in Figure 7.6 with magnetic fields enabled.

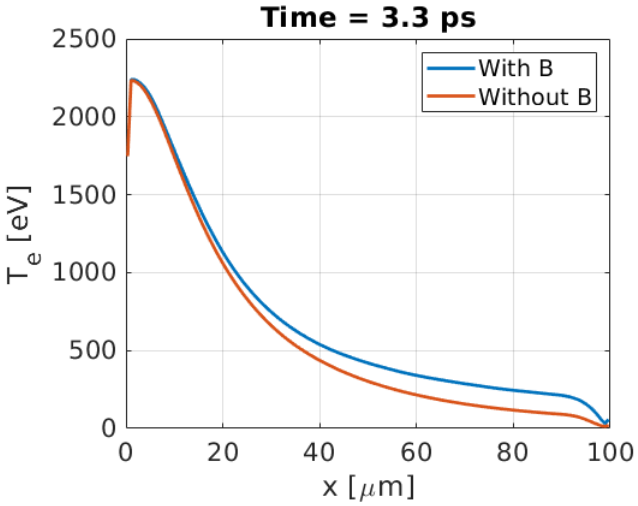

Figure 7.11: A snapshot of background target electron temperature, averaged over the central 11×11 cells in the y and z direction. These curves correspond to the simulations in Figure 7.6.

reduction of X-ray energy in B-field simulations is related to the increase in resistive energy loss, as seen by the increased background electron temperatures shown in Figure 7.11.

7.5 Efficiency scaling

There are three significant energies used when calculating efficiencies in laser-solid simulations: the total energy carried by the laser pulse (l), the sum of initial kinetic energies for

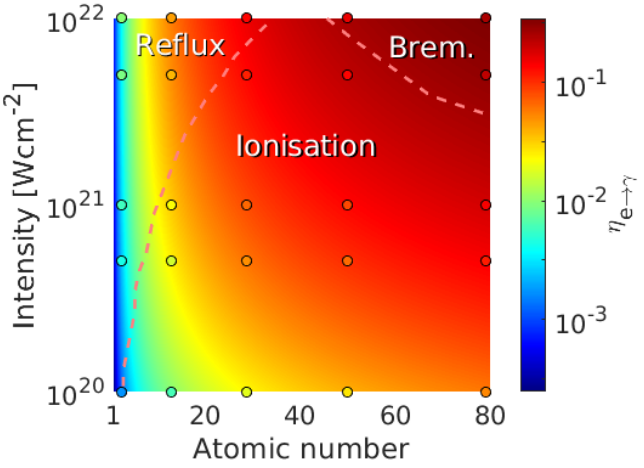

Figure 7.12: Efficiency of hot electron kinetic energy to bremsstrahlung X-rays over 1 MeV photon energy in cubic targets of side-length 100 µm. The data-points show hybrid-PIC simulations, and the background heatmap comes from a simple scaling model (see Section 7.6.1). Regions where different energy loss mechanisms dominate are split by the pink lines.

injected hot electrons (e), and the sum of X-ray energies for photons over 1 MeV (γ). The laser to X-ray efficiency $\eta_{l\to\gamma} = \eta_{l\to e}\eta_{e\to\gamma}$, and it is the electron to X-ray efficiency $\eta_{e\to\gamma}$ which is measured in these simulations.

Figure 7.12 shows $\eta_{e\to\gamma}$ evaluated for multiple $100\times100\times100$ µm^3 targets in 3D hybrid-PIC simulations. The target materials considered were Al, Cu, Sn and Au, and plastic CH targets are also shown plotted at atomic number $Z = 2.7$. The peak efficiency of hot electron energy to X-rays over 1 MeV occurs for the 10^{22} Wcm^{-2} shot on Au with $\eta_{e\to\gamma} = 0.25$, which corresponds to a laser to X-ray efficiency of $\eta_{l\to\gamma} = 0.074$.

These simulations consider the full bremsstrahlung emission, and observe efficiencies higher than those reported from full-PIC simulations. Previous estimates [28,30] for $\eta_{l\to\gamma}$ in Al targets at 10^{22} Wcm^{-2} have ranged from 4×10^{-6} to 8×10^{-5} compared to 0.014 in these simulations, although the larger target size here also contributes to the greater efficiency. The main difference between the full-PIC and our hybrid-PIC results are the time-scales. We model bremsstrahlung radiation over tens of picoseconds, whereas the PIC campaigns both simulated under 500 fs and only caught a small fraction of the total emission [28,30]. These high efficiencies are significant in experiments where bremsstrahlung is a background, suggesting measurement of X-rays from other processes (for example synchrotron radiation) may be much more difficult than currently expected.

7.6 Scaling laws

For some of the simulations present in this chapter, additional diagnostics were performed on the hot electrons as they propagated through the target. Each time-step, the energy lost by each macro-electron was tracked for each energy loss process, and so the total energy lost to each channel could be deduced. A breakdown of these energy losses is shown in Figure 7.13 for the 10^{20} and 10^{22} Wcm^{-2} simulations in 100^3 µm^3 Al and Au targets. It was found that 28% of all lost energy in the Au 10^{22} Wcm^{-2} simulation was due to bremsstrahlung radiation (from all photon energies), which dominated all other forms of energy loss. Ionisation loss dominated at 10^{20} Wcm^{-2}, taking 47% of the hot electron energy in Al and 59% in Au. Reflux energy loss dominated in 10^{22} Wcm^{-2} Al, accounting for 51% of the energy loss. Escaping energy took away 17-22% in all simulations, and resistive fields accounted for 8-19%. While some electrons gained energy from these electric fields, field gains were less than 2% of the field losses in all four simulations.

The energy loss mechanisms are also important over different time-scales. The escaping electrons leave the target after one pass, and field losses are also greatest during the initial injection when electron densities are high (around 1 ps in Figure 6.12). Bremsstrahlung, ionisation and reflux losses are important for the remainder of the electron motion, although more bremsstrahlung radiation occurs earlier when hot electron energies are high, and more ionisation loss occurs later as electron energies decrease. It was found that these results could be approximated using a simple analytic model, which is discussed in Section 7.6.1.

7.6.1 Analytic efficiency model

A simple model was constructed to quickly estimate the efficiencies of hot electron energy loss mechanisms, and to demonstrate how these scale with laser and target parameters. This model condenses the exponential injection of electron kinetic energies, ϵ_k into three macro-electrons, characterised by the high-energy X-ray threshold, ϵ_γ^{th} (1 MeV here), and the escape energy $\epsilon_{\rm esc} = \kappa_{\rm esc} a_0 m_e c^2$. The "warm" macro-electron describes all electrons with $\epsilon_k < \epsilon_\gamma^{th}$, the "emitting" macro-electron holds $\epsilon_\gamma^{th} \leq \epsilon_k < \epsilon_{\rm esc}$, and the "escaping" macro-electron holds $\epsilon_k \geq \epsilon_{\rm esc}$. The macro-electron weights are found from integrating

$$\frac{dN_e}{d\epsilon_k} = \frac{N_e}{\langle \epsilon_k \rangle} e^{-\epsilon_k / \langle \epsilon_k \rangle} \tag{7.1}$$

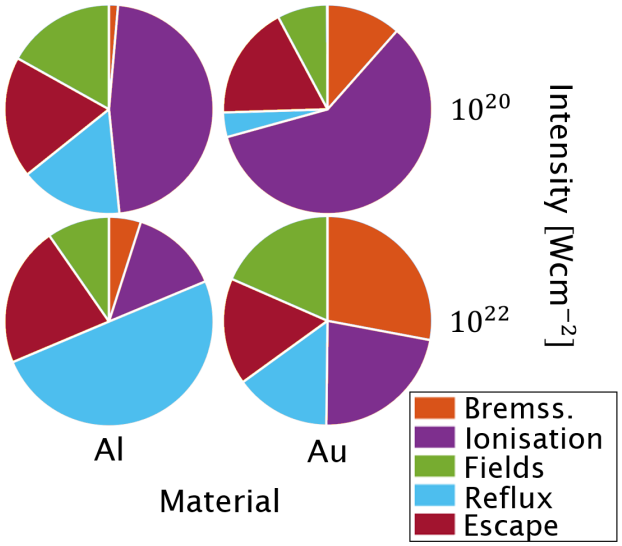

Figure 7.13: Hot electron energy loss breakdown for four hybrid-PIC simulations from Figure 7.12. The remaining electron energy in these simulations was less than 0.03% of the total energy lost over the run-time.

between the defining kinetic energy limits, where the mean injected kinetic energy $\langle \epsilon_k \rangle = a_0 m_e c^2 \langle \sqrt{fg} \rangle$. Using the hybrid particle injector model (5.7), the total number of injected electrons is

$$N_e = \frac{I_0 \langle fg \rangle \left(\frac{\pi r_{fwhm}^2}{4} \right) \left(t_{fwhm} \sqrt{\frac{\ln 10}{\ln 2}} \right) \eta_{l \to e}}{\langle \epsilon_k \rangle} \tag{7.2}$$

after substitution of the full injection area and pulse duration for our envelopes. Similarly, the three macro-electron ϵ_k values are found from integrating $\epsilon_k dN_e/d\epsilon_k$ between the defining energies.

Four stopping-powers are used to characterise energy loss from the individual energy loss mechanisms. For bremsstrahlung, a stopping power is derived from the classical radiation differential cross section for atomic targets (2.32), which takes the form

$$-\left.\frac{d\epsilon}{dx}\right|_{brem} = \frac{\gamma e^6}{12\pi^3 \epsilon_0^3 m_e c^3 \hbar} n_i Z^2 \ln\left(\frac{5.6\pi\epsilon_0 \hbar c}{Z^{1/3} e^2} \right) \tag{7.3}$$

and describes bremsstrahlung emission into photons of all energies. The stopping power from

photons over energy ϵ_γ^{th} is

$$-\left.\frac{d\epsilon}{dx}\right|_{\epsilon_\gamma>\epsilon_\gamma^{th}} = -\left.\frac{d\epsilon}{dx}\right|_{brem}\left(\frac{\epsilon_k-\epsilon_\gamma^{th}}{\epsilon_k}\right) \tag{7.4}$$

which can be used to calculate $\eta_{e\to\gamma}$. Another continuous-slowing-down approximation has been used to describe ionisation energy loss

$$-\left.\frac{d\epsilon}{dx}\right|_{ion} = \frac{Zn_ie^4}{4\pi\epsilon_0^2 m_e v^2}\left(\ln\left(\frac{\epsilon_k}{I_{ex}}\right)+\frac{1}{2}\ln(\gamma+1)+\frac{0.909}{\gamma^2}-\frac{0.818}{\gamma}-0.246\right) \tag{7.5}$$

which is given by Davies *et al* [109]. Equation (7.5) is similar to the continuous model in (3.68), but extended to δ-rays of all energy and with an approximate density correction factor. A simple continuous stopping power for reflux energy loss can be made by substituting parameters into our empirical model. In a target of size $L_x \times L_y \times L_z$, the typical path between two boundaries is roughly $(L_x + L_y + L_z)/3$, and with a known energy lost per reflux, a stopping power of the form

$$-\left.\frac{d\epsilon}{dx}\right|_{tnsa} = \frac{3\kappa_{\text{tnsa}} a_0 m_e c^2}{L_x+L_y+L_z}. \tag{7.6}$$

may be assumed. This approximation is most applicable to small targets with many reflux events, and would be a poor model in targets where electrons never reach a boundary. For fields, the stopping power is equivalent to the Lorentz force $-eE$, where the electric fields in this system are described in (5.14). Assuming the hot electron current density, j_h is balanced by the background electron current, the stopping power may be written as $-e\eta_r j_h$ for a solid with resistivity, η_r. By approximating a suitable form for $j_h(x)$, we have

$$-\left.\frac{d\epsilon}{dx}\right|_{field} = e^2\langle\eta_r\rangle\frac{I_0\langle fg\rangle\left(\frac{1}{2}r_{fwhm}\right)^2\eta_{l\to e}}{(x\tan\theta_c+\frac{1}{2}r_{fwhm})^2\langle\epsilon_k\rangle} \tag{7.7}$$

where a constant typical resistivity $\langle\eta_r\rangle$ has been used. Here we have assumed the injected current begins with a circular area of radius $r_{fwhm}/2$, where electrons move into a cone of half-angle θ_c, such that the current radius at x includes the $x\tan\theta_c$ term. This ensures the field stopping power diminishes as electrons spread out in the solid.

The "warm" and "emitting" macro-electrons are integrated through these stopping powers until they have no more energy, and the "escaping" macro-electron is integrated to

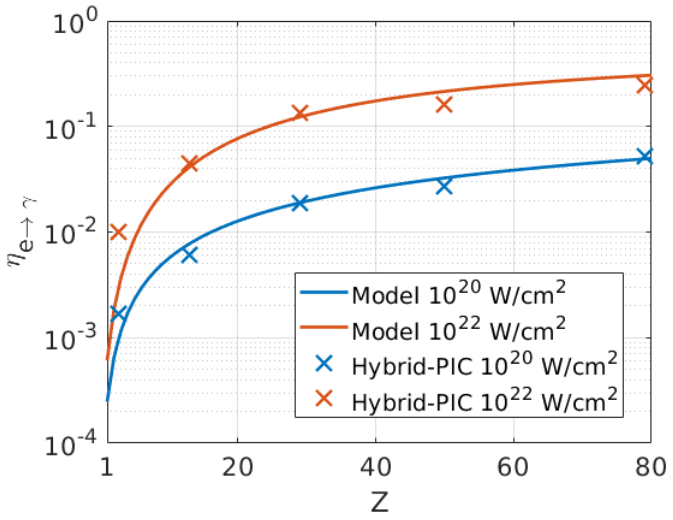

Figure 7.14: Electron to X-ray efficiency line-outs from Figure 7.12 at constant laser-intensity. The hybrid-PIC data is compared to the results from the simple analytic scaling model.

$x = L_x$, at which point the remaining energy is considered to be escaped. Using $\theta_c = 20°$ and $\langle \eta_r \rangle = 10^{-6}$ Ωm, $\eta_{e\to\gamma}$ was calculated over the simulation range shown in Figure 7.12, and forms the background heatmap. While calculating this heatmap, a constant $n_i = 6\times10^{28}$ m^{-3} was used, along with the approximation $I_{ex} \approx 11eZ$. The dominant emission mechanisms were identified in each calculation, and are grouped by the pink lines in Figure 7.12. This simple analytic model shows good agreement with the simulation results, as can be seen more clearly in Figure 7.14, where line-outs of $\eta_{e\to\gamma}$ from Figure 7.12 at fixed intensities have been plotted.

7.7 Discussion

Using a hybrid-PIC code specially developed for tracking X-ray production in laser-solid interactions, it has been found that the laser to X-ray efficiencies from bremsstrahlung radiation may be significantly higher than was previously thought. Through benchmarking the code against Vulcan shots at 10^{20} Wcm^{-2} in sections 6.7 and 6.8, the hot electron injection was found to form the dominant source of uncertainty. PIC simulations were shown to underestimate the bremsstrahlung efficiency by orders of magnitude, as they are unable to capture the full emission. Monte Carlo codes are expected to overestimate the emission, as they lack collective energy loss mechanisms. In these 3D simulations, we did not ob-

serve the lobes in the bremsstrahlung angular distribution found in 2D full-PIC simulations. Our results instead reveal a novel angular distribution for radiation, where X-rays may be strongly emitted in directions perpendicular to the laser injection direction for thin foil targets. Previous PIC campaigns may have missed this due to using spatial simulation windows which were too small in the transverse directions, and the use of outflow boundaries may have removed perpendicularly propagating electrons before significant photon emission [30]. These results also demonstrate the importance of self-induced magnetic fields, which are shown to reduce hot electron divergence, increase the resistive fields, and ultimately reduce the bremsstrahlung emission.

Different energy-loss mechanisms were found to dominate at different laser intensities and target atomic numbers, with bremsstrahlung dominating in high-intensity high-Z set-ups. A simple analytic model was provided for estimating efficiencies $\eta_{e\to\gamma}$, and good agreement was found when comparing against the predictions of the hybrid-PIC simulations. For high Z targets at lower intensities, the injected hot electrons were at lower energies and it was found that ionisation loss dominated over bremsstrahlung. In lower Z targets, the stopping power associated with these processes decreases and reflux energy loss becomes the dominant process, making these set-ups especially unsuitable for modelling using traditional Monte Carlo codes which lack collective effects.

These results rely on an empirical treatment for electron refluxing, which has some uncertainties. For instance, we have used a typical κ_{tnsa} value of 2.7×10^{-3}, but this parameter varied between $(1.2-4.2)\times10^{-3}$ in Table 5.4. To demonstrate the effect of this uncertainty, the simple scaling model was re-run over the Figure 7.12 parameter range, and the lines splitting regions of different dominant energy loss mechanisms have been recalculated in Figure 7.15 for various κ_{tnsa} values. While there is some uncertainty in the ionisation/reflux boundary, there still seems to be a region where reflux loss dominates, which would be unsuitable for modelling with Monte Carlo simulations. The κ_{tnsa} value was also varied in the simple scaling model to estimate uncertainties in the $\eta_{l\to\gamma}$ results from the 10^{22} Wcm^{-2} hybrid-PIC simulations. These efficiencies were found to be $\eta_{l\to\gamma}=(1.4\pm0.7)\%$ for Al, and $(7.4\pm1.0)\%$ for Au.

At these time-scales (over 10 ps), the code could be improved by evolving the immobile background ion fluid with a hydrodynamic code to model decompression, and the target temperatures could be diffused by a thermal conductivity model. Lower laser intensities

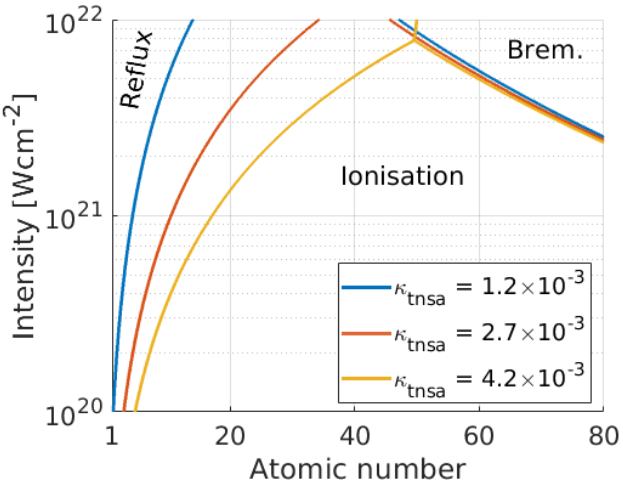

Figure 7.15: Separation lines for dominant energy loss mechanisms using the simple scaling model. These are calculated in the same way as in 7.12, but with different κ_{tnsa} values.

could be better modelled if the code was extended to include photon transport effects like photoelectric attenuation, to address the uncertainties revealed in Figure 6.10. For higher laser intensities, pair production through the Bethe-Heitler process [41] would be needed to model the propagation of high energy photons produced from hot electrons.

Chapter 8

Signatures of synchrotron radiation

8.1 Introduction

The results of Chapter 7 characterised bremsstrahlung radiation in laser-solid interactions for petawatt-class lasers, and ignored the synchrotron radiation which occurs as electrons are expelled from the laser focal spot. This treatment can be justified at low intensities, as bremsstrahlung radiation is the dominant source of X-rays in these interactions [28, 31]. However, as laser intensity increases it is expected that the efficiency of synchrotron radiation will rise faster than that of bremsstrahlung, with synchrotron eventually becoming the dominant emission process [29]. Such results are especially relevant as experimental campaigns move to multi-petawatt laser-pulses, where intensities exceeding 10^{22} Wcm^{-2} may be achieved. Some groups predict synchrotron laser-to-X-ray efficiencies on the order of 10%, for generated X-rays over 1 GeV in energy [170, 171], with others finding laser absorption over 90% [172]. The high energy electrons produced in these laser-solid interactions could radiate X-rays of high enough energy to create dense pair plasmas, or beams of exotic particles. Hence, a detailed understanding of synchrotron radiation would be required to make full use of these next generation lasers for X-ray sources.

The term responsible for the efficiency of the synchrotron emission process is η, which was defined in equation (2.52). The η parameter varies with the electromagnetic fields and the electron momentum, but the value is heavily influenced by the momentum direction relative to the fields. For example, in the case of electron refluxing, the electron oscillates back and forth in the target due to strong $\boldsymbol{E}$ fields on the boundaries (with negligible $\boldsymbol{B}$). Despite the

acceleration in strong fields, $\boldsymbol{p}$ moves parallel and anti-parallel to $\boldsymbol{E}$ in this set-up, and

$$\eta^2 \approx \frac{1}{E_s^2}\left(\gamma E^2 - \frac{E^2 p^2}{m_e^2 c^2}\right) = 0 \tag{8.1}$$

which produces very little synchrotron radiation. Conversely, electrons travelling into a counter-propagating laser beam experience perpendicular $\boldsymbol{E}$ and $\boldsymbol{B}$ such that $\boldsymbol{p} \times c\boldsymbol{B} \approx p\boldsymbol{E}$, resulting in

$$\eta^2 \approx \frac{4\gamma^2 E^2}{E_s^2} \tag{8.2}$$

and synchrotron radiation which increases with the laser intensity and electron momentum.

Several models have been developed to describe the synchrotron emission in laser-solid interactions, with the exact mechanism changing with different set-ups. For targets near relativistic critical density, electrons may be ionised and pushed away from their ions in the laser direction, creating a longitudinal space-charge electric field. Eventually this field can be strong enough to pull electrons back, and these radiate strongly as they counter-propagate with the laser. As electrons are injected into the next laser front, this process is termed re-injected electron synchrotron emission (RESE) [32]. A similar phenomenon has been observed in simulations with over-dense targets, where this time it is the laser-pulse which has its direction reversed as it reflects off the solid boundary. Forwards propagating electrons collide with the reflected laser in the process of skin-depth emission (SDE), although this creates X-rays less efficiently than the RESE mechanism as electrons are accelerated over a short distance, and the reflected laser intensity is weak [173, 174]. A third process, transversely oscillating electron synchrotron emission (TOEE), has been shown to occur for intermediate target parameters where the force from the laser balances the space-charge force [174]. Electrons can also counter-propagate with the laser after refluxing through the target rear [29], or in transverse oscillations on the edge of a laser channel (termed "edge-glow") [173].

With all these channels available to achieve prolific X-ray generation, various groups have studied ways to optimise this emission [29, 32, 170, 171, 173–180]. Target enhancements have been considered to boost the synchrotron efficiency, including nano-wire arrays to improve laser absorption [176], concave targets to enhance the laser intensity [178], and sinusoidally "bumpy" targets to set up radiating plasma waves [179]. Specially tailored pre-plasma may

provide a good target density for the laser pulse to interact with, and optimal pre-plasma scale lengths have been reported between $4-20$ µm [170,175,177]. Some groups have focused on comparisons between synchrotron emission and bremsstrahlung [28,31,180], although the PIC methods were only run over short time-scales [28, 180], and the work of Pandit [31] used a reduced radiation transport solver for bremsstrahlung which misses some energy-loss channels.

Previous literature has relied on simulations which may not fully capture the extent of the bremsstrahlung background. In this chapter we seek to re-evaluate this problem. A more detailed analytic model for RESE-based synchrotron emission is considered in Section 8.2, and the hybrid-PIC code has been used to estimate the bremsstrahlung background in Section 8.3. A final discussion of the results is also included in Section 8.4.

8.2 Re-injected electron synchrotron emission

The RESE process was first proposed by Brady *et al* [32], and is based on observations from laser-solid PIC simulations for near-critical density targets. When plotting the evolution of the electron phase-space, it was seen that electrons were initially pushed forwards by the laser and formed a dense electron bunch. After some time had passed, the bunch breaks up and some electrons reverse direction back into the laser. This breakdown event is linked to an emission of X-rays also travelling back towards the laser, and it is this collective motion which was termed RESE.

The authors present a simple analytic model to deduce the laser to X-ray efficiency of this process. Firstly, the ion motion was assumed to be negligible, and the attraction from these static ions was used to explain the electron reversal. Using a 1D geometry, the electric field established by a forwards-travelling electron bunch moving at speed c grows as

$$E_x(t) \approx \frac{n_e e c t}{\epsilon_0} \tag{8.3}$$

using Gauss' law (2.1). Eventually, the electric field on the electron bunch due to the ions will compete with the electric field of driving laser, E_0, and electron reversal may occur for $E_x = E_0$. From re-arranging (8.3), this electron bunch breakdown time τ_{bd} can be estimated

as

$$\tau_{bd} = \frac{\epsilon_0 E_0}{c e n_e} \tag{8.4}$$

and it is assumed the electrons are pulled back into the next laser peak. The laser-pulse then proceeds deeper into the target, forming a new electron bunch at the laser front which will travel until the next break-down event. The X-ray energy radiated in these periodic emissions can be approximated using the head-on collision η parameter from (8.2), with the equation for the Landau-Lifshitz force, F_{LL} (2.51). Here, the radiation power, $P_s(\eta)$ from a single electron of velocity, $\boldsymbol{v}$ would be $\boldsymbol{F}_{LL} \cdot \boldsymbol{v}$, or

$$P_s(\eta) = \frac{e^2 m_e^2 c^2}{6\pi\epsilon_0 \hbar^2} \eta^2 g(\eta) \tag{8.5}$$

for $v \approx c$. This power also includes the Gaunt factor, $g(\eta)$ from (2.71) to account for quantum effects. The number of electrons in the electron bunch, N is calculated from the size of the ion volume left behind, $N = n_e A c \tau_{bd}$ for a laser of transverse area, A. Assuming the electron bunch counter-propagates at speed c and travels one full laser wavelength during the breakdown, the emission time would be half the laser period τ_p. Thus, the efficiency of a single breakdown event is

$$\eta_{l\to\gamma} = \frac{N P_s(\eta) \tau_p}{2\epsilon_l} \tag{8.6}$$

for a laser pulse of energy ϵ_l.

When creating this analytic model for the RESE efficiency, Brady *et al* find good agreement to the data after applying a scaling factor of 0.6, and assuming there are τ_l/τ_{bd} breakdown events for a laser of pulse duration τ_l [32]. There is some ambiguity surrounding the latter condition here, which implies the breakdown events are periodic and last only as long as the laser is running. This seems to contradict the earlier description of a laser propagating through the target, forming new electron bunches at the laser front when previous bunches are re-injected downstream. In such a set-up, the laser will always find new electrons at the laser front, and the number of bunches would be set by the size of the target and not the pulse duration. Alternatively, if the re-injected electrons re-neutralised the entire ion channel and the laser energy in this channel was absorbed, then we may expect τ_l/τ_{bd} breakdowns as the

target would return to its original state after each event (although the electron temperature would be higher due to laser absorption). However, in this alternate set-up, some electrons would travel further than others and the laser to X-ray efficiency of each breakdown would not be described by equation (8.6). Hence, it is clear that while the estimates of Brady *et al* provide good scaling agreement, it may not accurately describe the temporal emission behaviour. In the remainder of this section, we describe a simple framework for modelling electron motion in RESE regimes, and compare these results to 1D full-PIC simulations.

8.2.1 Single particle model

To study the dynamics of electron motion due to acceleration from laser fields in relativistically transparent targets, we may use a model proposed in an unpublished report by Arefiev. In this section we will re-derive these equations, but while Arefiev only considered linearly polarised laser pulses, we shall keep our treatment in terms of a general vector potential, $\boldsymbol{A}$ which may have the form given in (3.38).

The derivation proceeds using Lagrangian dynamics, with a canonical momentum, $\boldsymbol{P}$ and a Hamiltonian H such that

$$\boldsymbol{P} = \boldsymbol{p} - e\boldsymbol{A} \tag{8.7}$$

$$H = c\sqrt{m_e^2 c^2 + (\boldsymbol{P} + e\boldsymbol{A})^2} - e\phi \tag{8.8}$$

for an electron of momentum $\boldsymbol{p}$ under the influence of a scalar potential ϕ. If the laser propagates in the x direction, and ϕ is assumed to be a function of x only, then P_y and P_z must be constant according to Hamilton's equations:

$$-\frac{\partial H}{\partial \boldsymbol{x}} = \frac{d\boldsymbol{P}}{dt} \tag{8.9}$$

$$\frac{\partial H}{\partial \boldsymbol{P}} = \frac{d\boldsymbol{x}}{dt} \tag{8.10}$$

and so the canonical momenta can be shown to give

$$\frac{dP_x}{dt} = -\frac{e}{\gamma m_e}(\boldsymbol{P} + e\boldsymbol{A}) \cdot \frac{\partial \boldsymbol{A}}{\partial z} + e\frac{\partial \phi}{\partial z} \tag{8.11}$$

$$\frac{dP_y}{dt} = 0 \tag{8.12}$$

$$\frac{dP_z}{dt} = 0 \tag{8.13}$$

using (8.9). Similarly, the particle position evolves according to

$$\frac{d\boldsymbol{x}}{dt} = \frac{1}{\gamma m_e}(\boldsymbol{P} + e\boldsymbol{A}) \tag{8.14}$$

which can be derived from either (8.7) or (8.10). The Landau-Lifshitz force can be added into these equations of motion, which we write as $\boldsymbol{F}_{LL} = -P_s(\eta)\hat{\boldsymbol{n}}/c$, where the unit vector, $\hat{\boldsymbol{n}}$ is

$$\hat{\boldsymbol{n}} = \frac{\boldsymbol{P} + e\boldsymbol{A}}{\sqrt{\gamma^2 - 1} m_e c} \tag{8.15}$$

as this force acts in the opposite direction to the electron momentum. Finally, the scalar potential gradient is taken to be

$$\frac{\partial \phi}{\partial x} = \frac{-Z^* e}{\epsilon_0} \int_{x_0}^{x} n_i(x')dx' \tag{8.16}$$

which comes from Gauss' law (2.1) and the ϕ definition (2.6) for ions of charge state Z^* and number density n_i. Here the electron starts at position x_0, and it is assumed that electrons do not overtake each other, and that ions are immobile. Combining all results yields the equations of motion

$$\frac{dP_x}{dt} = -\frac{e}{\gamma m_e}(\boldsymbol{P} + e\boldsymbol{A}) \cdot \frac{\partial \boldsymbol{A}}{\partial z} - \frac{Z^* e^2}{\epsilon_0} \int_{x_0}^{x} n_i(x')dx' - \frac{Px}{\sqrt{\gamma^2 - 1} m_e c^2} P_s(\eta) \tag{8.17}$$

$$\frac{dP_y}{dt} = -\frac{Py + eA_y}{\sqrt{\gamma^2 - 1} m_e c^2} P_s(\eta) \tag{8.18}$$

$$\frac{dP_z}{dt} = -\frac{Pz + eA_z}{\sqrt{\gamma^2 - 1} m_e c^2} P_s(\eta) \tag{8.19}$$

which can be solved using a 4th-order Runge-Kutta numerical integration method. Power can be deduced by tracking $P_s(\eta)$ over time.

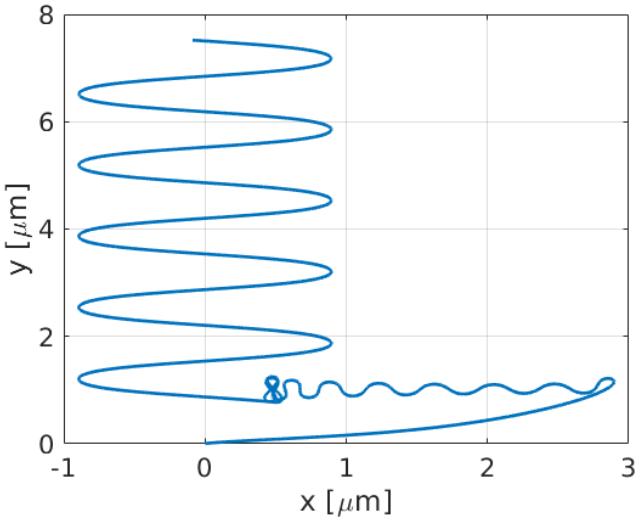

Figure 8.1: Electron trajectory in the single particle model. A laser at 2×10^{23} Wcm^{-2} intensity and 30 fs duration travels through a target of initial electron density 10^{28} m^{-3}.

An example trajectory is shown in Figure 8.1 for a linearly-polarised 30 fs step-pulse laser, with intensity $I = 2 \times 10^{23}$ Wcm^{-2}. A uniform, ionised hydrogen target with $n_i = 10^{28}$ m^{-3} was chosen to model a classically over-dense but relativistically under-dense plasma, relevant to the RESE regime. The electron shows a trajectory consistent with the RESE description, starting at (0,0) and moving with the laser at first, then falling back into the laser at $x = 2.9$ µm. The electron then oscillates around $x = 0.5$ µm where the laser push in the positive x direction is roughly balanced by the Coulomb force from the ions. Once the laser pulse ends, the Coulomb force drives oscillations in x about the start position, while the drift in y is caused by the remaining p_y at the time of the pulse end. This is a non-physical y-drift, as the simple 1D theory does not model target variation in the y direction.

8.2.2 RESE model comparisons

The single particle model can be used to calculate the electron motion and temporal distribution of synchrotron radiation when lasers strike relativistically under-dense plasma. The temporal emission from the full interaction can be estimated by summing this single electron synchrotron power over all electrons in the target, with the contributions of each electron off-set by the time taken for the laser-pulse to reach the electron start position, x_0. The synchrotron emission corresponding to the trajectory in Figure 8.1 has been summed in such a way, and the resultant full emission is shown in Figure 8.2 (labelled as Aref.). In this figure,

the laser reaches the first electron at a time $t = 17$ fs, corresponding to a 5 µm vacuum gap between the initial laser pulse-front and the plasma.

It was found that the synchrotron power radiated by the electrons was comparable to the energy carried by the 30 fs laser pulse, ϵ_l, and so a simple modified model was created using energy conservation arguments. The curve in Figure 8.2 labelled Aref. Mod. was calculated with the same method used to obtain the Aref. result, but the power at time t was reduced by the fraction, $f_s(t)$ where

$$f_s(t) = 1 - \frac{1}{\epsilon_l} \int_0^t P(t')dt' \tag{8.20}$$

and $P(t)$ is the radiated power of all electrons. Here we assume X-ray energy is drawn from the laser fields, and so there will be less laser energy available for future electron acceleration. The factor $f_s(t)$ ensures that the power radiated by subsequent electron motion is reduced by the same factor as the lost laser energy fraction at time t.

Both Aref. and Aref. Mod. show a fast rise in synchrotron power followed by a steady emission, which is in sharp contrast to the periodic breakdown model of Brady *et al* in Section 8.2. The breakdown time and re-injection energy were calculated using the same model parameters as in the single particle simulations, and the expected temporal distribution is also sketched in Figure 8.2 according to the Brady description.

In order to test the validity of the models, a series of 1D PIC simulations was performed in `EPOCH` for this laser-target set-up. As the Arefiev and Brady models are semi-classical in nature (classical with a Gaunt factor quantum correction), the quantum synchrotron Monte-Carlo module in `EPOCH` was replaced with a semi-classical Landau-Lifshitz drag force. In these simulations, a 2×10^{23} Wcm^{-2} laser pulse with a 30 fs step-profile travelled through a vacuum of 5 µm, then passed into a uniform electron-proton plasma with $n_i = 10^{28}$ m^{-3}. Recall that the other models have their temporal distributions off-set by 17 fs, as this allows for direct comparison with these PIC simulations. The code ran with cells of size 15 nm and used a total of 5.2×10^5 macro-particles, of which half were macro-electrons and the other half were macro-protons. Both electron and proton species started with zero temperature, as the comparison models also neglected thermal effects. The plasma length was set to 28 µm so the laser would not reach the simulation boundary by the 100 fs end-point (enough time for four RESE breakdown events). The radiated power from this PIC set-up has been

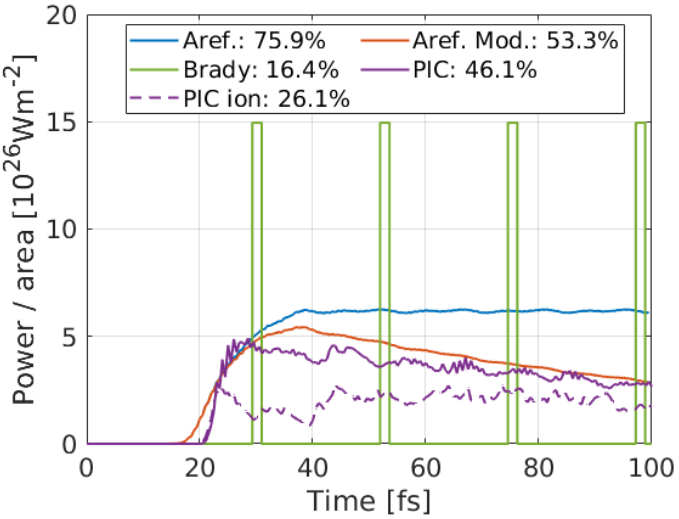

Figure 8.2: A comparison of different emission models for the RESE process. These list the Arefiev single particle model in its original (Aref.) and modified (Aref. Mod.) forms, the Brady breakdown model, and `EPOCH1D` simulations with immobile (PIC) and mobile ions (PIC ion).

simulated and plotted in Figure 8.2, both with and without ion motion.

It can be seen that the single particle model modified for energy conservation is in good agreement with the PIC simulation without ion motion. This is to be expected, as the single particle treatment is derived also assuming immobile ions. However, it can be seen that ion motion complicates this agreement, which suggests that the collective motion of particles is important for RESE radiation, and a single particle model may be of limited use (particularly for the light hydrogen ions used here). Despite this, the qualitative form of the Arefiev treatments seem in better agreement with the PIC simulations than the Brady model, as neither mobile nor immobile ion runs demonstrate the characteristic breakdown events. It is clear from these simulations that the analytic models alone cannot fully describe the synchrotron emission in laser-solid interactions, and for detailed characterisation we must turn to PIC methods.

8.3 Synchrotron and bremsstrahlung in laser-solid interactions

Experimental verification of the synchrotron emission in laser-solid interactions is complicated by the background of bremsstrahlung photons. While various groups have simulated synchrotron radiation dominating the emission at high laser intensities [28,31], these simulations were unable to capture the full bremsstrahlung emission. With the high bremsstrahlung efficiencies found in Chapter 7, it is unclear whether synchrotron radiation can still dominate at the intensities achieved by petawatt-class lasers. To test this, we performed simulations which tracked both synchrotron and bremsstrahlung photons in targets optimised for synchrotron emission and bremsstrahlung suppression.

In simulations performed by Martinez *et al* [129], it was found that synchrotron emissions dominated bremsstrahlung at high intensity (10^{22} Wcm^{-2}) and in thin targets. This is consistent with our characterisation of the bremsstrahlung emission in Chapter 7, as it was found that hot electrons in thinner targets encountered boundaries more frequently, resulting in more reflux energy loss. Parameter scans by other groups [170, 175] have found that synchrotron emission becomes more efficient when lasers interact with long pre-plasmas, with scale-lengths on the order of 10-20 µm. Thus, to find the strongest synchrotron signal in experiment, the optimal target would seem to be thin and of low atomic number to suppress bremsstrahlung, with a long pre-plasma in front. A laser intensity of 10^{22} Wcm^{-2} will be used, as this is roughly the highest intensity which can be achieved with petawatt class lasers. We will again consider a laser with a 5 µm fwhm Gaussian focal spot, and a temporal fwhm of 40 fs. The laser will be fired at a 20 µm exponentially decaying pre-plasma with scale-length 10 µm, positioned in front of a plastic foil target of dimensions $10 \times 1000 \times 1000$ µm^3. A plastic target was chosen due to the low atomic numbers of C and H, the pre-plasma length was chosen to maximise laser absorption and NCS emission, and a thin target was chosen to maximise reflux energy loss (minimising bremsstrahlung radiation). A large target transverse area was chosen in an attempt to direct the remaining bremsstrahlung radiation into a transverse direction, to allow a clearer angular signature of synchrotron radiation. The detailed simulation set-up is presented in Section 8.3.1, and the resulting hot electron and X-ray characteristics are shown in sections 8.3.2 and 8.3.3 respectively.

8.3.1 Simulation set-up

Immediately we are faced with a problem when trying to simulate both synchrotron and bremsstrahlung radiation in the same simulation. A full-PIC run can model both processes, but only in short time-scales compared to the bremsstrahlung emission. Hybrid-PIC simulations can be run for long enough to model bremsstrahlung but these codes do not model the laser, and so synchrotron emission from hot electron acceleration in the laser-fields cannot be simulated. The solution is to run both codes on the same problem. We initially start with a 2D full-PIC simulation of the target pre-plasma extending up to the solid-density surface. The laser-pulse travels through the target, and synchrotron emissions from the hot electrons are recorded upon the creation of the macro-photons. A particle probe is positioned within the solid density region to record the position, momentum, and time of each hot macro-electron passing into the solid. These macro-electrons are then injected into a 3D hybrid-PIC simulation, with the positions and momenta randomly rotated in the y-z plane by $\pm 90^\circ$ to model a 3D cone injection. The weights of the macro-electrons are multiplied by the laser fwhm to scale the 2D weights down to sensible values for 3D simulation. Once injected, the modified macro-electrons travel through the hybrid-PIC simulation as normal, and the bremsstrahlung emission is recorded.

The full-PIC simulation window spanned 26×40 µm^2, with square cells of size 20 nm. A vacuum was initialised between $-5 < x < 0$ µm, followed by a plasma of profile $n_i = n_{i0} \exp((x_{\mu m} - 20)/10)$, where $x_{\mu m}$ is the position in microns. The ion number density of the solid region, n_{i0} was 3.7×10^{28} m^{-3} for the carbon species, and 7.4×10^{28} m^{-3} for the hydrogen species. These ions were assumed to be fully ionised, and all particles were initialised at 1 keV temperature. The code used 300 particles per cell, split 1:2:6 for H:C:e^- macro-particles respectively. Beyond $x = 20$ µm, the target was initialised to solid density. Open boundaries were used for most electrons, but boundary particles starting with $|y| > 15$ µm or $x > 20.5$ µm were made to reflect off boundaries, to prevent leakage of low energy macro-particles. A particle probe positioned at $x = 20.5$ µm recorded electrons over 100 keV passing into the solid-density region. Synchrotron photons over energy 1 MeV were recorded, and bremsstrahlung was ignored in this simulation. A simulated run-time of 250 fs was used, which was sufficient for the full laser pulse to cross the entire simulation length twice (for reflection).

Electrons were injected into a hybrid-PIC simulation of size $10 \times 1000 \times 1000$ µm^3, with

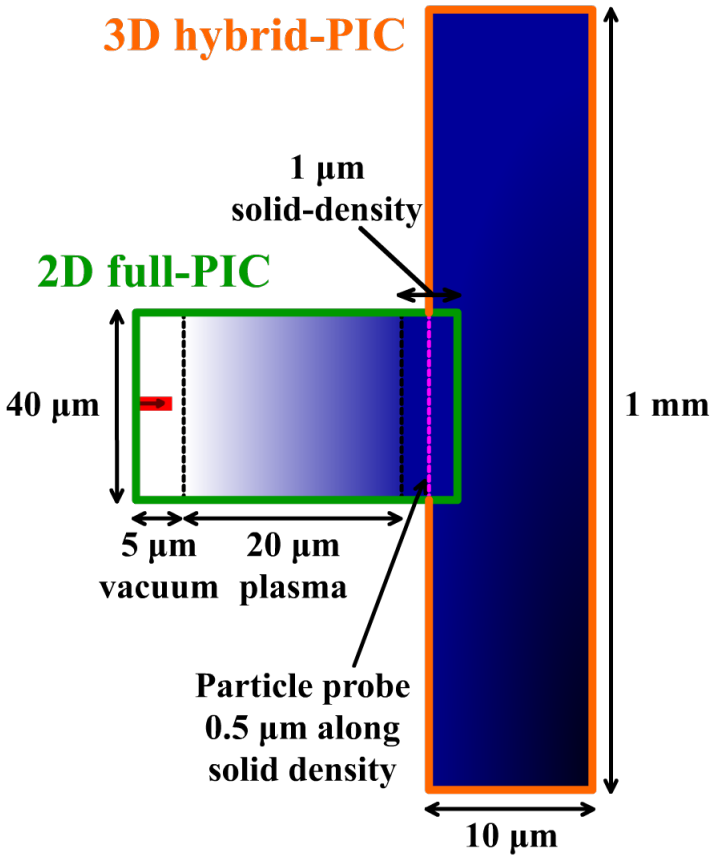

Figure 8.3: A schematic diagram sketching out the physical domains simulated by the 2D full-PIC, and 3D hybrid-PIC codes. This figure is not to scale. The laser comes in from the left hand side travelling through the pre-plasma in the full-PIC simulation, and electrons passing the particle probe are injected into the hybrid-PIC foil simulation.

cubic cells of side 0.7 µm. A plastic background was initialised, with all hybrid physics switched on. The empirical reflux parameters were set to match those of Chapter 7. The code ran for a simulated time of 125 ps, and recorded bremsstrahlung photons of energy over 1 MeV. This set-up is shown graphically in Figure 8.3.

8.3.2 Hot electron population

Before discussing the X-ray characteristics of synchrotron and bremsstrahlung radiation, it is worth inspecting the hot electron population passing the particle probe. To better describe the energies involved in 3D space, the 2D macro-particles have had their weights reduced by the factor 5×10^{-6} in the figures of this section. This scale-factor was chosen to match the fwhm of the laser focal spot, as this is expected to set the length scale of the omitted

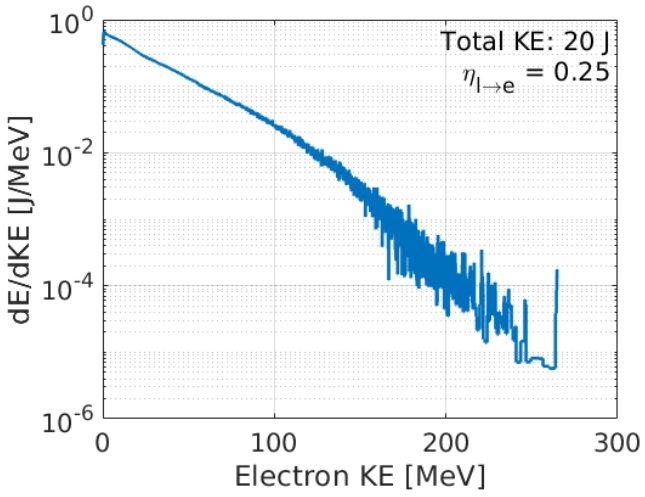

Figure 8.4: The kinetic energy spectrum of electrons passing the particle probe at the end of the PIC simulation. The total electron kinetic energy and laser to electron efficiency are also provided. Particle weights are multiplied by the laser fwhm in metres (5.0×10^{-6}) to account for 2D to 3D conversion.

dimension. The energy spectrum of electrons passing into the hybrid simulation is given in Figure 8.4. In this simulation, 80 J of laser energy was injected through the $x_{\min}$ boundary, and the particle probe recorded a total kinetic energy of 20 J from electrons over 100 keV in energy. A simple exponential fit to the data yields a hot electron temperature of 31 MeV, which is comparable to the 43 MeV temperature expected from ponderomotive scaling. The 25% laser to electron efficiency is also consistent with the injection models we have assumed so far.

The angular distribution of hot electrons at the particle probe is plotted in Figure 8.5, and shows consistency with previous estimates. In the hybrid-PIC simulations of Chapter 7, the electron distribution was also modelled as a cone between some angular cut-off limits (here 41° compared to our earlier 20°). The transverse boundaries in the PIC simulation were made to be open for electrons starting near the laser axis, so it is expected that electrons with a large injection angle may escape the simulation window before reaching the particle probe. In the worst case scenario at the front of the pre-plasma, such an electron would have to travel 20 µm in y before travelling 20.5 µm in x, suggesting a maximum cut-off angle of 45°. As 45° is greater than the observed cut-off angle, the limits of Figure 8.5 are not expected to be an artefact of the simulation window size.

We finally consider the temporal distribution of hot electron passage shown in Figure

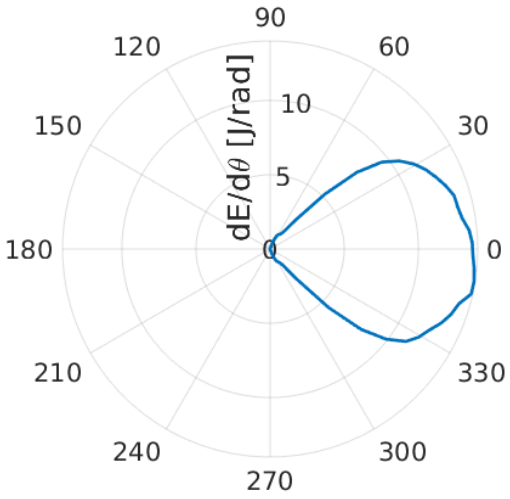

Figure 8.5: The angular distribution of electrons passing the particle probe at the end of the PIC simulation. Macro-particle weights have been adjusted as in Figure 8.4.

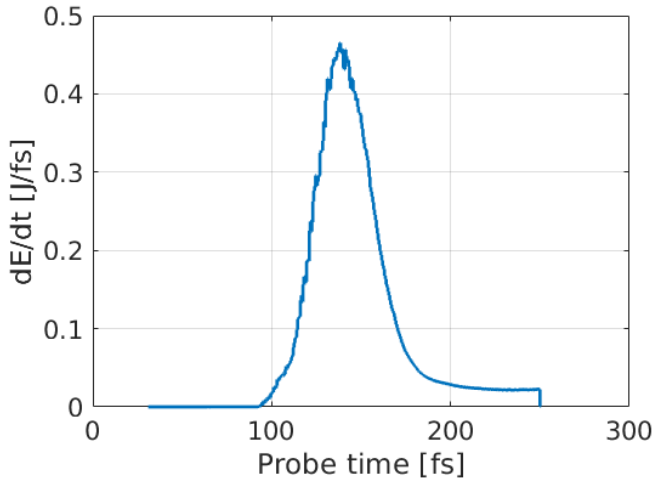

Figure 8.6: The temporal distribution of electrons passing the particle probe at the end of the PIC simulation. Macro-particle weights have been adjusted as in Figure 8.4.

8.6. The fwhm of this electron injection is measured to be 38 fs, which is consistent with the 40 fs fwhm used by the laser pulse. While the injection profile does show the characteristic rise and fall with laser intensity, there is also a high energy tail which is not fully resolved in the simulation run-time. As it takes 67 fs for an electron travelling close to c to pass our 20 µm pre-plasma, it is assumed that such a tail would not extend for much longer, as hot electrons would quickly leave the simulation window. Alternatively, these late probe events may be due to non-physical self heating of macro-electrons, which could also be ignored.

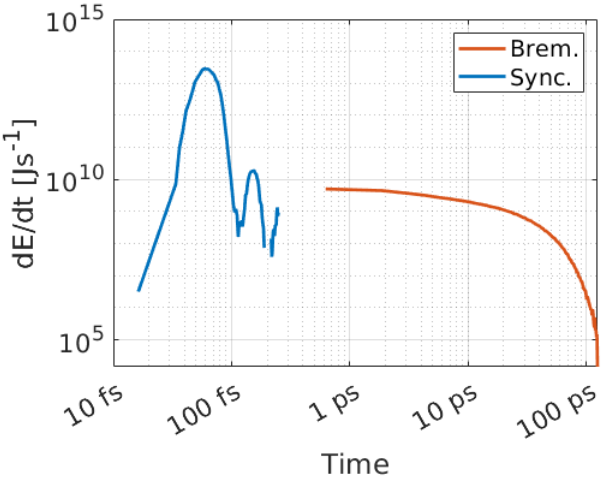

Figure 8.7: The temporal distributions of synchrotron and bremsstrahlung emissions from the full-PIC and hybrid-PIC codes respectively. Synchrotron macro-photon weights are adjusted as in Figure 8.4. The bremsstrahlung emission appears delayed as the hybrid-PIC code only writes to file 100 times, and these outputs do not resolve the femtosecond time-scale.

8.3.3 X-ray characteristics

In this simulation, it was found that synchrotron emission provided the dominant source of X-ray radiation. The $\eta_{l\to\gamma}$ value for synchrotron radiation was 0.84%, which is comparable to the $\eta_{l\to\gamma} \approx 1\%$ estimate of Brady *et al* at 10^{22} Wcm^{-2} [32]. The efficiency into bremsstrahlung radiation was found to be an order of magnitude lower, with $\eta_{l\to\gamma} = 0.083\%$. The key differences between these radiation mechanisms can be seen in Figure 8.7, which illustrates the temporal emission of the two processes. Synchrotron radiation occurs in a bright flash as it can only generate photons while interacting with the fields of the short-pulse laser, whereas bremsstrahlung radiates less power, but for a much longer time-scale (particularly in the case of plastic). The smaller peaks in the synchrotron signal are likely due to simulation noise which appears exaggerated on the log-scale. While the short time-scale flash would be a clear signature of synchrotron radiation, it is not experimentally feasible to resolve the emission of multi-MeV photons over a femtosecond time-scale.

In Figure 8.8, it can be seen that the synchrotron emission dominates that of bremsstrahlung between photon energies of 1-20 MeV. While photons will be created below this energy, these macro-photons were not added to the simulation for computational speed. Synchrotron radiation also appears to dominate at high photon energies, as the escaping hot electron population restricts the bremsstrahlung emission over 80 MeV. However, it can also be seen that the

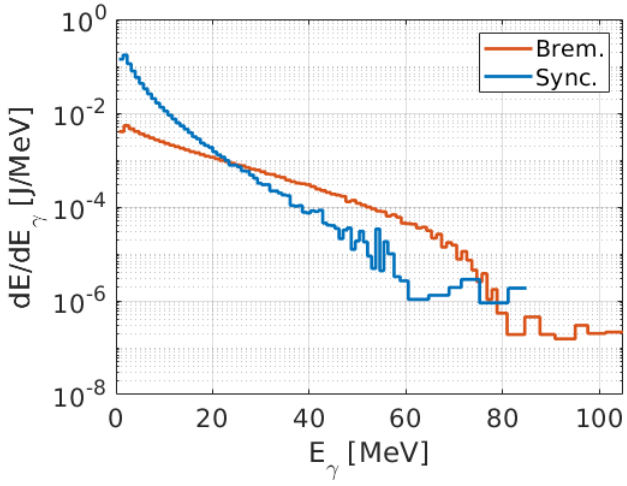

Figure 8.8: Energy spectra of synchrotron and bremsstrahlung radiation. Synchrotron macro-photon weights are adjusted as in Figure 8.4.

bins have become much wider at these high photon energies, which shows that the photon spectra are under-sampled here. Due to the poor photon statistics, the high photon-energy synchrotron domination may be an artefact of statistical noise.

Lastly, the angular distributions of synchrotron and bremsstrahlung radiation have been provided in Figure 8.9. This plot depicts $dE/d\theta$ (energy per unit radian), and so the curve integrated between two θ limits shows how much radiation would be detected by a ring of detectors catching all escaping photons with these angles. This is distinct from the $dE/d\Omega$ (energy per steradian) plots of Figure 7.4, which describe how much energy passes through a detector of constant solid-angle positioned at different θ positions. While $dE/d\Omega$ is more experimentally relevant, the choice to plot $dE/d\theta$ is justified for the synchrotron data as the photon momentum was mostly confined to the x-y plane. In the 2D full-PIC simulation, the mean $\langle|p_y|\rangle$ was 1.6 MeV/c for the synchrotron photons, compared to $\langle|p_z|\rangle = 665$ eV/c. Thus, it would be misleading to re-weight the bins to $dE/d\Omega$ assuming photons were spread out azimuthally for a given θ. Bremsstrahlung is also plotted by $dE/d\theta$ to allow direct comparison against the synchrotron signal, despite the 3D nature of the bremsstrahlung emission.

In Figure 8.9, it can be seen that bremsstrahlung is restricted to emissions in the transverse direction. Due to using a thin target with low atomic number, the bremsstrahlung stopping power is low and electrons do not lose much energy before reflux scattering. The

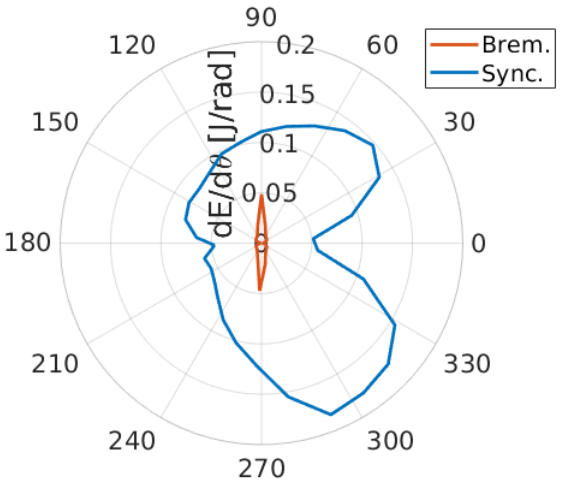

Figure 8.9: Angular distribution of synchrotron and bremsstrahlung radiation. Synchrotron macro-photon weights are adjusted as in Figure 8.4. The incident laser direction for PIC, and the electron injection direction for hybrid-PIC are both directed along θ=0.

electrons will then continue to reflux between x boundaries until they are scattered into a transverse direction, where they may travel a long distance and emit many X-rays before scattering away. This provides a more extreme example of the transverse electron travel highlighted in Figure 8.9. The synchrotron emission peaks along lobes which are directed off the laser axis in the forwards direction, alongside a non-negligible emission in the backwards direction. Such an angular distribution is consistent with the synchrotron radiation pre-plasma modelling of Vyskočil *et al* [29].

8.4 Discussion

This chapter sought to model synchrotron radiation in the laser focal spot for petawatt-class laser pulses, with a particular emphasis on near-critical density targets, and pre-plasmas passing critical density. It was found that at high intensities, it was still possible to have synchrotron radiation dominate bremsstrahlung radiation in thin, low-Z targets. Synchrotron radiation was found to be particularly dominant in lobe directions around 30° to 60° off the laser axis in the forwards direction, for X-rays of energies between 1 and 20 MeV.

While such results are a promising start, they do not represent a clear signature for synchrotron emission. Detectors cannot distinguish synchrotron photons from bremsstrahlung, and so a simple bright spot of X-rays at 40° for 1-20 MeV photons would not guarantee an

observation of synchrotron radiation. A more robust signature may be found in the X-ray scaling. In all the RESE models of Section 8.2, it was assumed that the power roughly scaled with η^2 (8.5), which scales with $\gamma^2 E^2$ when electrons collide with the laser head-on (8.2). In ponderomotive scaling, $\gamma \approx a_0$, and the laser intensity, I scales with both E^2 (3.37) and a_0^2 (3.45), hence the synchrotron power may be expected to scale with I^2. Meanwhile, the bremsstrahlung stopping power only scales with γ (7.3), and so it may be expected that bremsstrahlung is proportional to $\sqrt{I}$. Hence, a possible synchrotron signature may be found by looking at how the radiated power scales with laser intensity, performing multiple shots on targets and varying I between 10^{21} and 10^{22} Wcm^{-2}. Detectors sensitive to X-ray energies of a few MeV and positioned in a lobe direction would be most likely to record the synchrotron I^2 scaling. In such an experiment, synchrotron radiation may be 100 times weaker at 10^{21} Wcm^{-2}, so this range may include both bremsstrahlung and synchrotron scaling at low and high intensities respectively.

In practice, the scaling behaviour may be more complicated. The synchrotron scaling arguments assume a RESE-like emission, but the observed lobes in Figure 8.9 show a forwards emission component as well. Ion motion may further complicate the synchrotron scaling theory. Furthermore, the bremsstrahlung path length is not fixed - a reduction in the bremsstrahlung stopping power does not necessarily imply the same reduction in the total emitted power, as electrons may radiate the same amount of energy over a longer time. However, the reduced stopping power will give the other energy loss mechanisms more time to drain hot electron energy in non-radiative ways. As seen in Figure 7.13, ionisation loss will start to dominate at lower laser intensities, so the bremsstrahlung efficiency will still decrease with I. Further work on synchrotron signatures could look to repeat the simulations of Section 8.3 at different intensities, to explicitly model these scaling behaviours.

Chapter 9

Conclusion

The hot electrons produced when high intensity ($>10^{20}$ Wcm^{-2}) lasers strike solid targets have the potential to produce a bright source of X-rays, with photon energies in excess of 1 MeV. These X-rays are generated from both electron acceleration in the laser focal spot (synchrotron) and from acceleration in the electric fields of target nuclei (bremsstrahlung). While previous groups have sought to compare the radiation generated from these two mechanisms, the results were limited by full-PIC simulation time-scales which prevented simulation of the entire bremsstrahlung emission. A hybrid-PIC extension to the PIC code `EPOCH` has been written to achieve this simulation capability, and it was demonstrated that the bremsstrahlung emission lasted on the order of 10-100 ps, with a strong dependence on laser intensity, along with the shape and material of the target.

In benchmarking the hybrid-PIC code against experiment, it was found that one source of uncertainty appeared to be the simple model used for electron injection. This limits the results to seeking general X-ray characteristics, instead of recreating the initial conditions of a particular experimental set-up. While electron transport routines have been included, photon transport effects like photoelectric attenuation and Bethe-Heiter pair production are omitted, although these effects are less important for photons over 1 MeV at the laser intensities of interest here (see Figure 6.10). Another source of uncertainty comes from the simple empirical boundary model, which was devised to approximate the electron refluxing behaviour (reflux energy loss, scatter and escaping electrons). This boundary treatment is an improvement over traditional hybrid-PIC modelling methods which used open or reflective boundaries, but it does introduce uncertainties into the results.

In 3D hybrid-PIC simulations modelling the bremsstrahlung emission, it was found that

different energy loss mechanisms dominated the hot electron stopping power in different regimes. Bremsstrahlung radiation dominated in high intensity shots on targets with high atomic number, while ionisation energy loss dominated lower intensities. In targets of lower atomic number, electron refluxing was found to provide an important energy loss mechanism, as the low stopping powers of bremsstrahlung and ionisation loss allowed the electrons to complete more refluxes before running out of energy. Despite these competing processes, it was found that the bremsstrahlung efficiency was significantly higher than full-PIC estimates, with a laser to X-ray (>1 MeV) conversion efficiency peaking at $(7.4 \pm 1.0)\%$ for 10^{22} Wcm^{-2} shots on thick gold targets. A simple model for estimating the bremsstrahlung efficiency has also been included, and shows good agreement with the hybrid-PIC simulation data.

While the long run-times distinguish these results from those found using full-PIC codes, the inclusion of resistive fields, refluxing and self-generated magnetic fields separates the hybrid-PIC model from Monte Carlo simulations too. It was found that the combination of fields and refluxing took away a large proportion of the hot electron energy, which would not be modelled by a Monte Carlo code. The magnetic fields within the target helped to maintain a high electron beam density, which lead to further energy loss through resistive fields and Ohmic heating. The large scatter of reflux boundaries also contributed to a novel angular distribution of radiation in large foil targets. It was found that X-ray lobes emerged in the transverse direction, as electrons scattered into these directions could travel a long time before encountering another boundary and scattering away. This result relies on using both the reflux boundary model and the large spatial domain of the hybrid-PIC simulation window, which would be difficult to reproduce with full-PIC or Monte Carlo codes.

Despite the high efficiency of laser energy to bremsstrahlung radiation found in hybrid-PIC simulations, there may still be regimes accessible with petawatt class lasers where synchrotron radiation dominates. Using a combination of 2D full-PIC and 3D hybrid-PIC modelling, it was found that a 10^{22} Wcm^{-2} shot on a plastic foil target yielded a synchrotron laser-to-radiation efficiency of 0.84%. This was found to be roughly $10\times$ higher than the corresponding bremsstrahlung efficiency (0.083%). A single particle model can be used for general synchrotron scaling predictions, and seems to provide a more accurate representation of the temporal evolution of radiation through the RESE mechanism. However, this model is limited by its immobile ion approximation, as 1D full-PIC simulations demonstrate a reduction in synchrotron power when ion motion is permitted.

Further work may be performed to improve both bremsstrahlung and synchrotron radiation modelling using these codes. Including photon transport effects like Bethe-Heitler pair production will allow the propagation of high energy photons to be treated more realistically, which would be important when simulating intensities over 10^{23} Wcm^{-2} for multi-petawatt lasers. Additions to the hybrid-PIC code could also be made to model the changing nature of the target over long time-scales. The background ion number density could be updated according to a hydrodynamic model, which would describe the deformation of the target and thermal expansion. Further results could also be generated with the code in its current form. For example, by sampling the synchrotron and bremsstrahlung emissions for a variety of laser intensities and target parameters, we expect to find additional synchrotron signatures in the radiation scaling. To conclude, our hybrid-PIC code has provided new insights into the radiation produced in high intensity laser-solid interactions. With multi-petawatt lasers on the horizon, we anticipate this code leading to even more interesting results in the future.

List of References

[1] A. Filler. The history, development and impact of computed imaging in neurological diagnosis and neurosurgery: Ct, mri, and dti. *Nature Precedings*, pages 1–1, 2009.

[2] W. H. Bragg and W. L. Bragg. The reflection of x-rays by crystals. *Proceedings of the Royal Society of London. Series A, Containing Papers of a Mathematical and Physical Character*, 88(605):428, 1913.

[3] A. Ebrahim, et al. Dose-resolved serial synchrotron and xfel structures of radiation-sensitive metalloproteins. *IUCrJ*, 6(4):543, 2019.

[4] D. Allan, et al. Status of the crystallography beamlines at diamond light source. *The European Physical Journal Plus*, 130(3):1, 2015.

[5] J. Strempfer, T. Brückel, D. Hupfeld, J. Schneider, K.-D. Liss, and T. Tschentscher. The non-resonant magnetic x-ray scattering cross-section for photon energies up to 500 kev. *Europhysics Letters*, 40(5):569, 1997.

[6] N. Schell, A. King, F. Beckmann, T. Fischer, M. Müller, and A. Schreyer. The high energy materials science beamline (hems) at petra iii. In *Materials Science Forum*, volume 772, pages 57–61. Trans Tech Publications, 2014.

[7] D. I. Thwaites and J. B. Tuohy. Back to the future: the history and development of the clinical linear accelerator. *Physics in Medicine & Biology*, 51(13):R343, 2006.

[8] R. C. Runkle, D. L. Chichester, and S. J. Thompson. Rattling nucleons: New developments in active interrogation of special nuclear material. *Nuclear Instruments and Methods in Physics Research Section A: Accelerators, Spectrometers, Detectors and Associated Equipment*, 663(1):75, 2012.

[9] C. Cetina, et al. Photofission of heavy nuclei at energies up to 4 gev. *Physical Review Letters*, 84(25):5740, 2000.

[10] D. Li, K. Imasaki, and M. Aoki. Analysis on coupling gamma-ray to nuclear giant resonance. *Journal of Nuclear Science and Technology*, 39(11):1247, 2002.

[11] E. Irani, S. K. Sadighi, S. Zare, and R. Sadighi-Bonabi. Laser-induced photo transmutation of 126sn–a hazardous nuclear waste product-into short-lived nuclear medicine of 125sn. *Energy Conversion and Management*, 64:466, 2012.

[12] X.-L. Zhu, T.-P. Yu, Z.-M. Sheng, Y. Yin, I. C. E. Turcu, and A. Pukhov. Dense gev electron–positron pairs generated by lasers in near-critical-density plasmas. *Nature communications*, 7(1):1, 2016.

[13] R. Blumenthal, W. Faissler, P. Joseph, L. Lanzerotti, F. Pipkin, D. Stairs, J. Ballam, H. DeStaebler Jr, and A. Odian. Photoproduction of charged pions from beryllium in the bev range. *Physical Review Letters*, 11(11):496, 1963.

[14] P. Rogalla, C. Kloeters, and P. A. Hein. Ct technology overview: 64-slice and beyond. *Radiologic clinics of North America*, 47(1):1, 2009.

[15] R. Edwards, et al. Characterization of a gamma-ray source based on a laser-plasma accelerator with applications to radiography. *Applied Physics Letters*, 80(12):2129, 2002.

[16] J. Katz, G. Blanpied, K. Borozdin, and C. Morris. X-radiography of cargo containers. *Science & Global Security*, 15(1):49, 2007.

[17] C. Chen, et al. Bremsstrahlung and k α fluorescence measurements for inferring conversion efficiencies into fast ignition relevant hot electrons. *Physics of plasmas*, 16(8):082705, 2009.

[18] G. Sarri, et al. Ultrahigh brilliance multi-mev γ-ray beams from nonlinear relativistic thomson scattering. *Physical Review Letters*, 113(22):224801, 2014.

[19] J. Ferri, et al. High-brilliance betatron γ-ray source powered by laser-accelerated electrons. *Physical Review Letters*, 120(25):254802, 2018.

[20] C. Limborg, J. Clendenin, D. Dowell, S. Gierman, and J. Schmerge. New optimization for the lcls photo-injector. In *Proceedings of the 8th European Particle Accelerator Conference*. 2002.

[21] J. Cole, et al. Laser-wakefield accelerators as hard x-ray sources for 3d medical imaging of human bone. *Scientific Reports*, 5(1):1, 2015.

[22] C. Brenner, et al. Laser-driven x-ray and neutron source development for industrial applications of plasma accelerators. *Plasma Physics and Controlled Fusion*, 58(1):014039, 2015.

[23] S. Weber, et al. P3: An installation for high-energy density plasma physics and ultra-high intensity laser–matter interaction at eli-beamlines. *Matter and Radiation at Extremes*, 2(4):149, 2017.

[24] D. Papadopoulos, et al. First commissioning results of the apollon laser on the 1 pw beam line. In *2019 Conference on Lasers and Electro-Optics (CLEO)*, pages 1–2. IEEE, 2019.

[25] P. B. Corkum. Plasma perspective on strong field multiphoton ionization. *Physical review letters*, 71(13):1994, 1993.

[26] B. Yaakobi, I. Pelah, and J. Hoose. Preheat by fast electrons in laser-fusion experiments. *Physical Review Letters*, 37(13):836, 1976.

[27] C. B. Schroeder, E. Esarey, J. van Tilborg, and W. P. Leemans. Theory of coherent transition radiation generated at a plasma-vacuum interface. *Physical Review E*, 69(1):016501, 2004.

[28] F. Wan, C. Lv, M. Jia, H. Sang, and B. Xie. Photon emission by bremsstrahlung and nonlinear compton scattering in the interaction of ultraintense laser with plasmas. *European Physical Journal D*, 71(9):236, 2017.

[29] J. Vyskočil, E. Gelfer, and O. Klimo. Inverse compton scattering from solid targets irradiated by ultra-short laser pulses in the 1022–1023 w/cm2 regime. *Plasma Physics and Controlled Fusion*, 62(6):064002, 2020.

[30] J. Vyskočil, O. Klimo, and S. Weber. Simulations of bremsstrahlung emission in ultra-intense laser interactions with foil targets. *Plasma Physics and Controlled Fusion*, 60(5):054013, 2018.

[31] R. Pandit. *Numerical study of γ-ray production in ultra-intense laser-plasma interaction.* Ph.D. thesis, University of Nevada, Reno, 2015.

[32] C. S. Brady, C. Ridgers, T. Arber, A. Bell, and J. Kirk. Laser absorption in relativistically underdense plasmas by synchrotron radiation. *Physical Review Letters*, 109(24):245006, 2012.

[33] J. Jackson. Classical electrodynamics, 1999.

[34] B. Laud. *Electromagnetics.* Wiley Eastern, 1987.

[35] N. W. Ashcroft, N. D. Mermin, et al. Solid state physics, 1976.

[36] K. S. Thorne and R. D. Blandford. *Modern Classical Physics: Optics, Fluids, Plasmas, Elasticity, Relativity, and Statistical Physics.* Princeton University Press, 2017.

[37] H.-K. Chung, M. Chen, W. Morgan, Y. Ralchenko, and R. Lee. Flychk: Generalized population kinetics and spectral model for rapid spectroscopic analysis for all elements. *High Energy Density Physics*, 1(1):3, 2005.

[38] S. M. Seltzer and M. J. Berger. Bremsstrahlung energy spectra from electrons with kinetic energy 1 kev–10 gev incident on screened nuclei and orbital electrons of neutral atoms with z = 1–100. *Atomic Data and Nuclear Data Tables*, 35(3):345 , 1986.

[39] S. M. Seltzer and M. J. Berger. Bremsstrahlung spectra from electron interactions with screened atomic nuclei and orbital electrons. *Nuclear Instruments and Methods in Physics Research Section B: Beam Interactions with Materials and Atoms*, 12(1):95, 1985.

[40] R. Pratt, H. Tseng, C. Lee, L. Kissel, C. MacCallum, and M. Riley. Bremsstrahlung energy spectra from electrons of kinetic energy 1 kev¡=t1¡=000 kev incident on neutral atoms 2¡=z¡=92. *Atomic Data and Nuclear Data Tables*, 20(2):175, 1977.

[41] H. Bethe and W. Heitler. On the stopping of fast particles and on the creation of positive electrons. *Proceedings of the Royal Society of London. Series A, Containing Papers of a Mathematical and Physical Character*, 146(856):83, 1934.

[42] H. Bethe. The influence of screening on the creation and stopping of electrons. In *Mathematical Proceedings of the Cambridge Philosophical Society*, volume 30, pages 524–539. Cambridge University Press, 1934.

[43] H. Davies, H. Bethe, and L. Maximon. Theory of bremsstrahlung and pair production. ii. integral cross section for pair production. *Physical Review*, 93(4):788, 1954.

[44] E. Haug. Bremsstrahlung and pair production in the field of free electrons. *Zeitschrift für Naturforschung A*, 30(9):1099, 1975.

[45] L. D. Landau and E. M. Lifshitz. *The classical theory of fields*, volume 2. Pergamon, 2013.

[46] J. G. Kirk, A. Bell, and I. Arka. Pair production in counter-propagating laser beams. *Plasma Physics and Controlled Fusion*, 51(8):085008, 2009.

[47] C. P. Ridgers, J. G. Kirk, R. Duclous, T. Blackburn, C. Brady, K. Bennett, T. Arber, and A. Bell. Modelling gamma-ray photon emission and pair production in high-intensity laser–matter interactions. *Journal of Computational Physics*, 260:273, 2014.

[48] G. Moortgat-Pick. The furry picure. In *Journal of Physics: Conference Series*, volume 198, page 012002. IOP Publishing, 2009.

[49] W. Furry. On bound states and scattering in positron theory. *Physical Review*, 81(1):115, 1951.

[50] T. Erber. High-energy electromagnetic conversion processes in intense magnetic fields. *Reviews of Modern Physics*, 38(4):626, 1966.

[51] C. Ridgers, et al. Signatures of quantum effects on radiation reaction in laser–electron-beam collisions. *Journal of Plasma Physics*, 83(5), 2017.

[52] C. Rau. Imaging with coherent synchrotron radiation: X-ray imaging and coherence beamline (i13) at diamond light source. *Synchrotron Radiation News*, 30(5):19, 2017.

[53] F. Löhl. *Optical synchronization of a free-electron laser with femtosecond precision*. Ph.D. thesis, University of Hamburg, 2009.

[54] E. Saldin, E. Schneidmiller, and M. V. Yurkov. *The physics of free electron lasers*. Springer Science & Business Media, 1999.

[55] J. Rönsch-Schulenburg, K. Honkavaara, M. Kuhlmann, S. Schreiber, R. Treusch, M. Vogt, et al. Upgrade plans for flash for the years after 2020. In *Proceedings of the 10th International Particle Accelerator Conference*, pages 1909–1911. 2019.

[56] J. Arthur. Status of the lcls x-ray fel program. *Review of scientific instruments*, 73(3):1393, 2002.

[57] D. Eakins and D. Chapman. X-ray imaging of subsurface dynamics in high-z materials at the diamond light source. *Review of Scientific Instruments*, 85(12):123708, 2014.

[58] M. Mo, et al. Ultrafast visualization of incipient plasticity in dynamically compressed matter. *Nature communications*, 13(1):1, 2022.

[59] A. Rousse, et al. Production of a kev x-ray beam from synchrotron radiation in relativistic laser-plasma interaction. *Physical Review Letters*, 93(13):135005, 2004.

[60] S. Fourmaux, et al. Demonstration of the synchrotron-type spectrum of laser-produced betatron radiation. *New Journal of Physics*, 13(3):033017, 2011.

[61] A. Teymurazyan, et al. High precision photon flux determination for photon tagging experiments. *Nuclear Instruments and Methods in Physics Research Section A: Accelerators, Spectrometers, Detectors and Associated Equipment*, 767:300, 2014.

[62] G. Collaboration, et al. First results from the gluex experiment. In *AIP Conference Proceedings*, volume 1735, page 020001. AIP Publishing LLC, 2016.

[63] R. McKeown. The jefferson lab 12 gev upgrade. In *AIP Conference Proceedings*, volume 1374, pages 121–126. American Institute of Physics, 2011.

[64] H. Al Ghoul, et al. Measurement of the beam asymmetry σ for π 0 and η photoproduction on the proton at e γ= 9 gev. *Physical Review C*, 95(4):042201, 2017.

[65] B. L. Berman and S. Fultz. Measurements of the giant dipole resonance with monoenergetic photons. *Reviews of Modern Physics*, 47(3):713, 1975.

[66] L. Jammes, G. Audit, A. Block, N. de Botton, N. d'Hose, J. Martin, C. Schuhl, G. Tamas, P. Argan, and P. Pedroni. Total cross section measurement of $\pi 0$ photoproduction near threshold on complex nuclei. *Physics Letters B*, 227(1):21, 1989.

[67] P. Argan, et al. A 130 to 530 mev tagged photon beam obtained by in flight positron annihilation. *Nuclear Instruments and Methods in Physics Research Section A: Accelerators, Spectrometers, Detectors and Associated Equipment*, 228(1):20, 1984.

[68] A. Di Piazza, C. Müller, K. Hatsagortsyan, and C. H. Keitel. Extremely high-intensity laser interactions with fundamental quantum systems. *Reviews of Modern Physics*, 84(3):1177, 2012.

[69] G.-P. An, et al. High energy and high brightness laser compton backscattering gamma-ray source at ihep. *Matter and Radiation at Extremes*, 3(4):219, 2018.

[70] H. R. Weller and M. W. Ahmed. The hiγs facility: a free-electron laser generated gamma-ray beam for research in nuclear physics. pages 1569–1590. World Scientific, 2003.

[71] Y. Wu. Overview of high intensity gamma-ray source-capabilities and future upgrades. In *2013 International Workshop on Polarized Sources, Targets and Polarimetry, University of Virginia*. 2013.

[72] Y. Wu, et al. Performance and capabilities of upgraded high intensity gamma-ray source at duke university. *Proceedings of PAC09*, pages 3181–3183, 2009.

[73] C. Courtois, et al. Characterisation of a mev bremsstrahlung x-ray source produced from a high intensity laser for high areal density object radiography. *Physics of Plasmas*, 20(8):083114, 2013.

[74] M. Perry, J. Sefcik, T. Cowan, S. Hatchett, A. Hunt, M. Moran, D. Pennington, R. Snavely, and S. Wilks. Hard x-ray production from high intensity laser solid interactions. *Review of Scientific Instruments*, 70(1):265, 1999.

[75] C. Armstrong, et al. Bremsstrahlung emission from high power laser interactions with constrained targets for industrial radiography. *High Power Laser Science and Engineering*, 7, 2019.

[76] D. Rusby, C. Armstrong, G. Scott, M. King, P. McKenna, and D. Neely. Effect of rear surface fields on hot, refluxing and escaping electron populations via numerical simulations. *High Power Laser Science and Engineering*, 7, 2019.

[77] R. P. Drake. *High-energy-density physics*. Springer, 2010.

[78] L. Spitzer. *Physics of fully ionized gases*. Courier Corporation, 2nd edition, 1962.

[79] P. Kaw and J. Dawson. Relativistic nonlinear propagation of laser beams in cold overdense plasmas. *Physics of Fluids*, 13(2):472, 1970.

[80] P. Gibbon. *Short pulse laser interactions with matter: an introduction*. Imperial College Press, 2005.

[81] C. Danson, D. Hillier, N. Hopps, and D. Neely. Petawatt class lasers worldwide. *High power laser science and engineering*, 3, 2015.

[82] C. Danson, et al. Vulcan petawatt—an ultra-high-intensity interaction facility. *Nuclear Fusion*, 44(12):S239, 2004.

[83] D. Strickland and G. Mourou. Compression of amplified chirped optical pulses. *Optics communications*, 55(6):447, 1985.

[84] I. N. Ross, J. L. Collier, P. Matousek, C. N. Danson, D. Neely, R. M. Allott, D. A. Pepler, C. Hernandez-Gomez, and K. Osvay. Generation of terawatt pulses by use of optical parametric chirped pulse amplification. *Applied Optics*, 39(15):2422, 2000.

[85] T. Z. Esirkepov, et al. Prepulse and amplified spontaneous emission effects on the interaction of a petawatt class laser with thin solid targets. *Nuclear Instruments and Methods in Physics Research Section A: Accelerators, Spectrometers, Detectors and Associated Equipment*, 745:150, 2014.

[86] C. Ziener, P. Foster, E. Divall, C. Hooker, M. Hutchinson, A. Langley, and D. Neely. Specular reflectivity of plasma mirrors as a function of intensity, pulse duration, and angle of incidence. *Journal of Applied Physics*, 93(1):768, 2003.

[87] D. Neely, et al. Frequency doubling of multi-terawatt picosecond pulses. *Laser and Particle Beams*, 17(2):281, 1999.

[88] V. Ginzburg. The propagation of electromagnetic waves in plasmas.

[89] F. Brunel. Not-so-resonant, resonant absorption. *Physical review letters*, 59(1):52, 1987.

[90] E. S. Weibel. Anomalous skin effect in a plasma. *The Physics of Fluids*, 10(4):741, 1967.

[91] P. Catto and R. M. More. Sheath inverse bremsstrahlung in laser produced plasmas. *The Physics of Fluids*, 20(4):704, 1977.

[92] S. Wilks, W. Kruer, M. Tabak, and A. Langdon. Absorption of ultra-intense laser pulses. *Physical Review Letters*, 69(9):1383, 1992.

[93] C. Moore, A. Ting, S. McNaught, J. Qiu, H. Burris, and P. Sprangle. A laser-accelerator injector based on laser ionization and ponderomotive acceleration of electrons. *Physical Review Letters*, 82(8):1688, 1999.

[94] A. Bell, J. Davies, S. Guerin, and H. Ruhl. Fast-electron transport in high-intensity short-pulse laser-solid experiments. *Plasma Physics and Controlled Fusion*, 39(5):653, 1997.

[95] H. Alfvén. On the motion of cosmic rays in interstellar space. *Physical Review*, 55(5):425, 1939.

[96] J. Davies. Magnetic-field-limited currents. *Physical Review E*, 68(3):037501, 2003.

[97] D. Hammer and N. Rostoker. Propagation of high current relativistic electron beams. *Physics of Fluids*, 13(7):1831, 1970.

[98] Y. T. Lee and R. More. An electron conductivity model for dense plasmas. *Physics of Fluids*, 27(5):1273, 1984.

[99] N. March. The thomas-fermi approximation in quantum mechanics. *Advances in Physics*, 6(21):1, 1957.

[100] A. Bell. New equations of state for medusa. Technical report, Science Research Council, 1980.

[101] R. Latter. Temperature behavior of the thomas-fermi statistical model for atoms. *Physical Review*, 99(6):1854, 1955.

[102] M. Berger, M. Inokuti, H. Anderson, H. Bichsel, J. Dennis, D. Powers, S. Seltzer, and J. Turner. Report 37. *Journal of the International Commission on Radiation Units and Measurements*, (2):NP, 1984.

[103] M. Inokuti. Inelastic collisions of fast charged particles with atoms and molecules—the bethe theory revisited. *Reviews of modern physics*, 43(3):297, 1971.

[104] Geant4 collaboration, Physics reference manual, Release 10.7, 2020.

[105] E. Fermi. The ionization loss of energy in gases and in condensed materials. *Physical Review*, 57(6):485, 1940.

[106] R. M. Sternheimer. The density effect for the ionization loss in various materials. *Physical Review*, 88(4):851, 1952.

[107] C. Møller. Über den stoss zweier teilchen unter berücksichtigung der retardation der kräfte. *Zeitschrift für Physik*, 70(11-12):786, 1931.

[108] V. Ivin, M. Silakov, G. Babushkin, B. Lu, P. Mangat, K. Nordquist, and D. Resnick. Modeling and simulation issues in monte carlo calculation of electron interaction with solid targets. *Microelectronic engineering*, 69(2-4):594, 2003.

[109] J. Davies, A. Bell, M. Haines, and S. Guerin. Short-pulse high-intensity laser-generated fast electron transport into thick solid targets. *Physical Review E*, 56(6):7193, 1997.

[110] J. Davies. How wrong is collisional monte carlo modeling of fast electron transport in high-intensity laser-solid interactions? *Physical Review E*, 65(2):026407, 2002.

[111] A. Robinson, D. Strozzi, J. Davies, L. Gremillet, J. Honrubia, T. Johzaki, R. Kingham, M. Sherlock, and A. Solodov. Theory of fast electron transport for fast ignition. *Nuclear Fusion*, 54(5):054003, 2014.

[112] L. Gremillet, G. Bonnaud, and F. Amiranoff. Filamented transport of laser-generated relativistic electrons penetrating a solid target. *Physics of Plasmas*, 9(3):941, 2002.

[113] T. Arber, et al. Contemporary particle-in-cell approach to laser-plasma modelling. *Plasma Physics and Controlled Fusion*, 57(11):113001, 2015.

[114] C. Ridgers, C. Brady, R. Duclous, J. Kirk, K. Bennett, T. Arber, A. Robinson, and A. Bell. Dense electron-positron plasmas and ultraintense γ rays from laser-irradiated solids. *Physical Review Letters*, 108(16):165006, 2012.

[115] C. K. Birdsall and A. B. Langdon. *Plasma physics via computer simulation*. CRC press, 2004.

[116] R. Kingham and A. Bell. An implicit vlasov–fokker–planck code to model non-local electron transport in 2-d with magnetic fields. *Journal of Computational Physics*, 194(1):1, 2004.

[117] A. Bell, A. Robinson, M. Sherlock, R. Kingham, and W. Rozmus. Fast electron transport in laser-produced plasmas and the kalos code for solution of the vlasov–fokker–planck equation. *Plasma Physics and Controlled Fusion*, 48(3):R37, 2006.

[118] N. J. Sircombe and T. D. Arber. Valis: A split-conservative scheme for the relativistic 2d vlasov–maxwell system. *Journal of Computational Physics*, 228(13):4773, 2009.

[119] J. Dawson. One-dimensional plasma model. *Physics of Fluids*, 5(4):445, 1962.

[120] R. Morse and C. Nielson. Numerical simulation of warm two-beam plasma. *Physics of Fluids*, 12(11):2418, 1969.

[121] C. K. Birdsall and D. Fuss. Clouds-in-clouds, clouds-in-cells physics for many-body plasma simulation. *Journal of Computational Physics*, 3(4):494, 1969.

[122] J. P. Boris. Relativistic plasma simulation-optimization of a hybrid code. In *Proceedings of the 4th Conference on Numerical simulation of plasmas*, pages 3–67. 1970.

[123] K. Yee. Numerical solution of initial boundary value problems involving maxwell's equations in isotropic media. *IEEE Transactions on antennas and propagation*, 14(3):302, 1966.

[124] J. Villasenor and O. Buneman. Rigorous charge conservation for local electromagnetic field solvers. *Computer Physics Communications*, 69(2-3):306, 1992.

[125] T. Z. Esirkepov. Exact charge conservation scheme for particle-in-cell simulation with an arbitrary form-factor. *Computer Physics Communications*, 135(2):144, 2001.

[126] R. Duclous, J. G. Kirk, and A. R. Bell. Monte carlo calculations of pair production in high-intensity laser–plasma interactions. *Plasma Physics and Controlled Fusion*, 53(1):015009, 2010.

[127] R. Ward and N. Sircombe. Fast particle bremsstrahlung effects in the pic code epoch: Enhanced diagnostics for laser-solid interaction modelling. Technical report, Central Laser Facility, 2014.

[128] D. Wu, X. He, W. Yu, and S. Fritzsche. Particle-in-cell simulations of laser–plasma interactions at solid densities and relativistic intensities: the role of atomic processes. *High Power Laser Science and Engineering*, 6, 2018.

[129] B. Martinez, M. Lobet, R. Duclous, E. d'Humières, and L. Gremillet. High-energy radiation and pair production by coulomb processes in particle-in-cell simulations. *Physics of Plasmas*, 26(10):103109, 2019.

[130] Y. Sentoku, K. Mima, T. Taguchi, S. Miyamoto, and Y. Kishimoto. Particle simulation on x-ray emissions from ultra-intense laser produced plasmas. *Physics of Plasmas*, 5(12):4366, 1998.

[131] Y.-S. Tsai. Pair production and bremsstrahlung of charged leptons. *Reviews of Modern Physics*, 46(4):815, 1974.

[132] Y.-S. Tsai. Erratum: Pair production and bremsstrahlung of charged leptons. *Reviews of Modern Physics*, 49(2):421, 1977.

[133] P. D. Lax. Hyperbolic difference equations: A review of the courant-friedrichs-lewy paper in the light of recent developments. *IBM Journal of Research and Development*, 11(2):235, 1967.

[134] C. K. Birdsall and N. Maron. Plasma self-heating and saturation due to numerical instabilities. *Journal of Computational Physics*, 36(1):1, 1980.

[135] R. Hockney. Measurements of collision and heating times in a two-dimensional thermal computer plasma. *Journal of Computational Physics*, 8(1):19, 1971.

[136] O. Buneman. *Computer Space Plasma Physics: Simulations Techniques and Software*, pages 72–73. Terra Scientific, 1993.

[137] D. Woodbury, et al. Laser wakefield acceleration with mid-ir laser pulses. *Optics letters*, 43(5):1131, 2018.

[138] S. Kar, A. Robinson, D. Carroll, O. Lundh, K. Markey, P. McKenna, P. Norreys, and M. Zepf. Guiding of relativistic electron beams in solid targets by resistively controlled magnetic fields. *Physical Review Letters*, 102(5):055001, 2009.

[139] N. Sircombe, S. Hughes, and M. Ramsay. Integrated calculations of short-pulse laser interactions with matter. *New Journal of Physics*, 15(2):025025, 2013.

[140] T. Daykin, H. Sawada, Y. Sentoku, F. Beg, H. Chen, H. McLean, A. Link, P. Patel, and Y. Ping. Characterization of fast electron divergence and energy spectrum from modeling of angularly resolved bremsstrahlung measurements. *Physics of Plasmas*, 25(12):123103, 2018.

[141] Hybrid-PIC code available at `https://github.com/Status-Mirror/epoch` last accessed 30 June 2021.

[142] S. Agostinelli, et al. Geant4—a simulation toolkit. *Nuclear instruments and methods in physics research section A: Accelerators, Spectrometers, Detectors and Associated Equipment*, 506(3):250, 2003.

[143] J. Allison, et al. Geant4 developments and applications. *IEEE Transactions on nuclear science*, 53(1):270, 2006.

[144] J. Allison, et al. Recent developments in geant4. *Nuclear Instruments and Methods in Physics Research Section A: Accelerators, Spectrometers, Detectors and Associated Equipment*, 835:186, 2016.

[145] C. Walsh, J. Chittenden, D. Hill, and C. Ridgers. Extended-magnetohydrodynamics in under-dense plasmas. *Physics of Plasmas*, 27(2):022103, 2020.

[146] D. E. Peplow. Direction cosines and polarization vectors for monte carlo photon scattering. *Nuclear Science and Engineering*, 131(1):132, 1999.

[147] R. More. Pressure ionization, resonances, and the continuity of bound and free states. In *Advances in atomic and molecular physics*, volume 21, pages 305–356. Elsevier, 1985.

[148] D. R. Lide. *CRC handbook of chemistry and physics*, volume 85. CRC press, 2004.

[149] W. Shang, et al. Experimental demonstration of laser to x-ray conversion enhancements with low density gold targets. *Applied Physics Letters*, 108(6):064102, 2016.

[150] S. P. Hatchett, et al. Electron, photon, and ion beams from the relativistic interaction of petawatt laser pulses with solid targets. *Physics of Plasmas*, 7(5):2076, 2000.

[151] S. Wilks, A. Langdon, T. Cowan, M. Roth, M. Singh, S. Hatchett, M. Key, D. Pennington, A. MacKinnon, and R. Snavely. Energetic proton generation in ultra-intense laser–solid interactions. *Physics of plasmas*, 8(2):542, 2001.

[152] V. Grichine. Electromagnetic angular models. Geant4 progress meeting, CERN.

[153] A. Hanson, L. Lanzl, E. Lyman, and M. Scott. Measurement of multiple scattering of 15.7-mev electrons. *Physical Review*, 84(4):634, 1951.

[154] G. J. Lockwood, L. E. Ruggles, G. H. Miller, and J. Halbleib. Calorimetric measurement of electron energy deposition in extended media. theory vs experiment. Technical report, Sandia Labs., Albuquerque, NM (USA), 1980.

[155] M. Berger, J. Coursey, and M. Zucker. Estar, pstar and astar: Computer programs for calculating stopping-power and range tables for electrons, protons and α-particles (version 1.2. 2). *NIST, Gaithersburg*, 2000.

[156] D. Rester, W. Dance, and J. Derrickson. Thick target bremsstrahlung produced by electron bombardment of targets of be, sn, and au in the energy range 0.2–2.8 mev. *Journal of Applied Physics*, 41(6):2682, 1970.

[157] H. Milchberg, R. Freeman, S. Davey, and R. More. Resistivity of a simple metal from room temperature to 10 6 k. *Physical Review Letters*, 61(20):2364, 1988.

[158] R. Evans, et al. Rapid heating of solid density material by a petawatt laser. *Applied Physics Letters*, 86(19):191505, 2005.

[159] R. Clarke, et al. Radiological characterisation of photon radiation from ultra-high-intensity laser–plasma and nuclear interactions. *Journal of Radiological Protection*, 26(3):277, 2006.

[160] F. Biggs and R. Lighthill. Analytical approximations for x-ray cross sections iii. Technical report, Sandia National Labs., Albuquerque, NM (USA), 1988.

[161] T. Cowan, et al. High energy electrons, nuclear phenomena and heating in petawatt laser-solid experiments. *Laser and Particle Beams*, 17(4):773, 1999.

[162] S. Belyshev, A. Ermakov, B. Ishkhanov, V. Khankin, A. Kurilik, A. Kuznetsov, V. Shvedunov, and K. Stopani. Studying photonuclear reactions using the activation technique. *Nuclear Instruments and Methods in Physics Research Section A: Accelerators, Spectrometers, Detectors and Associated Equipment*, 745:133, 2014.

[163] B. Girolami, B. Larsson, M. Preger, C. Schaerf, and J. Stepanek. Photon beams for radiosurgery produced by laser compton backscattering from relativistic electrons. *Physics in Medicine & Biology*, 41(9):1581, 1996.

[164] R. Edwards, et al. Characterization of a gamma-ray source based on a laser-plasma accelerator with applications to radiography. *Applied Physics Letters*, 80(12):2129, 2002.

[165] H. Chen, et al. Scaling the yield of laser-driven electron-positron jets to laboratory astrophysical applications. *Physical Review Letters*, 114(21):215001, 2015.

[166] A. Henderson, E. Liang, N. Riley, P. Yepes, G. Dyer, K. Serratto, and P. Shagin. Ultra-intense gamma-rays created using the texas petawatt laser. *High Energy Density Physics*, 12:46, 2014.

[167] S. Jiang, A. G. Krygier, D. W. Schumacher, K. U. Akli, and R. R. Freeman. Enhancing bremsstrahlung production from ultraintense laser-solid interactions with front surface structures. *European Physical Journal D*, 68(10):283, 2014.

[168] C. Armstrong, et al. Bremsstrahlung emission from high power laser interactions with constrained targets for industrial radiography. *High Power Laser Science and Engineering*, 7, 2019.

[169] A. Compant La Fontaine, C. Courtois, E. Lefebvre, J. Bourgade, O. Landoas, K. Thorp, and C. Stoeckl. Effects of electron recirculation on a hard x-ray source observed during the interaction of a high intensity laser pulse with thin au targets. *Physics of Plasmas*, 20(12):123111, 2013.

[170] K. Lezhnin, P. Sasorov, G. Korn, and S. Bulanov. High power gamma flare generation in multi-petawatt laser interaction with tailored targets. *Physics of Plasmas*, 25(12):123105, 2018.

[171] Z. Gong, R. Hu, H. Lu, J. Yu, D. Wang, E. Fu, C. Chen, X. He, and X. Yan. Brilliant gev gamma-ray flash from inverse compton scattering in the qed regime. *Plasma Physics and Controlled Fusion*, 60(4):044004, 2018.

[172] P. Zhang, C. Ridgers, and A. Thomas. The effect of nonlinear quantum electrodynamics on relativistic transparency and laser absorption in ultra-relativistic plasmas. *New Journal of Physics*, 17(4):043051, 2015.

[173] C. Brady, C. Ridgers, T. Arber, and A. Bell. Gamma-ray emission in near critical density plasmas. *Plasma Physics and Controlled Fusion*, 55(12):124016, 2013.

[174] H. Chang, B. Qiao, Y. Zhang, Z. Xu, W. Yao, C. Zhou, and X. He. Ultraintense laser absorption and γ-ray synchrotron radiation in near critical density plasmas. *Physics of Plasmas*, 24(4):043111, 2017.

[175] C. Brady, C. Ridgers, T. Arber, and A. Bell. Synchrotron radiation, pair production, and longitudinal electron motion during 10-100 pw laser solid interactions. *Physics of Plasmas*, 21(3):033108, 2014.

[176] B. Martinez, E. d'Humiéres, and L. Gremillet. Synchrotron emission from nanowire array targets irradiated by ultraintense laser pulses. *Plasma Physics and Controlled Fusion*, 60(7):074009, 2018.

[177] X.-B. Wang, G.-Y. Hu, Z.-M. Zhang, Y.-Q. Gu, B. Zhao, Y. Zuo, and J. Zheng. Gamma-ray generation from ultraintense laser-irradiated solid targets with preplasma. *High Power Laser Science and Engineering*, 8, 2020.

[178] Y. Zhao, J. Liu, G. Xia, and A. Bonatto. Dense high-energy γ-rays emission by ultraintense laser interacting with a concave target. *Physics of Plasmas*, 27(7):073106, 2020.

[179] K. Pan, C. Zheng, D. Wu, L. Cao, Z. Liu, and X. He. Study of strong enhancement of synchrotron radiation via surface plasma waves excitation by particle-in-cell simulations. *Applied Physics Letters*, 107(18):183902, 2015.

[180] B. Martinez, E. d'Humières, and L. Gremillet. Synchrotron radiation from ultrahigh-intensity laser-plasma interactions and competition with bremsstrahlung in thin foil targets. *Physical Review Research*, 2(4):043341, 2020.